JET ENERGY CALIBRATION IN ATLAS

by

Douglas William Schouten

B.Sc., University of British Columbia, 2004

A THESIS SUBMITTED IN PARTIAL FULFILLMENT
OF THE REQUIREMENTS FOR THE DEGREE OF
MASTER OF SCIENCE
in the Department of Physics

SIMON FRASER UNIVERSITY
Summer, 2007

APPROVAL

Name:	Douglas William Schouten
Degree:	Master of Science
Title of thesis:	Jet Energy Calibration in ATLAS
Examining Committee:	Dr. Karen Kavanagh Chair
	Dr. Michel Vetterli, Simon Fraser University Senior Supervisor
	Dr. Dugan O'Neil, Simon Fraser University Supervisor
	Dr. Chris Oram, TRIUMF Supervisor
	Dr. Sarah Johnson, Simon Fraser University Internal Examiner
Date Approved:	April 19, 2007

Abstract

A correct energy calibration for jets is essential to the success of the ATLAS experiment. In this thesis I study a method for deriving an in situ jet energy calibration for the ATLAS detector. In particular, I show the applicability of the missing transverse energy projection fraction method. This method is shown to set the correct mean energy for jets. Pileup effects due to the high luminosities at ATLAS are also studied. I study the correlations in lateral distributions of pileup energy, as well as the luminosity dependence of the in situ calibration method.

For those whose encouragement I could not continue without: dad, mom, Colleen, and family.

"It all went kablooie after the happy hamster hopped."

— Hamster Huey and the Gooey Kablooie

Acknowledgments

I suppose that in the great grand happenings of the cosmos, the publication of a study on the energy calibration of QCD jets in ATLAS is hardly an event worthy of pomp and circumstance, and it will probably (hopefully) be ignored in the great historical annals of humankind in the future. Regardless, it is the culmination of two years of work and many years of learning. For me, it is huge.

In as much as this is a personal milestone, it is an oppurtunity to express my sincere gratitude to those who have helped me in so many ways.

I extend my sincerest thanks to my family (Brenda, Kathryn, Linda & Trevor, Cheryl & Adam, Marc & Jody), and especially my parents: dad, mom, without your selfless support and encouragement over many years, this thesis could not have been imagined, let alone completed.

I extend my thanks no less to my wonderful fiance Colleen, who has made the last $1\frac{1}{2}$ years a delight. You provided encouragement and motivation at every turn. I love you.

It would be incredibly near-sighted of me to neglect the fantastic High Energy Physics Group at SFU, past and present (in no particular order, Dr. Dugan O'Neil, Zhiyi Liu, Dag Gillberg, Jen Godfrey, Travis Stewart, Gary Pike, Erfan Rezaie, Dr. Jyothsna Rani, Dr. Yann Coudeau, Dr. Rod Walker, and Marco Bieri) and especially my supervisor Dr. Mike Vetterli. Mike (and Dugan), your patience and helpfulness have not gone unnoticed. Students and post docs, the grad student 'repository' was a great center for informative - or at least entertaining - discussion. Cheers, guys.

Finally, I thank the creator of this intriguing universe. Studying it is a delight.

Contents

List of Tables

List of Figures

Preface

The environment in the ATLAS detector presents a real challenge for experimental particle physics. In order to establish the existence of the Higgs boson and to look for physics beyond the current theoretical framework, unprecedented center of mass energies and luminosities in a hadron collider are required. This is what the LHC delivers. Managing to measure the signals from the $p - p$ collisions of the LHC accurately is the task of ATLAS. If it is successful, ATLAS could well open up a whole new arena of fundamental physics research.

To this end, I became interested in working on ATLAS. The aim of this thesis has been to 'transport' some of the knowledge learned from previous experiments at the Tevatron to the LHC environment. The high luminosity brings the possibility of detecting rare events to within the span of our lifetime. However, it also presents its challenges: at design luminosity there are an average of 23 interactions taking place in each bunch crossing. Picking these signals apart in order to measure something intelligible is a difficult task, one aspect of which this thesis addresses.

A significant amount of introductory material is necessary to be able to address the subtle issues involved in calibrating QCD jets. In Chapters 1 - 3, I introduce the scope and design of the ATLAS detector with a particular emphasis on calorimetry. In Chapter 4, jets are defined. Chapter 5 is the first chapter which actually touches on the research I performed. I then switch gears again in Chapter 6 to introduce pileup and to concentrate on some of its most important features. Chapter 7 is the culmination of the previous chapters, as I present research on the effects of pileup in jet energy calibration.

Chapter 1

Introduction

The ATLAS (**A** **T**oroidal **L**HC **A**pparatus) experiment is situated at the LHC (**L**arge **H**adron **C**ollider) at CERN in Geneva, Switzerland. The LHC consists of two accelerator rings for proton-proton collisions with a center of mass energy of 14 TeV and a design luminosity of 10^{34} cm^{-2}s^{-1}. The ATLAS detector is designed to be a multi-purpose detector that will investigate many interesting fundamental physics phenomena at the high-energy frontier by looking at the debris from these p-p collisions.

1.1 Physics Motivation

The current theoretical framework of physics at subatomic length scales is encapsulated in the Standard Model (SM). This model describes the interaction of fermions, which are spin 1/2 particles, via mediating bosons with spin 1. The fermions are point-like objects and consist of the leptons[1] and the quarks[2]. The quarks and leptons are separated into three families which are symmetric except for mass, as shown in Figure 1.1. There is also mixing between the weak eigenstates of the three quark families, described ad hoc by the Cabbibo-Kobayashi-Maskawa (CKM) matrix.

The SM has been successful in describing the strong, weak, and electromagnetic

[1] e, μ, τ and corresponding ν_e, ν_μ, and ν_τ neutrinos

[2] u, d, s, c, b, and t

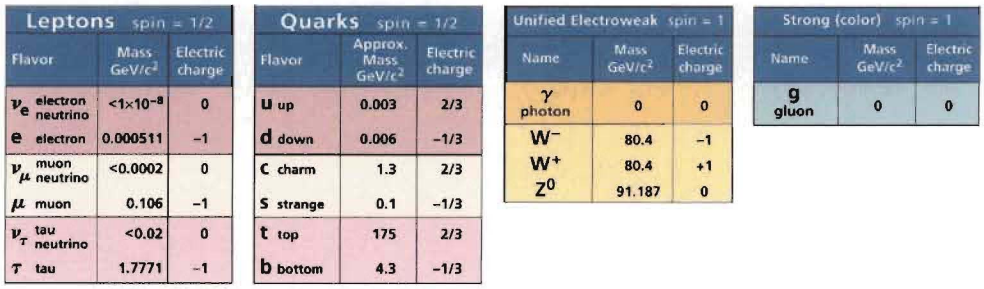

Leptons spin = 1/2		
Flavor	Mass GeV/c^2	Electric charge
ν_e electron neutrino	$<1\times10^{-8}$	0
e electron	0.000511	−1
ν_μ muon neutrino	<0.0002	0
μ muon	0.106	−1
ν_τ tau neutrino	<0.02	0
τ tau	1.7771	−1

Quarks spin = 1/2		
Flavor	Approx. Mass GeV/c^2	Electric charge
u up	0.003	2/3
d down	0.006	−1/3
c charm	1.3	2/3
s strange	0.1	−1/3
t top	175	2/3
b bottom	4.3	−1/3

Unified Electroweak spin = 1		
Name	Mass GeV/c^2	Electric charge
γ photon	0	0
W^-	80.4	−1
W^+	80.4	+1
Z^0	91.187	0

Strong (color) spin = 1		
Name	Mass GeV/c^2	Electric charge
g gluon	0	0

Figure 1.1: The fermions and bosons of the Standard Model of particle physics.

forces observed in nature. However, one of the unseen phenomena in this model is the Higgs mechanism of electroweak symmetry breaking. In the unification of the weak and electromagnetic forces, it is this mechanism that is thought to give rise to the mass of the W and Z bosons, while the γ (photon) remains massless. One of the consequences of this theory is the existence of a Higgs boson, which has not yet been seen experimentally. In fact, although many aspects of the SM have been tested, there is no direct evidence for the Higgs mechanism. The observation (or exclusion) and precision measurement of the properties of the Higgs boson are among the primary motivators of the ATLAS experiment. The ability of the ATLAS detector to discover the Higgs boson is illustrated in Figure 1.2.

Although the SM has been shown to be a very useful theory, it is believed by most to be incomplete, or a restricted subset of a more general and complete model. This is because the SM has 19 free parameters which are the coupling constants of the forces, the lepton and quark masses, the mass of the Z boson, and the four parameters of the CKM matrix. If, in fact the SM is part of some more fundamental theory, then it has been stated that something new should be discovered at the TeV energy scale that either extends or breaks the SM.

Among the more appealing concepts for theoreticians are supersymmetric (SUSY) models, although there is currently no experimental evidence for them. SUSY models are interesting for a couple of reasons: they incorporate the gravitational interaction into a quantum theory, they remove divergences in the Higgs self-coupling, and they inherit all the experimental evidence and predictive powers of the SM (which is a

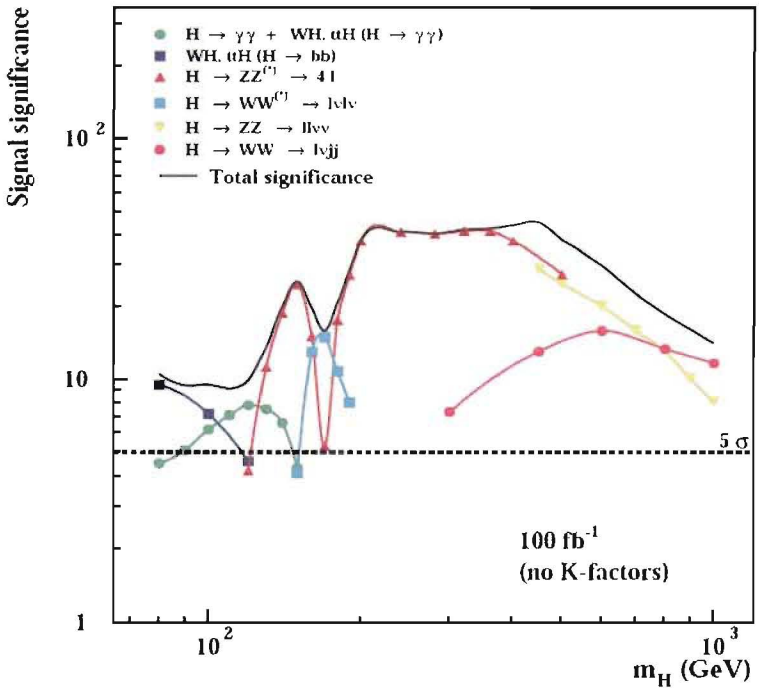

Figure 1.2: ATLAS sensitivity for the discovery of a SM Higgs boson. The vertical axis is the signal significance for various Higgs decay channels, measured in standard deviations (σ) from a null measurement. The common threshold for discovery is 5σ, indicated by the dashed horizontal line. The horizontal axis is the mass of the Higgs. ATLAS Experiment Image: Copyright CERN, [1].

subset of supersymmetric models) [1]. One of the consequences of these theories is a plethora of new super-particles to pair with all the presently observed particles, as well as multiple Higgs bosons. This new spectrum of particles hinges on a few parameters in these models, all of which are unknown. However, it is expected that if SUSY models are correct, the masses of at least some of these particles should be ≤ 1 TeV, and thus observable at the LHC energy scale [1].

Since ATLAS is designed to be a multi-purpose detector, it is also sensitive to a wide array of other physics processes. Some of these include precision measurements of the top quark mass in different channels, searches for rare top-quark decays, and B-physics studies including CP-violation measurements (tests of the CKM parameters),

rare decay searches and tests of SM branching ratio predictions, and inclusive cross-section measurements. These and other physics topics are reviewed extensively in the ATLAS Letter of Intent [2] and the ATLAS Detector and Physics Performance Technical Design Report [1].

1.2 Experimental Overview

1.2.1 The Large Hadron Collider

Only a cursory overview of the LHC is presented here. A more in-depth description can be found in the LHC Design Report [3]. The LHC is a 27 km circumference, superconducting, two-ring accelerator currently being deployed in the LEP tunnel at CERN. There are two high-luminosity experiments (ATLAS and CMS) and two low-luminosity experiments (LHCb and ALICE) located at symmetric points on the LHC. The accelerator is designed to collide counter-rotating, 7 TeV protons from the two rings to yield a center of mass energy of 14 TeV at the four interaction points, as shown in Figure 1.3. The ability to collide heavy ions (such as lead) is also part of the design. This will be used particularly for the ALICE experimental programme. The high beam intensities (10^{34} cm^{-2}s^{-1}, more than one hundred times the luminosity of the Tevatron) exclude the use of anti-protons because they are much more difficult to produce than protons. Therefore the LHC has a separate magnet system for both of the rings, although the two beams are merged into a common system at the injection and interaction regions [3]. At the design luminosity of the LHC, proton bunches will cross the interaction regions every 25 ns, with a mean multiplicity of around 23 non-diffractive proton-proton collisions per bunch crossing. The protons are accelerated to 7 TeV ($0.9999999677c$) in four stages as shown in Fig 1.4: a 50 MeV boost in the linear accelerator, followed by injection into the Proton Synchrotrons (Booster, PS) which accelerate to 1.4 and 26 GeV respectively, and finally into the Super Proton Synchrotron (SPS) which accelerates the particles to 450 GeV before final injection into the LHC ring. Leading order cross-sections for some important processes at the LHC are summarized in Table 1.1.

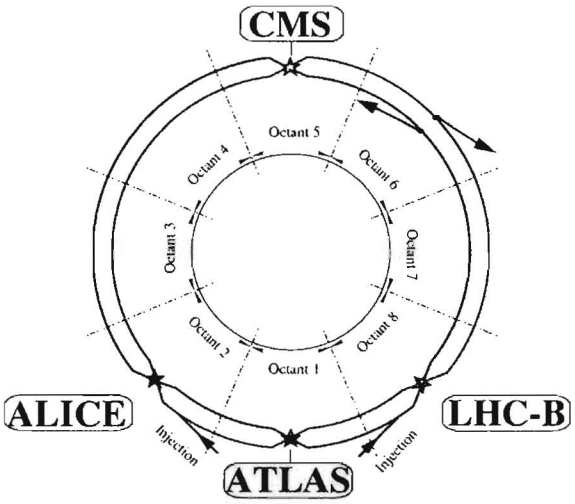

Figure 1.3: LHC experimental overview displaying the location of the four detectors and the two ring structure. ATLAS Experiment Image: Copyright CERN, [4].

Process	**Cross-section**
inclusive H with $m_H = 100$ GeV	27.8 pb
inclusive SUSY $m_{\tilde{g}} \simeq 1$ TeV	3.4 pb
inclusive $b\bar{b}$	500 μb
inclusive $t\bar{t}$ ($m_t = 175$ GeV)	590 pb
di-jet processes w/ 1 jet $p_T > 180$ GeV, $\|\eta\| < 3.2$	13 μb

Table 1.1: Leading order cross-sections for some typical processes at LHC. These numbers have been obtained from Monte Carlo simulations [1].

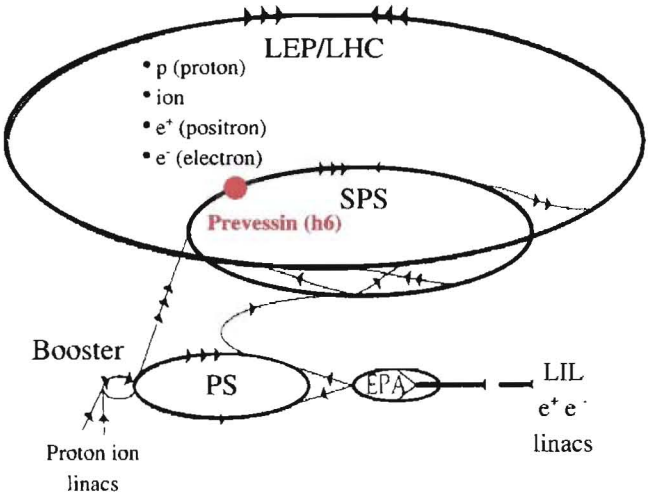

Figure 1.4: LHC with injector complex. The injection sequence is as follows: linac (50 MeV), PS booster (1.4 GeV), PS (26 GeV), SPS (450 GeV) [5].

1.2.2 The ATLAS Detector

Much of the ATLAS detector is currently in either advanced construction or early commissioning stages, with the detector turn-on date set for late 2007. ATLAS consists of three main components: an inner detector and tracking system, particle calorimetry, and a large muon spectrometer. Each of these main components consists of specialized sub-components. There is also a magnet system for bending charged particle trajectories. The inner detector is contained within a large superconducting solenoid with a magnetic field of 2 T, and large air-core toroids generate the field for the muon spectrometer. The layout of the ATLAS detector is shown in Figure 3.1. The detector weighs more than 7000t and is 44m long with a diameter of 22m. The overall design goals of the ATLAS detector are [1]:

- precise electromagnetic calorimetry to detect photons and electrons, and good coverage in hadronic calorimetry
- precision muon momentum measurement
- efficient tracking, even at high luminosity, for charged high-p_T particles

- near-hermetic solid angle coverage for the different detector subsystems

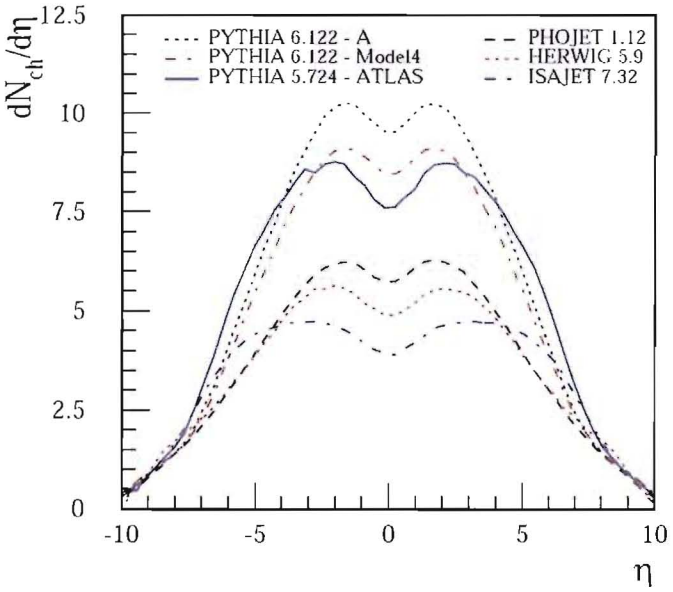

Figure 1.5: Charged particles per unit η from minimum bias collisions, shown as a function of η. The various curves correspond to different Monte Carlo fragmentation models (see Chapter 4). ATLAS Experiment Image: Copyright CERN, [1].

The ATLAS coordinate system consists of the beam direction as the z-axis, with the $x-y$ plane transverse to the beam direction. The positive x direction is defined as pointing into the center of the LHC ring. The azimuthal angle ϕ is measured in the $x-y$ plane about the z-axis, and the polar angle θ is measured from the beam axis. Instead of θ, the pseudorapidity η is often used, and is defined as $\eta = -\ln(\tan(\theta/2))$. Pseudorapidity is a useful measure in colliding beam experiments because it is approximately additive under Lorentz boosts in the z direction (along the beam axis), and so pseudorapidity differences are invariant. Another characteristic of pseudorapidity is that the particle rate per unit area for collisions with low momentum transfer is approximately equal for all η regions, as shown in Figure 1.5. A commonly used distance measurement in $\eta - \phi$ space is $\Delta\mathrm{R} = \sqrt{\Delta\eta^2 + \Delta\phi^2}$.

The quantities p_T (transverse momentum) and E_T (transverse energy) are defined in the $x-y$ plane. Missing transverse energy is a useful signature for interesting

events since it indicates the presence of neutrinos or new particles which pass through the calorimeters undetected. It is defined as

$$\vec{E}_T = -\sum_{\text{cells}} \vec{E}_T, \tag{1.1}$$

where the vector sum is over all the cells in the ATLAS calorimeters[3].

1.3 Experimental Techniques

There are a number of techniques that can be employed to search for new discoveries in particle physics. These can be (1) high precision searches, where one looks for small deviations from theoretical predictions using large data samples, or (2) high energy searches in either fixed target or colliding beam setups. In the latter approach, which is used at ATLAS, the measurement of the scattered products from the collisions involves measuring the cross-section, σ. The cross-section is a measure of the probability for a scattering process to occur. It is related to the event rate by

$$\frac{d\sigma}{d\Omega} = \frac{1}{L}\frac{dN}{d\Omega} \tag{1.2}$$

where L is the luminosity ($= \frac{\text{particles}}{\text{area}\times\text{time}}$), N is the event rate, and Ω is the solid angle. The cross-section can be calculated using Fermi's Golden Rule and the Feynman Rules for quantum electrodynamics and quantum chromodynamics. For completeness, the interaction length or mean free path of a particle in material is λ, and is given by $(\sigma n_a)^{-1}$ where n_a is the particle density of the material and σ is the cross section for the interaction (eg. Compton scattering for photons). This is an important quantity in the design of detectors.

For each physics process, the probability of occurrence can be calculated theoretically and compared to data from the experiment. Over a time-integrated luminosity, one can expect some $n = \int L d\sigma dt$ number of events. The detector must be optimized

[3]Since muons leave only small fractions of their energy in the calorimeters, the muon spectrometer is used to account for the transverse energy due to muons.

to be able to distinguish these events as efficiently as possible so that if, for example, a Higgs boson decay occurs, it can be detected.

In the ATLAS experiment beams of protons collide at the interaction point. At the high design CM energy, asymptotic freedom in QCD tells us that the quarks which comprise the protons are essentially free particles as far as the strong force is concerned. It can be said that at ATLAS, the LHC is essentially colliding 'bags' of quarks and gluons, as opposed to protons. These partons interact quantum mechanically, and only rarely scatter energetically enough to produce heavy particles such as the Higgs boson or $t\bar{t}$ quark pairs. The fundamental problem at ATLAS is then to pick out these rare events from a very large background of uninteresting events. For instance, in one year at initial operation (which is at significantly lower luminosity than design), there will be $O(10^{14})$ inelastic scattering events, compared to $O(10^3)$ Higgs boson decays.

Chapter 2

Calorimetry

Calorimetry, or energy measurement, is an integral part of modern particle physics experiments. It provides measurements of energy for interacting particles, and it also provides measurements for overall event quantities such as energy flow and transverse momentum imbalances, which are signatures of many interesting events. Combined with accurate momentum measurements, calorimetry can also provide particle identification over a range of energies. All calorimetry measurements are destructive processes, i.e., a particle that enters a calorimeter is changed in the measurement process. For this reason, calorimeters are located spatially outside of other subdetector systems such as vertex detectors and tracking chambers[1].

There are essentially two broad classes of calorimetry, namely electromagnetic and hadronic. Electromagnetic calorimeters are tuned to measure the energy of incident photons, electrons and positrons. On the other hand, hadronic calorimeters are tuned to measure the energy of incident hadrons. Over both of these classes, there are two main distinct technologies employed. These are (1) homogeneous calorimeters, often made of scintillating crystals, and (2) sampling calorimeters, which are built of alternating absorber and detector layers. ATLAS uses only sampling calorimeter detectors because homogeneous detectors were found to be too expensive and generally

[1]Note, however, that muons are essentially minimum ionizing particles (see Section 2.2) and so on average they lose only a small amount of their energy in the calorimeter. For this reason, the muon spectrometer is located outside of the calorimeter systems.

more sensitive to radiation damage.

This chapter begins with an introduction to electromagnetic calorimetry in Section 2.1. This section begins with a description of the ways photons and electrons interact with matter, and concludes with a qualitative description of how an electromagnetic shower develops. In Section 2.2 hadronic calorimetry is introduced. A qualitative picture of a hadronic shower is developed. Then, in Section 2.3, the differences between electromagnetic and hadronic calorimetry are discussed with respect to the issue of compensation. This is important for the ATLAS calorimeters, which are non-compensating. The chapter concludes with a brief overview of sampling calorimeters in Section 2.4.

2.1 Electromagnetic Calorimetry

An incident electron, positron or photon will initiate a cascade of particles as it passes through matter. In Section 2.1.1, the main processes by which a photon will interact as it passes through a calorimeter are presented. The next section describes the interactions of electrons and positrons. All of these processes are important in the development of electromagnetic showers, which are described in Section 2.1.3. The energy deposited by these showers is what is measured by an electromagnetic calorimeter.

2.1.1 Photon interactions

There are basically three processes by which photons interact with matter: the photoelectric effect, Compton scattering, and pair production. All of these contribute at varying levels over different energy regimes. For high energy photons, pair production is the dominant process, while for very low energy photons, the photoelectric effect is the most probable interaction. A plot of the cross-sections for these processes is shown in Figure 2.1. Rayleigh scattering is another interaction that may occur, but this process affects only the spatial distribution of scattered photons at low energy, and so is not very important in calorimetry [6]. For photons, there is a mean free path

λ over which *on average* photons will travel without interacting. The probability that a photon will not interact over some distance x in matter is $1 - e^{-x/\lambda}$.

Photoelectric effect

In this process, which is dominant for very low energy photons, a photon is absorbed by an atom which then emits an electron. The atom is left in an excited state and returns to its ground state by emitting either a photon or an electron from one of its outer shells. The cross-section for the photoelectric effect depends strongly on the available number of electrons, and thus on the Z of the material as Z^n, with $4 \leq n \leq 5$ [6]. The cross-section also varies strongly with the photon energy as E^{-3}, and so it is strongly suppressed for energetic photons.

Compton scattering

In Compton scattering, a photon scatters from an atomic electron energetically enough to put the electron into an unbound state. For most materials, Compton scattering is the most probable interaction in the energy range O(keV) to $\sim$ 5 MeV [6], and therefore it is a very important part of electromagnetic calorimetry since, as will be shown in Section 2.1.3, the majority of the energy is deposited by these low-energy photons. Compton scattering exhibits a preference for photons scattering in the forward hemisphere. Because the photoelectric effect only comes into play at low energies, an intermediate energy (MeV range) photon will Compton scatter many times before being absorbed by an atom. After many scatters the direction of the photon is distributed isotropically [6]. The cross-section for Compton scattering falls with photon energy as $1/E$, and varies linearly with the Z of the absorbing material.

Pair production

For photons with energy greater than $2m_e c^2$ an electron/positron pair may be created in the presence of a nucleus or atomic electron. In this energy regime, pair production is the predominant mechanism for photons to interact. In the Feynman diagram (see Figure 2.2), the recoil photon is the atomic electric field. The cross-section

for pair production rises with energy until leveling off at very high energies. For a photon of energy k and electron (positron) of energy $E_-(E_+)$, the ratio w is defined as $w_\pm = E_\pm/k$, and the cross section is given by [7]:

$$\frac{d\sigma}{dE_+} = \frac{4\alpha Z^2 e^4}{k(m_e c^2)^2}\left[(w_+^2 + w_-^2 + \frac{2}{3}w_+w_-)\ln(183/Z^{1/3}) - \frac{1}{9}w_+w_-\right], \qquad (2.1)$$

where α is the fine structure constant $\frac{1}{137}$.

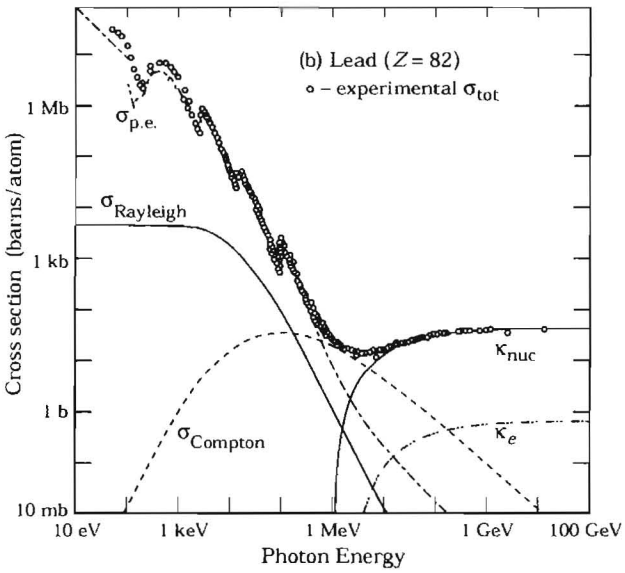

Figure 2.1: Contributions to the photon interaction cross-section. $\sigma_{\text{p.e.}}$ is the photoelectric effect, σ_{Rayleigh} is Rayleigh scattering, σ_{Compton} is Compton scattering, and $K_{\text{nuc}}, K_{\text{e}}$ are pair production off nuclei and atomic electrons respectively [8].

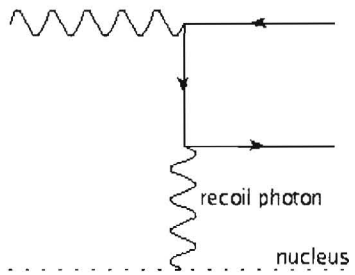

Figure 2.2: Feynman diagram of photon pair production.

2.1.2 Interactions of electrons and positrons

There are many ways in which all charged particles can interact with matter [6]:

- they may ionize atoms or molecules
- at very high velocities (faster than the the speed of light in the material), they may emit Cerenkov radiation
- at high energies, bremsstrahlung radiation is produced.

Except for special Cerenkov detectors, the ionization and bremsstrahlung processes are the most important. Ionization is more important in lower energy regimes. For electrons and positrons there is a critical energy ϵ_c at which the average energy loss due to ionization is equal to that due to bremsstrahlung [6]. This critical energy grows with $(m/m_e)^2$ for particles (with mass m) other than the electron. For the next heaviest lepton, the muon, $(m/m_e)^2 \simeq 4000$, so bremsstrahlung is only important at high energies. Electrons lose energy due to ionization at a rate given by [7]:

$$\frac{dE}{dx} = \frac{2\pi n_e e^4}{mc^2}\left(2\ln\frac{2mc^2}{I} + 3\ln\gamma - 2\right), \tag{2.2}$$

where n_e is the density of electrons in the material, I is the ionization potential of the material, and γ is the electron relativistic gamma factor. This formula is changed slightly for positrons because the cross section for e^-e^- (Moller) scattering is different than for e^-e^+ (Bhabha) scattering [7].

In most materials, and for energies greater than 100 MeV, bremsstrahlung is the dominant process for electrons and positrons to lose energy. This process is very close to the pair production mechanism shown in Figure 2.2. The radiated photon energy spectrum falls off as $1/k$ where k is the energy of the emitted photon. At high energy the mean angle of the emitted photon is

$$\langle\theta_\gamma\rangle = \frac{mc^2}{E}, \tag{2.3}$$

and thus most radiation lies inside a narrow cone around the electron or positron [7]. The radiation length X_0 is defined to be the length over which an electron or positron

loses *on average* $1 - e^{-1}$ of its energy to bremsstrahlung, and is a function of the Z of the material. There is no analogue to the mean free path for electrons and positrons. Rather, they lose energy in a continuous stream of radiation as they traverse material [6]. The average rate of energy loss due to bremsstrahlung is [7]

$$\frac{dE}{dx} = \frac{n_e}{Z} E\sigma, \tag{2.4}$$

where σ is the cross-section for bremsstrahlung.

2.1.3 Electromagnetic showers

Due to the interactions of electrons, positrons, and photons described above, a rapid proliferation of secondary particles occurs when any of these particles travels through matter. Incident electrons and positrons radiate hard photons due to bremsstrahlung, and the emitted photons undergo pair production to create further electrons and positrons, which then radiate photons, and so on. A simple model of an electromagnetic shower has been developed by Heitler in which an electron or positron with energy $> \epsilon_C$ emits one hard photon after traveling exactly one radiation length [7]. Below the threshold energy, the electron and positron lose their remaining energy due to collisions [7],[6]. Each photon with energy greater than some threshold produces an electron/positron pair with equal energy after traveling one λ. This simple model is qualitatively accurate in describing the development of an electromagnetic shower. An example of such a shower is shown in Figure 2.3. As the shower develops, the average energy of the particles decreases until at some point no further multiplication of particles occurs. This depth is called the shower maximum. Most of the energy is deposited after the shower maximum by particles with energy < 4 MeV [6]. This means that most of the energy deposited by photons is deposited via Compton scattering or the photoelectric effect. Remaining electrons and positrons deposit their energy through ionization processes.

The lateral spread of electromagnetic showers is determined by the motion of electrons and positrons away from the axis due to multiple scattering, and by the direction of bremsstrahlung photons. There is a parametrization of this lateral spread

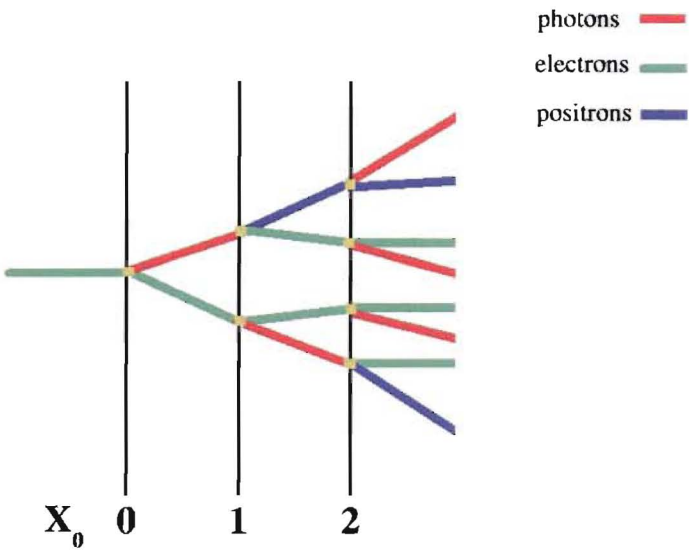

Figure 2.3: Cartoon of a simple electromagnetic shower using the Heitler model. The shower proceeds through three interaction steps, which yields 2^3 shower particles.

called the Moliere radius, defined as $\rho_M = mc^2\sqrt{4\pi/\alpha}\, X_0/\epsilon_c$. On average, $\geq 90\%$ of the shower energy is deposited inside the Moliere radius. Table 2.1 on page 23 contains a list of the radiation lengths, Moliere radii, and other properties for various materials commonly used in calorimeters.

2.2 Hadronic Calorimetry

Hadronic calorimetry is much more complicated than electromagnetic calorimetry because of the many more types of interactions that can occur. This section begins with a description of the main processes by which hadrons interact with matter. The strong interactions between the hadrons and nuclei often result in nuclear fission and high-multiplicity particle production which exhibit event-by-event fluctuations. These processes lead to the development of a hadronic shower, which is described in Section 2.2.3. Hadronic calorimeters are designed to measure the energy deposited by these hadronic showers.

2.2.1 Ionization

As mentioned in Section 2.1.2, all charged particles may deposit energy in matter by ionizing atoms. A semi-classical calculation is performed in [7], resulting in a general formula for the *average* rate of energy loss for a heavy, spin-0 particle:

$$\frac{dE}{dx} = c_0 T \left(\ln \frac{2p^2}{mI} - \beta \right), \tag{2.5}$$

where T is the kinetic energy and c_0 is a constant term depending on material and particle properties. The distribution of energy deposited exhibits large fluctuations and follows a Landau distribution. Since the $\frac{dE}{dx}$ depends on particle mass, it can be used for particle identification. All particles exhibit a minimum ionization rate of about 2 MeV/cm at $\beta\gamma \sim 3$. Particles in this energy regime are called minimum ionizing particles (MIPs).

2.2.2 Nuclear interactions

When a high-energy hadron strikes a nucleus, the most likely interaction is nuclear spallation [6]. In this process there is a short-lived cascade in which the struck nucleon passes large kinetic energies to other nucleons, followed by a slower release of particles from the nucleus. This process exhibits very large fluctuations: in one event a π^+ may strike a neutron in the reaction $\pi^+ + n \rightarrow p + \pi^0$ and most of the energy is passed on to the π^0. In another event the nucleus may disintegrate into many different hadrons. The binding energy barrier for nucleons to be kicked out of the nucleus in one of these collisions is not measured, and contributes to the uncertainties in measuring the energy of an incident particle. There are many subtle details which must be taken into account when designing a hadronic calorimeter[2].

[2]See [6] for more information.

2.2.3 Hadronic showers

When a high energy charged hadron enters a calorimeter, it will lose energy in a number of processes. On average, after penetrating some depth[3], the hadron will interact strongly with a nucleus as described in Section 2.2.2. For neutral hadrons, ionization does not occur and the only available option for losing energy is through nuclear reactions. In general, a proliferation of secondary mesons, nucleons, etc. will come from these hard collisions, which will further interact in the material, resulting in a hadronic shower. This will develop until a shower maximum, beyond which the particles are not energetic enough to produce more secondaries.

Conceptually then, a hadronic shower is similar to an electromagnetic one, as far as the cascade of particles is concerned. However, a hadronic shower is in general much more complicated structurally, and is subject to larger fluctuations[4]. In any hadronic shower there are significant amounts of energy deposited electromagnetically by hadrons such as π^0s and ηs through decays to $\gamma\gamma$. Therefore, within a hadronic shower, multiple electromagnetic showers will develop. The energy deposited by these 'sub-showers' is termed *EM energy*. As discussed in Section 2.2.2, there will also be a component of energy in a hadronic shower that is absorbed in nuclear breakups and excitations which is fundamentally undetectable in the calorimeter. This is called *invisible energy*. As well, there may be muons and neutrinos produced which will often escape the detector without being detected, taking with them *escaped energy*. An example of a hadronic shower, with approximate fractions of energy deposits of the various types is show in Figure 2.4. These fractions are only averages, and may fluctuate greatly event-by-event.

Due to the nature of the interactions, hadronic showers tend to be more diffuse than electromagnetic showers, and they propagate further in depth. This information can be used as a signal to identify the type of particle (i.e., hadronic or electromagnetic) which started the shower. Also, if a calorimeter is segmented longitudinally,

[3]This depth is called the nuclear interaction length, λ_{int}, and is analogous to the mean free path for photons described in Section 2.1.1.

[4]This is a statistical feature of hadronic showers. It is due to the large number of available processes by which an hadron may interact.

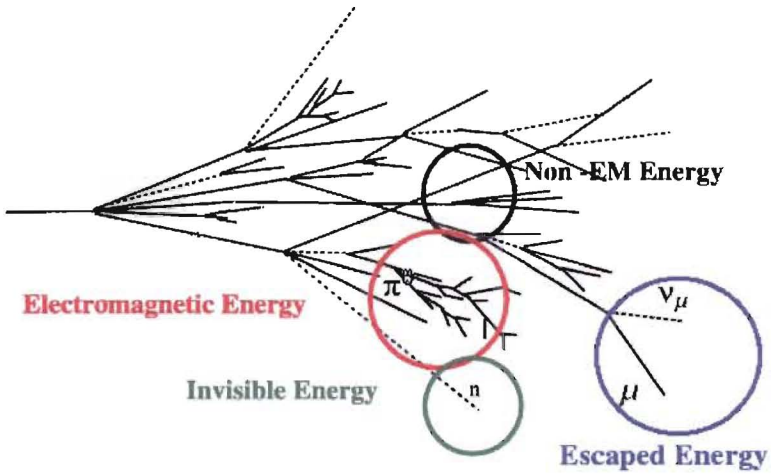

Figure 2.4: Example of a hadronic shower. The approximate fractions are EM energy $O(50\%)$; invisible energy $O(25\%)$; non-EM energy $O(25\%)$; escaped energy $O(2\%)$.

the depth information can be used to apply special calibrations to hadronic showers.

2.3 Compensation

An important difference between electromagnetic calorimetry and hadronic calorimetry has to do with the invisible and escaped energy in hadronic showers. In order to account for the invisible energy in hadronic showers, calorimeters are often designed to be *compensating*. This has the effect of enhancing the response[5] due to only non-EM, or hadronic energy deposition (defined as h), compared to the response due to EM energy deposition (called e) to make the ratio $e/h = 1$. Compensation is a desirable feature because it improves the linearity (see Section 2.3.1) and resolution of calorimeters. If a calorimeter design is non-compensating, the calibration for a hadronic shower changes event-by-event, according to fluctuations in the fraction of EM energy in the shower[6]. This is found to degrade the resolution of the measurement

[5]The response is defined as the ratio $E_{\text{measured}}/E_{\text{true}}$.

[6]Take for example a calorimeter with $e/h \gg 1$. Suppose that in one event 90% of the shower energy is EM, in which case the response will be ≈ 0.9. In another shower the EM energy component may be only 40%, in which case the response will be ≈ 0.4.

significantly [6].

Compensation is often achieved by using uranium or other neutron-rich materials which produce large numbers of fast neutrons in fission reactions. These neutrons induce fission in neighbouring nuclei, greatly enhancing the signal of the incident particle [6]. If a detector is non-compensating, there is also the possibility of using offline software techniques to apply special weights to the non-EM depositions within hadronic showers. This is the method employed by ATLAS.

2.3.1 Linearity

The average fraction of EM energy f_{em} in a hadronic shower grows with energy [9]:

$$f_{em}(E) = \alpha_0 \ln \frac{E}{E_{\text{scale}}}, \tag{2.6}$$

where $E_{\text{scale}} \approx 1\text{GeV}$ and α_0 is weakly energy dependent[7], but is often left as a constant. This equation can be understood in a simplified model where, in each nuclear reaction, $\pi^{\pm}$s and π^0s are produced in equal amounts. The $\pi^{\pm}$s propagate further into the shower and will produce further $\pi^{\pm}$s and π^0s in subsequent interactions. However, the decay to π^0s halts the hadronic decay chain because the π^0s only decay electromagnetically into two γs. Therefore the relative fraction of EM energy increases with the shower depth, and thus with the incident particle energy, as more and more $\pi^{\pm}$s convert into π^0s. Because of this, the fraction of invisible energy in a hadronic shower is also energy dependant. Based on this model, there is an alternative for Eq. 2.6 due to Groom [11] and Wigmans [6] which uses a power law parameterization

$$f_{em}(E) = 1 - \left(\frac{E}{E_0}\right)^{m-1}, \tag{2.7}$$

where E_0 is some scale energy and m is a parameter of the calorimeter. The two parameterizations are essentially equivalent, although Eq. 2.7 will be used less frequently in this study.

[7] It can be fit to the form $\alpha_0 = a_0 + a_1 \ln \frac{E}{E_{\text{scale}}}$ [10].

The measurement of energy in a hadronic shower is called linear if the response is independent of E_{true}. If compensation can be achieved, the linearity is greatly improved. This is because even though the relative fractions of EM and hadronic energy change with the energy of the hadronic shower, both components are measured with the same efficiency, so that the sum of the two is constant. However, in non-compensating calorimeters, the non-linearity in Eq. 2.6 is enhanced by the degree to which h is incorrectly measured. The measured response r of a hadronic shower is given by

$$\begin{aligned} r &= (1 - f_{em})h + f_{em}e \\ &= (e - h)f_{em} + h, \end{aligned}$$

and so if $e/h \neq 1$, the non-linear f_{em} term survives.

2.4 Sampling Calorimeters

Sampling calorimeters use various materials for measuring and developing electromagnetic or hadronic showers. A passive medium is used for shower development and an active medium is used to measure the energy of the particles in the shower. For sampling calorimeters which utilize ionization in the active medium, this structure has the benefit that the long Landau tail in the $\frac{dE}{dx}$ measurement is suppressed [12]. These calorimeters are used in high energy experiments primarily because they are much cheaper to construct for a given volume compared to homogeneous calorimeters.

In ATLAS there are two different types of sampling calorimeters used. The most common type is based on liquid argon (LAr) sampling, in which the charged particles in hadronic and electromagnetic showers ionize the LAr. This ionization current is proportional to the particles' incident energies. The other method of measuring the particle energies in ATLAS is with scintillating plastic. The particles create scintillation light in the plastic, which is read out with optical fibers to a photomultiplier tube (PMT). The PMT converts the light output into an electronic signal. This signal is also proportional to the energy of the incident particles.

A schematic of a sampling calorimeter is shown in Figure 2.5. The absorber is drawn in black, and the active material is red. Particle trajectories are shown in cyan, with the cyan dots corresponding to interactions in the absorber medium. The yellow dots indicate some sort of measurement, either by ionization of the active material, or by scintillation light. An important point to note is that not all particles are detected as they pass through the calorimeter. This leads to the so-called 'sampling fraction' which is defined as the energy deposited by MIPs in the active material compared to the total energy deposited in the calorimeter [6]. Fluctuations in this fraction contribute to the resolution with which a sampling calorimeter can measure the energy of an incident particle. However, the resolution is found to improve with $\sqrt{E}$ of the particle, which renders sampling calorimeters very useful for measurements of high-energy particles.

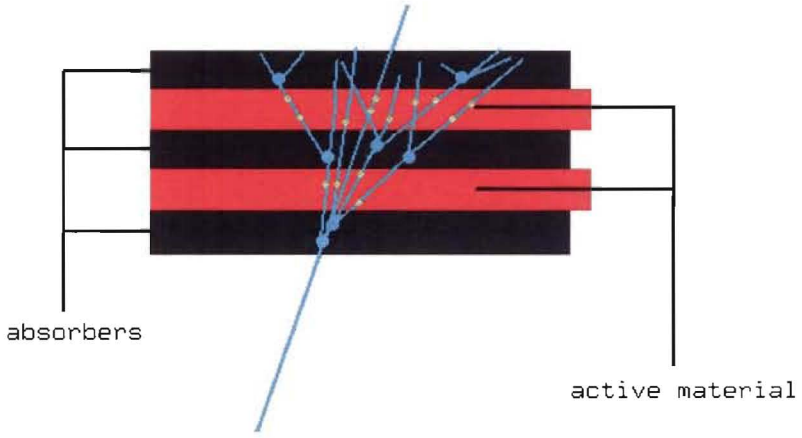

Figure 2.5: Schematic of a sampling calorimeter.

Passive Material	Z	Density (g cm^{-3})	E_c (MeV)	X_0 (mm)	ρ_M (mm)	λ_{int} (mm)
C	6	2.27	83	188	48	381
Al	13	2.70	43	89	44	390
Fe	26	7.87	22	17.6	16.9	168
Cu	29	8.96	20	14.3	15.2	151
Sn	50	7.31	12	12.1	21.6	223
W	74	19.3	8.0	3.5	9.3	96
Pb	82	11.3	7.4	5.6	16.0	170
^{238}U	92	18.95	6.8	3.2	10.0	105
Concrete	-	2.5	55	107	41	400
Glass	-	2.23	51	127	53	438
Marble	-	2.93	56	96	36	362
Active Material	Z	Density (g cm^{-3})	E_c (MeV)	X_0 (mm)	ρ_M (mm)	λ_{int} (mm)
Si	14	2.33	41	93.6	48	455
Ar (liquid)	18	1.40	37	140	80	837
Kr (liquid)	36	2.41	18	47	55	607
Xe (liquid)	54	2.95	12	24.0	42	572
Polystyrene	-	1.032	94	424	96	795
Plexiglas	-	1.18	86	344	85	708
Quartz	-	2.32	51	117	49	428
Lead-glass	-	4.06	15	25.1	35	330
Air 20^o,1 atm	-	0.0012	87	304 m	74 m	747 m
Water	-	1.00	83	361	92	849

Table 2.1: Material properties for various active and passive (absorbing) materials, including the critical energy (ϵ_c) for electrons, the radiation length (X_0), the Molière radius (ρ_M), and the nuclear interaction length (λ_{int}) [6].

Chapter 3

ATLAS Technical Overview

A complete oveview of the ATLAS detector is shown in Figure 3.1. Details of the subsystems are provided below.

3.1 Inner Detector

The basic function of the inner detector system is to track charged particles by detecting their interactions, called hits, at discrete points. The inner detector system is contained within a solenoidal magnetic field so that the curvature of the charged particle trajectories can be used to measure the particle momentum. Constraints for vertex resolution and tracking imposed by the physics goals of the experiment demand fine granularity detectors close to the interaction point (IP) in ATLAS. Such fine granularity is achieved with microstrip and pixel semiconductor tracking devices. A transition radiation tracker (TRT) is also located at the outermost radius of the inner detector. The TRT aids in electron identification and in providing further constraints on track fitting. The inner detector extends out to the edge of the electromagnetic barrel calorimeter. From the interaction region to the calorimeter, charged particles are tracked by (1) a pixel detector for $r \leq 20$cm, (2) silicon microstrips for $30.0 \leq r \leq 52.0$cm and (3) the TRT up to $r = 115$cm. There are also endcap detectors located at both ends of the barrel as listed in Table 3.1. The inner detector is illustrated in Figure 3.2.

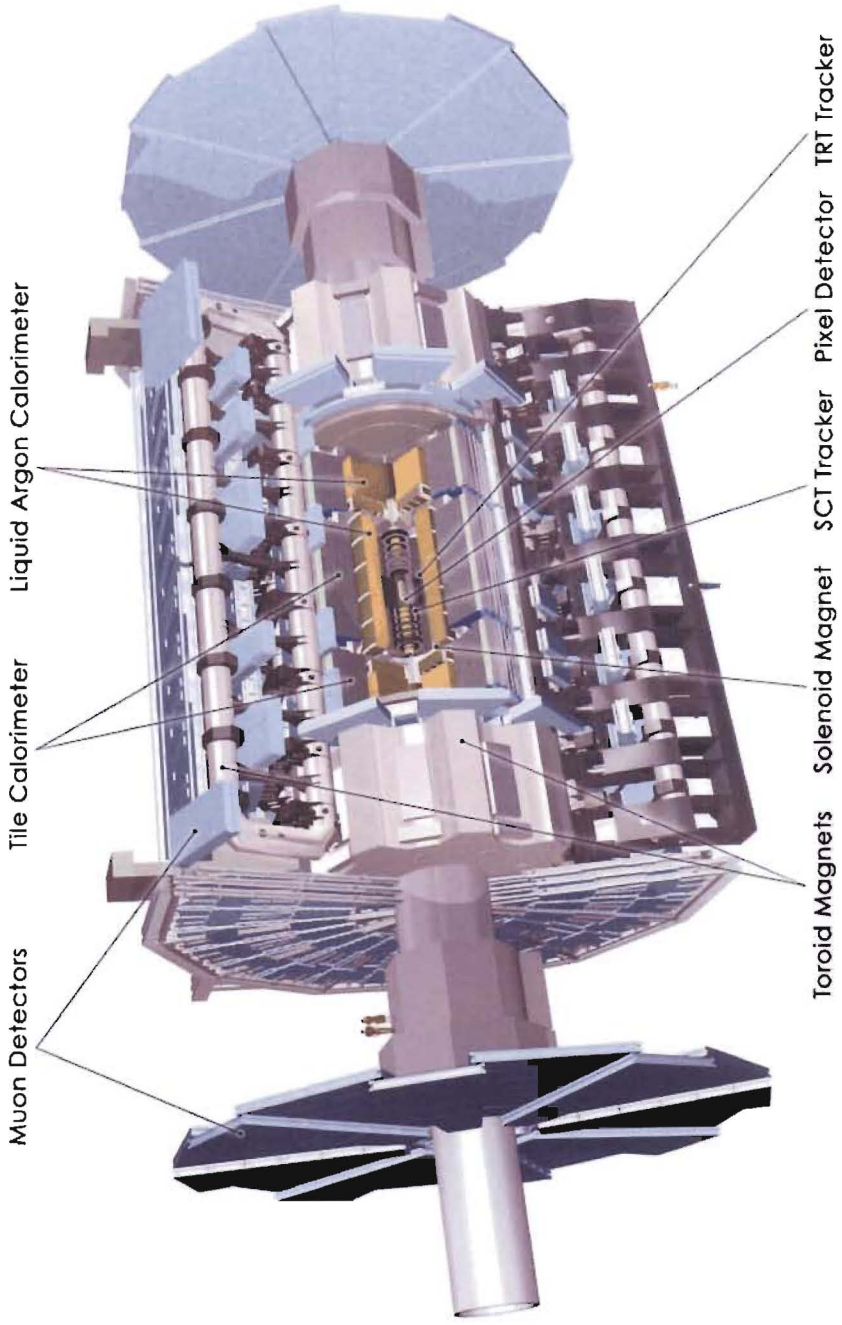

Figure 3.1: Overall layout of the ATLAS Detector, showing the location of the muon detectors, the tile calorimeter, the LAr calorimeters, the toroidal magnet system, the solenoid magnet, and the inner tracking system. ATLAS Experiment Image: Copyright CERN, [3]

System	Position	Channels (10^6)	η coverage
Pixels	removable barrel	16	± 2.5
	2 barrel layers	81	± 1.7
	10 endcap disks	43	1.7-2.5
Silicon strips	4 barrel layers	3.2	± 1.4
	9 endcap disks	3.0	1.4-2.5
TRT	barrel region	0.1	± 0.7
	radial endcap	0.32	0.7-2.5

Table 3.1: Overview of the ATLAS inner detector system [1]. See the text for more details.

Because the forward regions are characterized by high multiplicity and large radiation doses, the tracking covers only the η range $\pm$ 2.5, or $9^\circ \leq \theta \leq 171^\circ$ (this is considered suitable for most physics searches). Therefore, the region $|\eta| < 2.5$ is called the precision physics region. In optimizing the configuration, consideration was given to the amount of interacting material between the IP and the calorimeters in order to limit the number of photon conversions (pair production) and brehmstrahlung processes. Such processes are often unrecoverable in the reconstruction algorithms. More details can be found in [3].

3.2 Calorimetry

The ATLAS calorimeter system is comprised of five subsystems divided into barrel and endcap regions. The barrel region consists of a liquid argon (LAr) electromagnetic calorimeter (EMB) and presampler, and a scintillating plastic tile hadronic calorimeter (TILE). The endcap calorimeters are all based on LAr sampling technology: an electromagnetic presampler and endcap (EMEC), the hadronic endcap (HEC), and the forward calorimeter (FCAL). A summary of the calorimeter geometry is given in Table 3.2. The calorimeter system is illustrated in Figure 3.3.

EM Calorimeter	**Barrel**	**End-cap**	
Coverage	$\|\eta\| < 1.475$	$1.375 < \|\eta\| < 3.2$	
Longitudinal segmentation	3 samplings	3 samplings	$1.5 < \|\eta\| < 2.5$
		2 samplings	$1.375 < \|\eta\| < 1.5$
			$2.5 < \|\eta\| < 3.2$
Granularity ($\Delta\eta \times \Delta\phi$)			
Sampling 1	0.003×0.1	0.025×0.1	$1.375 < \|\eta\| < 1.5$
		0.003×0.1	$1.5 < \|\eta\| < 1.8$
		0.004×0.1	$1.8 < \|\eta\| < 2.0$
		0.006×0.1	$2.0 < \|\eta\| < 2.5$
		0.1×0.1	$2.5 < \|\eta\| < 3.2$
Sampling 2	0.025×0.025	0.025×0.025	$1.375 < \|\eta\| < 2.5$
		0.1×0.1	$2.5 < \|\eta\| < 3.2$
Sampling 3	0.05×0.025	0.05×0.025	$1.5 < \|\eta\| < 2.5$
Presampler	**Barrel**	**End-cap**	
Coverage	$\|\eta\| < 1.52$	$1.5 < \|\eta\| < 1.8$	
Longitudinal segmentation	1 sampling	1 sampling	
Granularity ($\Delta\eta \times \Delta\phi$)	0.025×0.1	0.025×0.1	
Hadronic Tile	**Barrel**	**Extended barrel**	
Coverage	$\|\eta\| < 1.0$	$0.8 < \|\eta\| < 1.7$	
Longitudinal segmentation	3 samplings	3 samplings	
Granularity ($\Delta\eta \times \Delta\phi$)			
Sampling 1 and 2	0.1×0.1	0.1×0.1	
Sampling 3	0.2×0.1	0.2×0.1	
Hardonic LAr		**End-cap**	
Coverage		$1.5 < \|\eta\| < 3.2$	
Longitudinal segmentation		4 samplings	
Granularity ($\Delta\eta \times \Delta\phi$)		0.1×0.1	$1.5< \|\eta\| < 2.5$
		0.2×0.1	$2.5< \|\eta\| < 3.2$
Forward Calorimeter		**Forward**	
Coverage		$3.1< \|\eta\| < 4.9$	
Longitudinal segmentation		3 samplings	
Granularity ($\Delta\eta \times \Delta\phi$)		$\approx 0.2 \times 0.2$	

Table 3.2: Detailed parameters of the ATLAS calorimeter system, including the granularities and longitudinal segmentations of the various subdetectors [1].

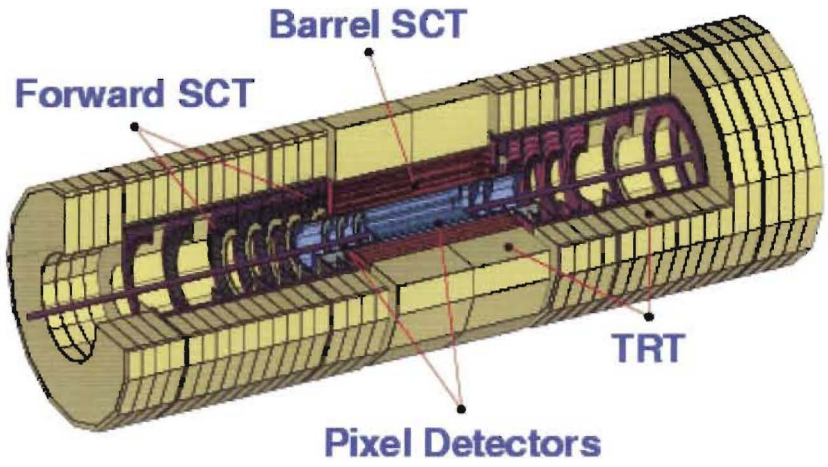

Figure 3.2: Layout of the ATLAS inner detector showing the location of the silicon pixel detectors, the barrel and forward silicon microstrip detectors, and the transition radiation tracker. ATLAS Experiment Image: Copyright CERN, [3].

3.2.1 Hadronic Tile Calorimeter

The hadronic tile calorimeter is a sampling calorimeter which uses iron as the absorbing material and scintillating plastic as the active material. The plastic tiles are staggered in depth and are connected at both sides to photomultiplier tubes via optical fibers. A geometrical overview of a segment of the TILE is shown in Figure 3.4. The readout cells are grouped projectively in η with a granularity of $\Delta\eta \times \Delta\phi = 0.1 \times 0.1$. The TILE has a total of 10,000 readout channels and is designed to produce fast signals from the scintillator. An electronic pulse shaper transforms the current pulse from the photomultiplier tubes in 50ns.

The TILE is shielded by the EMB calorimeter ($\approx 1.2\lambda$) and the coil of the solenoid used to generate the magnetic field for the inner detector. It is split into three sections: a central barrel region $\eta < 1.0$ and two extended barrel sections $0.8 < \eta < 1.7$. A vertical gap between these two regions contains cabling and service pipes for the EM calorimeters. The main function of the TILE is to provide a good measurement of the energy of jets (see Chapter 4) which make it through the EM calorimeters,

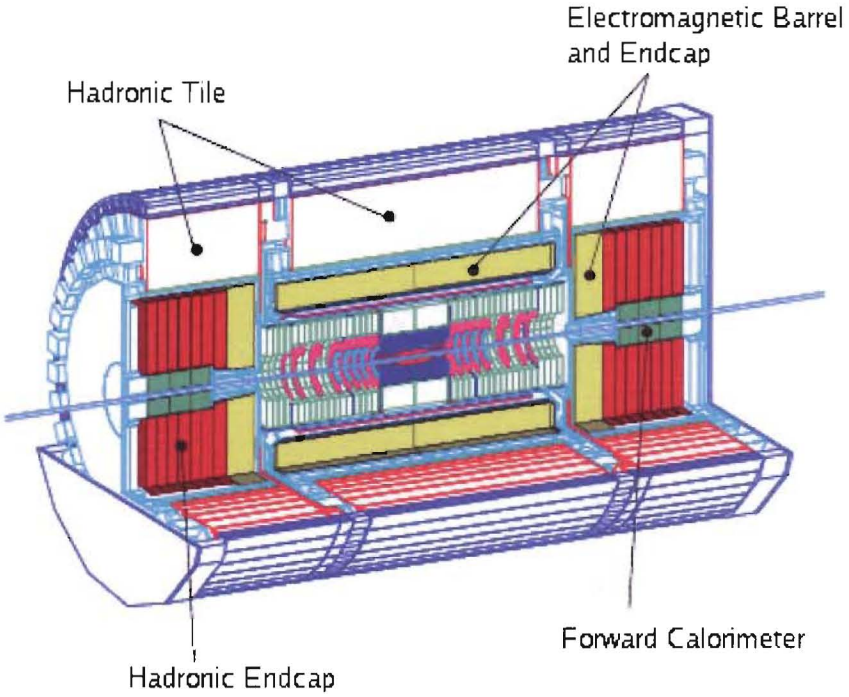

Figure 3.3: Overview of the ATLAS calorimetry system. The central core is the ATLAS inner detector. The hadronic tile (TILE) and electromagnetic barrel (EMB) calorimeters surround the inner detector. The ends of the barrel are capped by the electromagnetic endcap (EMEC), the hadronic endcap (HEC) and the forward calorimeter (FCAL). ATLAS Experiment Image: Copyright CERN, [13].

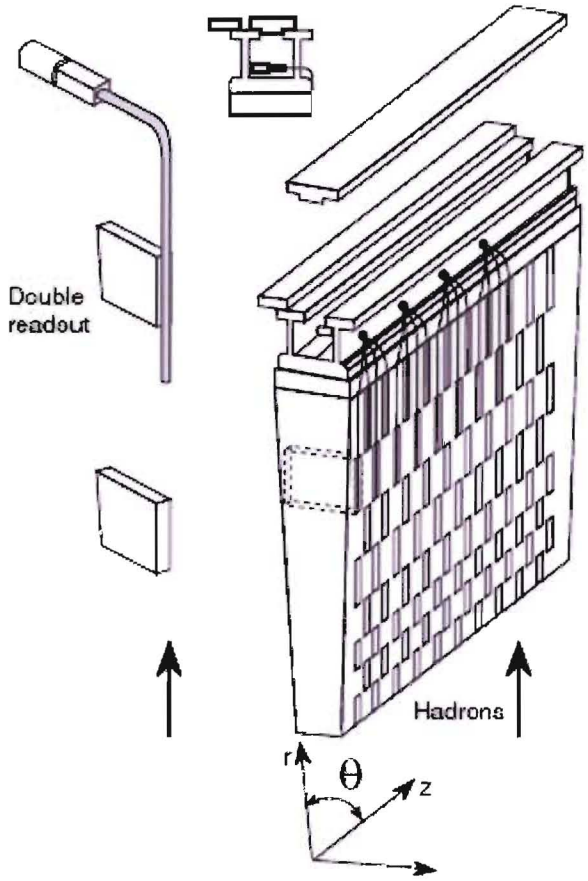

Figure 3.4: Schematic of the TILE calorimeter design. The direction of hadrons from the interaction point is shown by the upwards arrow. The scintillator tiles are arranged vertically within an iron absorber and are read out on both sides. ATLAS Experiment Image: Copyright CERN, [14].

and to improve the resolution of the $\not\!\!E_T$ measurement. Because the TILE is non-compensating (see Section 2.3), it was designed with longitudinal segmentation to allow for weighting of jet energies based on depth of energy deposition.

3.2.2 Electromagnetic Barrel and Endcap Calorimeters

The electromagnetic calorimeters in ATLAS consist of liquid argon sampling calorimeters using lead absorbers. In order to provide complete coverage in the ϕ coordinate without gaps between cells, the barrel and end-caps have an accordian geometry as shown in Figure 3.5. The absorber plates are 1.5mm lead sandwiched between 0.2mm stainless steel in the barrel, but vary in thickness with radius over two regions of the end-cap calorimeter. The reason for this is to compensate for the increase in the amplitude of the accordian wave with radius in the end-cap (see Figure 3.7). As shown in Figure 3.6, there are significant amounts of inactive material in front of the EM calorimeters. In order to correct for the energy lost in these regions, a presampler is placed in front of the EM calorimeter and is read out independantly. The energy in the presampler is weighted to recover the correct energy for particles which begin to shower before reaching the calorimeters. The η-strip geometry also allows for precision measurements of the shower geometry in the early stages of shower development, which is useful for EM/hadron separation and for precision measurement of the invariant mass of γ's from $H \rightarrow \gamma\gamma$. In the gap between the barrel and end-cap, there is a also a scintillator which is used to recover energy of particles which are otherwise undetected in this region. This is important because the gap is in the 'precision physics' region $|\eta| < 2.5$.

3.2.3 Hadronic Endcap Calorimeter

The hadronic endcap calorimeter is also a LAr sampling calorimeter, but it employs copper as the absorbing material instead of lead, as in the EM calorimeters. Each endcap consists of two independant wheels, which contain 25mm and 50mm copper plates respectively, interspaced with 8.5mm LAr gaps which are divided by three parallel electrodes into four drift spaces of about 1.8mm. Of the three electrodes, only

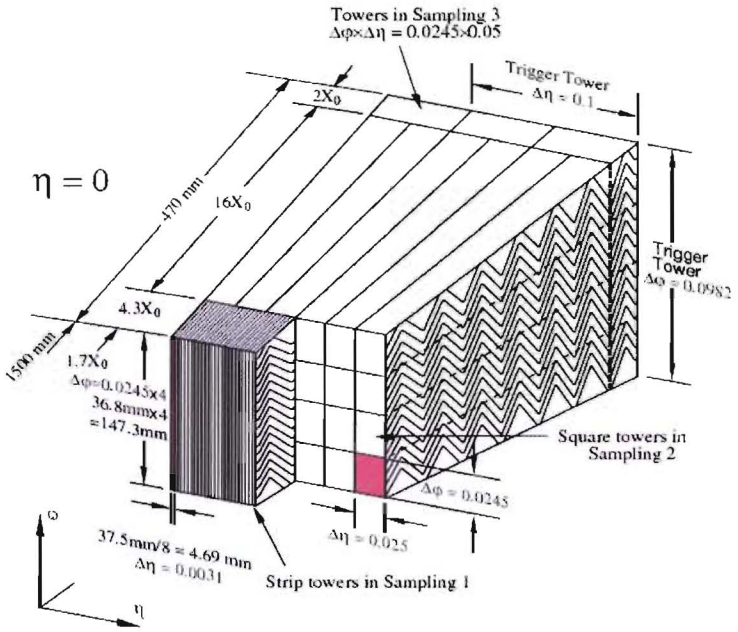

Figure 3.5: Sketch of the accordian structure of the EM barrel calorimeter. This figure shows the granularity and depth, measured in electron radiation lengths (X_0, see Section 2.1.2), for the three longitudinal layers in the EMB. These are shown for a readout section centered at $\eta = 0$. ATLAS Experiment Image: Copyright CERN, [13].

the central electrode is readout. The reason the gap is divided into four drift volumes is to minimize the time needed for ions to drift across, and therefore to prevent ion buildup due to high particle multiplicities [15]. A schematic of the readout structure is shown in Figure 3.8. Each HEC wheel is constructed from 32 identical modules in ϕ so that each module covers $\Delta\phi \simeq 0.1$. The cells in this calorimeter are fully projective from the IP in ϕ, but only nearly projective in η. In order to maximize coverage in the transition region at $|\eta| = 3.1$ between the HEC and the forward calorimeter, the EMEC extends to $|\eta| = 3.2$.

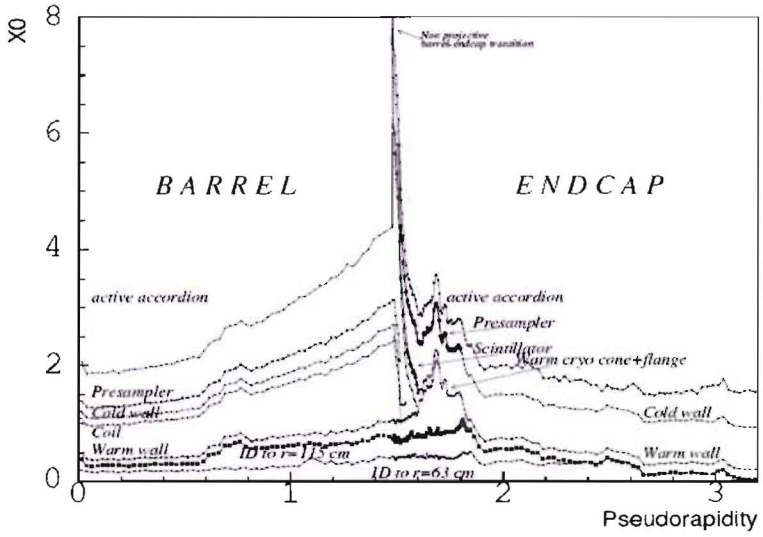

Figure 3.6: Dead, or inactive material in front of the EM barrel and endcap calorimeters, measured in electron radiation lengths, and shown as a function of η. The various contributions to the total dead material are detailed separately. ATLAS Experiment Image: Copyright CERN, [13].

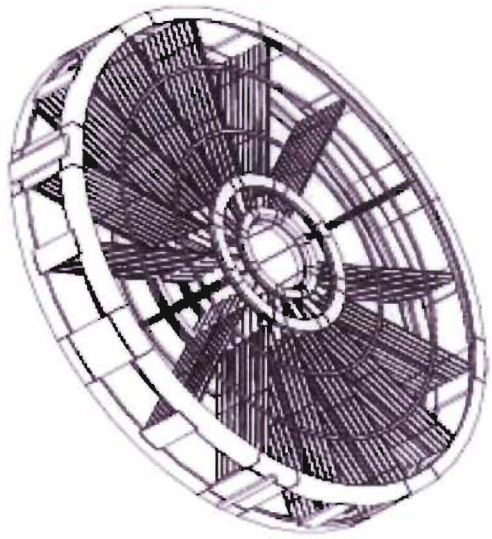

Figure 3.7: Sketch of the EM end-cap calorimeter. This sketch shows the accordian structure in the two radial sections (inner and outer wheel) of the EMEC. ATLAS Experiment Image: Copyright CERN, [13].

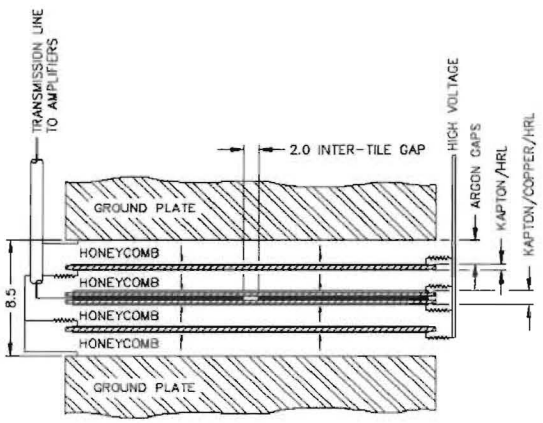

Figure 3.8: Electrode readout structure of the hadronic endcap calorimeter. See text for details. ATLAS Experiment Image: Copyright CERN, [13].

3.2.4 Forward Calorimeter

The liquid argon forward calorimeter is in a very high radiation zone. Because the jets in this region have very high energies, the FCAL consists of three sections: the forward region (the EM region), built of copper, and the rear two sections built of high-density tungsten so as to reduce punch-through into the muon system and lateral leakage into the HEC [1]. The FCAL is primarily used for tagging high energy jets in the forward region and for reducing radiation background in the muon detectors.

The FCAL employs an interesting geometry. Each calorimeter section consists of a metal matrix with regularly spaced longitudinal channels. These channels are filled with rods and concentric LAr gaps. The rods are held at a high voltage while the matrix is held at ground. This geometry allows for very narrow LAr gaps, which reduces the timescale of the current signals across the gaps, thus reducing significantly the levels of background signal due to the very high radiation environment. A diagram of this geometry is shown in Figure 3.9.

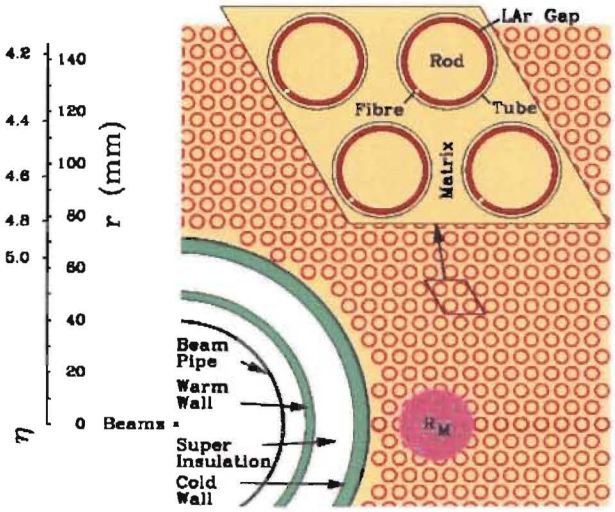

Figure 3.9: Sketch of the FCAL rod & matrix geometry. See text for explanation. ATLAS Experiment Image: Copyright CERN, [13].

3.3 Muon Spectrometer

The muon spectrometer is designed to measure the momentum of muons by measuring track curvatures in the ATLAS toroidal magnetic field. The spectrometer consists of four subsystems: the monitored drift chambers (MDT), the cathode strip chambers (CSC), the resistive plate chambers (RPC) and the thin gap chambers (TGC). The latter two subsystems are used for triggering in the muon system. An overall view of the muon system is show in Figure 3.10. The MDT is a drift tube chamber while the CSC is a multiwire proportional chamber. However, both systems work on a similar principle. When charged particles pass through the chambers, they ionize the chamber gas (an Ar and CO_2 mixture). The liberated electrons drift towards the anode wire and generate a measurable current to indicate the presence of a passing muon. The RPC and TGC chambers also work similarly, although in these systems there is no anode wire but only charged plates.

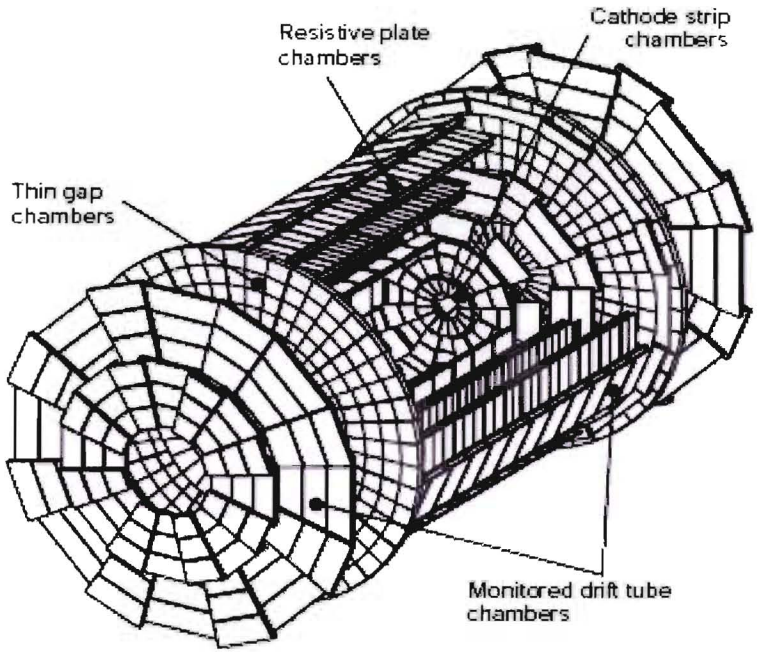

Figure 3.10: Overview of the main components of the ATLAS muon detector. ATLAS Experiment Image: Copyright CERN, [1].

3.4 ATLAS Software

Studies of the ATLAS detector require good Monte Carlo simulations of the physics processes and detector responses. Athena [16] is a software framework that has been developed for ATLAS. This framework consists of software to manage Monte Carlo simulations and also reconstruction of the detector signals during real running. A flow diagram of the main stages in data processing is shown in Figure 3.11. Various official productions[1] of simulated data have been produced with various detector geometries and Athena versions. As well, unofficial productions have been produced for this study using Athena software releases 10.0.1, 11.0.41, and 12.0.3. The development of the software is an ongoing process.

[1]https://twiki.cern.ch/twiki/bin/view/Atlas/MonteCarloProductionPolicy

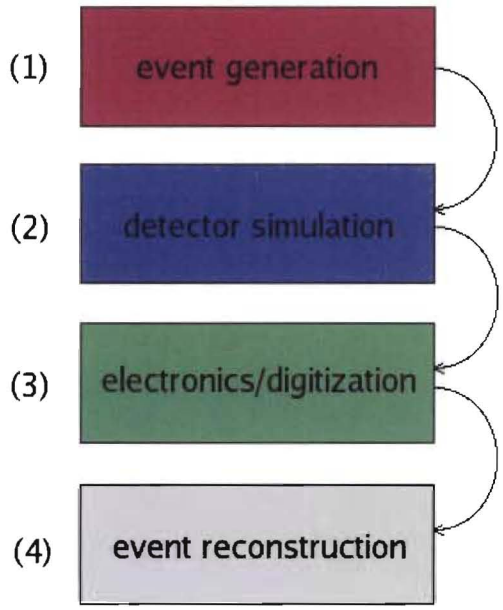

Figure 3.11: Various stages of simulated data in the Athena framework: (1) event generation is performed using any number of event generators such as Pythia, Herwig, MC@NLO, etc.; (2) detector simulation uses the Geant4 framework to simulate the passage of particles through matter; (3) electronics pulses are calculated from the output of the Geant4 simulation stage. Electronics and pileup noise are added at this stage; (4) events are reconstructed from the electronics output of the detector. Steps (1) - (3) simulate the detector. The last step is used for both simulated and real data.

Chapter 4

Jets

Loosely defined, jets are collimated sprays of hadrons. They are colour singlets produced from 'bare' quarks and gluons, and are the most common decay products in p-p collisions at ATLAS.

A number of Monte Carlo programs have been compiled to model the production of hadrons from quarks and gluons. The physics motivation for the models in these programs is that, as particles with colour charge are separated, the energy in the field between them grows to the point that a colour/anti-colour pair can be produced in the vacuum. In the Monte Carlo programs this process is known as the parton shower, and is repeated many times for quarks and gluons that scatter with large momenta. After this, the colour charges recombine into colour singlets, or hadrons, in a process called hadronization. The overall process of parton showering and hadronization is referred to as fragmentation.

The overall evolution of a jet in the ATLAS detector can be divided roughly into three stages as shown in Figure 4.1. In the first stage, the *parton level* jet consists of a bare parton[1] scattering in a p-p collision. The second stage, called the *particle level* jet, follows hadronization and consists of colour-singlet baryons and mesons. Finally, as the particles enter the detector and begin to shower, the *calorimeter level* jet is developed. The signals in the detector produced by the calorimeter level jet

[1]This parton may radiate multiple gluons, known as final state radiation (FSR).

must be reconstructed and calibrated back to the parton level in order to investigate the short-distance physics of an event. There are complicated physics effects in the

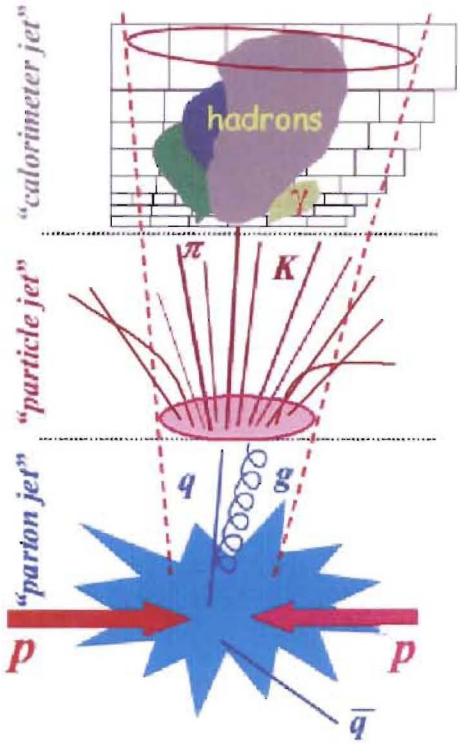

Figure 4.1: The three regimes in the evolution of a jet: parton level, particle level, and calorimeter level.

development of jets including (among others)

- quark fragmentation/hadronization - dependence on the particular model used results in a systematic uncertainty on jet measurements
- underlying event - the scattered debris from the p-p collisions can overlap with jets from the hard scatter of interest.

These unavoidable physics effects must be disentangled from detector design effects on the measurement of jets, including

- non-compensation - since jets are comprised of hadrons, the measurement of calorimeter level jets exhibits large fluctuations, as described in Sections 2.2.3 and 2.3
- electronics/pileup noise - multiple interactions (see Chapter 6) and electronics noise will distort the signals produced by jets
- dead material & leakage - not all of the energy in a jet will be deposited in the calorimeter.

Thus, developing a robust strategy for properly measuring jets is a very complicated undertaking.

4.1 Jet Reconstruction

The first step in going back to the parton level jet is to cluster the signals from the calorimeter cells in order to resolve jet structures. There are a number of software algorithms to do this, as described in [17]. Currently, the Athena framework implements various versions of cone and k_T algorithms, which are described below.

4.1.1 Cone Jet Algorithms

Cone jet algorithms are geometrically motivated by the notion that jets should be collimated in cones in $\eta - \phi$ space[2]. The most common cone algorithm is the seeded cone algorithm. There are various complicated versions which are deemed more theoretically stable [17], but only the seeded cone algorithm is used for this study. The inputs to the seeded cone (SC) algorithm in ATLAS are projective calorimeter towers or topological clusters (see Section 6.4). For this study, projective towers are used. Calorimeter towers are projections in depth from the interaction point, of granularity $\Delta\eta \times \Delta\phi \approx 0.1 \times 0.1$. These towers comprise a simple grid structure in $\eta - \phi$ space, as in Figure 4.2. The towers are assumed to be massless particles with 4-vectors

[2]Cone algorithms create cones in $\eta - \phi$ space, but not in real space. For example, cones in the forward region have very irregular shapes in real space.

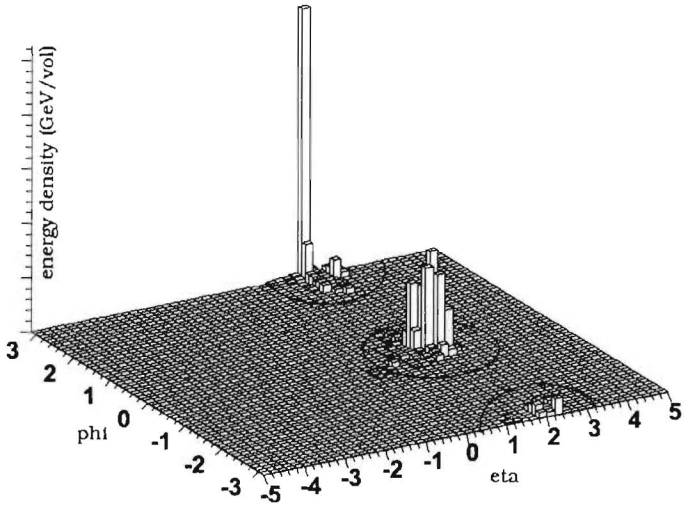

Figure 4.2: Energy density in an $\eta \times \phi$ grid, from a typical simulated γ + jet event, using Athena software r11.0.41. The photon is centered at $(\eta, \phi) \approx (2.0, \pi)$. The hardscatter jet is back-to-back from the photon at $(\eta, \phi) \approx (2.0, 0.0)$. Cone and kT jet algorithms will classify both energy depositions as stable jets. Example cones are shown drawn around the photon and the jet.

$E^i = (|\mathbf{p}^i|, \mathbf{p}^i)$ and coordinates (ϕ^i, η^i). A cone consists of all towers within a radius ΔR of the cone centroid, where the radius is a parameter of the algorithm[3]. The algorithm looks at all towers above the seed threshold[4] and proceeds as follows [17]:

- calculate the energy-weighted centroid of a cone placed about the geometric center of the seed tower
- use this centroid as the seed for a new tower and iterate until a stable solution is found.

The centroid coordinates of a cone C are calculated as

$$\eta^C = \frac{\sum_{i \subset C} E_T^i \eta^i}{E_T^C} \tag{4.1}$$

$$\phi^C = \frac{\sum_{i \subset C} E_T^i \phi^i}{E_T^C}. \tag{4.2}$$

[3]In Athena there are two default sizes of $\Delta R = 0.4$ and 0.7 for the seeded cone algorithm.

[4]The default is 1.0 GeV in ATLAS.

A stable solution is found when the change in the energy centroid during one iteration falls below some threshold, or a maximum number of iterations is reached. For each new cone, the algorithm checks if the stable solution was found previously, and ignores it if it already exists. Cone jets which overlap are dealt with in a split-merge algorithm that merges jets with overlap fractions greater than some threshold. An example of a cone jet algorithm applied to a γ + jet event is shown in Figure 4.2.

4.1.2 k_T Algorithms

In the k_T algorithm, solutions are based on closeness in momentum space rather than geometric space. Theoretically, these algorithms select particles which are nearby in momentum space (small relative transverse momentum) to create jets. Generally, k_T jets have a much more complicated topology than cone jets, since the shapes can be very irregular in $\eta - \phi$ space, and underlying event energy may be pulled in with large event-by-event fluctuations.

The inputs to the ATLAS k_T algorithm are also projective towers as in the SC algorithm. In k_T algorithms these inputs are called preclusters. In an attempt to suppress noisy contributions, an initial cut of 10 MeV is applied to all preclusters. The algorithm proceeds as follows [17]:

- for each precluster i, define

$$d_i = p_{T,i}^2 \tag{4.3}$$

  and for each pair (i, j) of preclusters,

$$\begin{aligned} d_{ij} &= \min(p_{T,i}^2, p_{T,j}^2)\frac{(\eta^i - \eta^j)^2 + (\phi^i - \phi^j)^2}{D^2} \\ &= \min(p_{T,i}^2, p_{T,j}^2)\frac{\Delta R_{ij}}{D^2} \end{aligned} \tag{4.4}$$

  where D is a parameter of the algorithm. For $D = 1$ and small ΔR_{ij}, d_{ij} is the minimal relative transverse momentum of one precluster with respect to another [17].

- find the minimum of all d_i and d_{ij} and label it $d_{\min}$

- if d_{min} is a d_{ij}, remove preclusters i and j and replace them with a merged precluster
- if d_{min} is a d_i, then the precluster is isolated in momentum space, and can be removed from the list of preclusters and added the list of output jets.

These steps proceed until no further preclusters remain. Overall this algorithm produces a list of jets separated by $\Delta R > D$ [17]. In non-compensating calorimeters a special hadronic calibration should first be applied to preclusters before the k_T algorithm will work properly, because the output depends so strongly on the energy of the preclusters [12]. Also, in events with large contributions from underlying event and pileup, the k_T algorithm may have the undesirable effect of combining preclusters which are not really from the same jet. Detailed studies are required before this algorithm can be used in all environments.

4.2 Jet Calibration

Once the jet structures have been resolved, calibration procedures have to be applied to remove detector design and clustering effects. Clustering corrections depend on the algorithm used to reconstruct the jets, and may include out-of-cone or underlying event corrections [18]. The ultimate aim is to get an accurate measurement of the properties of the particle-level jet. This is discussed in Chapter 5.

Chapter 5

Jet Energy Scale

The jet energy scale calibrates the measured calorimeter level jet energy to the particle level. This calibration must account for non-compensation, dead material and other detector effects, as well as algorithm specific biases. Model and physics-dependent corrections are needed to go back to the parton level. For many analyses, the knowledge of the jet energy scale is the leading systematic uncertainty [10], and some ATLAS physics goals require the jet energy scale to be known to within 1% [1]. This strongly motivates developing a method to derive and monitor the jet energy scale. In this chapter, a method for measuring the jet response part of the jet energy scale is presented. The discussion begins in Section 5.1 with an overview of *in situ* calibration. Section 5.2 deals with the jet response measurement, the most significant component of the jet energy scale. A scheme for measuring the jet response is presented in Section 5.3. This scheme is used in Section 5.4 to simulate an in situ measurement of the jet response in ATLAS.

5.1 In-situ Calibration

There are currently two ways of calibrating jets in ATLAS, as shown in Figure 5.1. Both schemes rely on a basic calibration called 'EM scale' which sets the correct energy

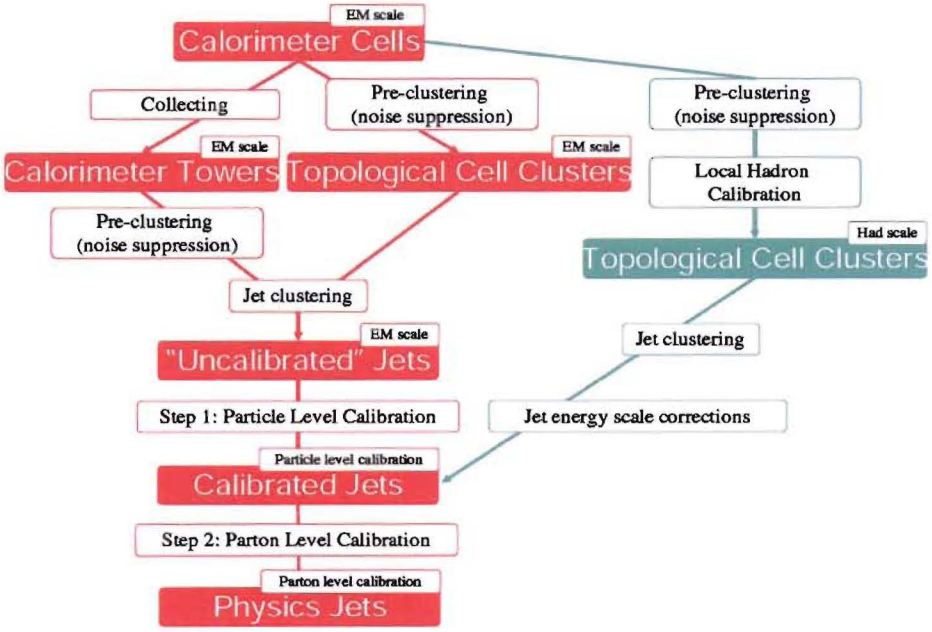

Figure 5.1: The calibration scheme envisioned for jets in ATLAS. There are two complementary schemes. The path on the right outlines a local hadronic calibration procedure which sets the correct energy scale for the inputs to the jet algorithms. The path on the left details a calibration for jet structures (see text for more details). Copied from [19].

for electrons and photons. In the local calibration scheme[1], calibration constants based on cell energy densities or topological cluster quantities are derived from Monte Carlo simulations and test beam data. The jet algorithms are run using the calibrated clusters or cells as inputs. In the alternate scheme, which also relies on Monte Carlo, calibrations are applied after jet structures have been resolved. Examples of such a scheme are the PESA calibration procedure [20] and the H1 jet calibration [21].

In order to properly set the jet energy scale for either method, there should be an in situ cross-check of the calibrations derived from the Monte Carlo simulations [22]. The jet energy scale can be found in situ for the ATLAS calorimeters by using momentum balance between an electromagnetic particle and a jet as in Z/γ + jet events. In these events the Z and γ interact electromagnetically[2], and since the calorimeters are tuned to the EM scale, they will be measured correctly. By considering momentum balance in the transverse plane[3], a correct calibration for the jet can be derived. Another method is by looking at $W \rightarrow jj$ (W decaying hadronically into two jets) events. The known W mass can be used to constrain the true energy of the jets, which can be compared to the measured calorimeter level energy.

For this study, momentum balance in γ + jet events is used to calculate the jet energy scale. The leading order Feynman diagrams for these events are shown in Figure 5.2. The 'Compton-like' scatter process (ISUB=29 in Pythia) is dominant at ATLAS over the quark annihilation process (ISUB=14 in Pythia)[4] as shown in Figure 5.3. The total cross section for γ + jet events at the Tevatron[5] is shown in Figure 5.4.

---

[1]The basis of this method is that hadronic showers are more diffuse than electromagnetic ones and thus cells with low energy density are weighted up, in order to achieve compensation.

[2]The photon will shower as described in Section 2.1.3. The Z will quickly decay to either e^+e^-, $\mu^+\mu^-$, $\tau^+\tau^-$ or $q\bar{q}$. Only the events in which the Z decays to an e^+e^- or $\mu^+\mu^-$ pair are useful here. The e^+e^- will interact as described in Section 2.1.2. The energies of the $\mu^+\mu^-$ are measured by the muon spectrometer.

[3]The net transverse momentum is only ≈ 0 in ATLAS because the partons have a relative momentum k_T within the colliding protons such that the CM of the parton scatter is not the CM in the lab frame. This effect is limited to $\langle k_T \rangle = 0.44\text{GeV/c}$, the Pythia default. It is reasonable to expect $k_T \leq 1.0\text{GeV/c}$ [23].

[4]Hard scatter processes are turned on in Pythia by setting certain Fortran variables, such as ISUB

[5]These plots will be different for the LHC because of the higher CM energy, and because the LHC is a p-p collider, while the Tevatron is a p-$\overline{\text{p}}$ collider.

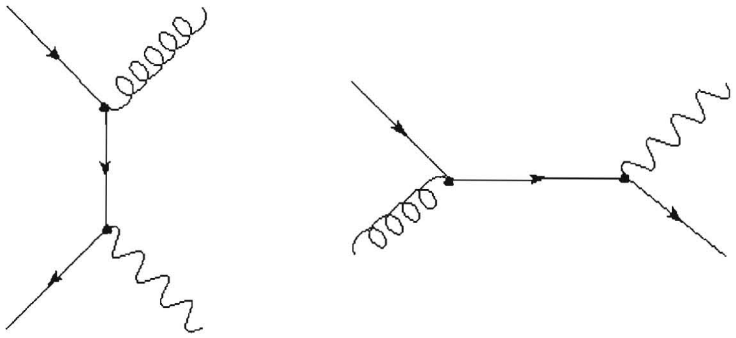

Figure 5.2: Feynman diagrams for (left) quark annihilation and (right) 'Compton-like' γ + jet production processes.

We find two advantages in using γ + jet events over Z + jet and $W \rightarrow jj$ events. First, γ + jet event rates are much higher (no suppression by leptonic branching ratios, and considerably smaller CM energy compared to events in which the W or Z has the same transverse momentum) and second, the Z + jet and $W \rightarrow jj$ processes may both be affected by new physics [24]. However, studies using Z + jet and $W \rightarrow jj$ events are certainly complementary, especially since the dilepton trigger is expected to have a much higher rate than the photon trigger at low transverse energies.

pysubs ckin 3	*minimum cut on* p_T
pysubs ckin 4 -1.	*no maximum cut on* p_T
pysubs msub 14 1	*turn on quark annihilation process*
pysubs msub 29 1	*turn on gluon scatter process*

Table 5.1: Pythia datacard options used to generate γ + jet events for this study. The parameter `ckin 3` was set to various p_T thresholds.

5.2 Jet Response

The jet response is a measure of the calorimeter response to the hadrons inside jets, and is the leading contribution to the jet energy scale calibration. The response to a

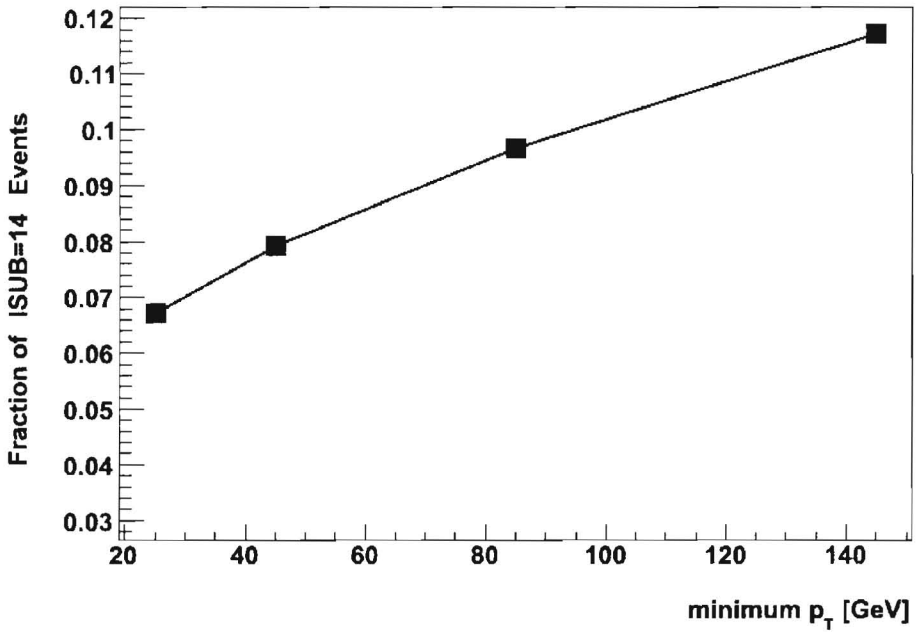

Figure 5.3: Fraction of $q\overline{q}$ annihilation events in γ + jet events, shown as a function of cut on minimum p_T^{γ}. This was calculated using Pythia 6.22 with the datacards in Table 5.1.

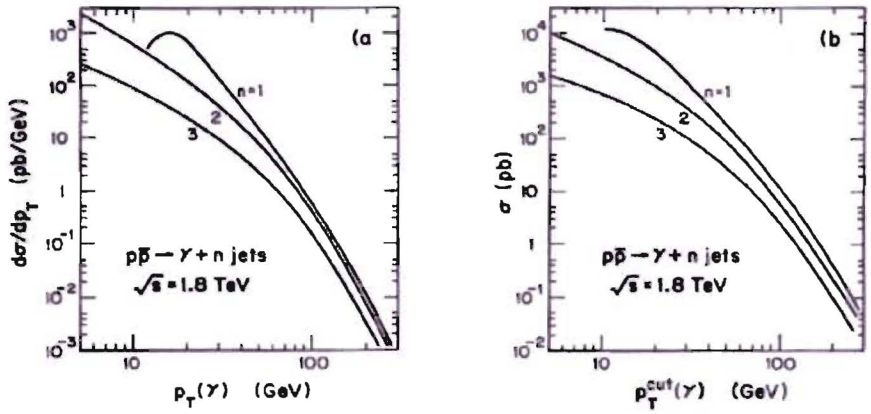

Figure 5.4: Photon transverse momentum distributions for $p\overline{p} \rightarrow \gamma +$ jet events at the Tevatron. The curves are for $n = 1, 2$ and 3 jets. Shown are the differential distribution (left) and the integrated cross section (right) as a function of the transverse momentum of the γ [24].

single incident hadron of energy E showering in the calorimeter is given by

$$r(E) = f_{em}(E)e + [1 - f_{em}(E)]\, h, \tag{5.1}$$

where $f_{em}(E)$ is the fraction of EM energy in the hadronic shower, and e, h are the response of the calorimeter to EM and hadronic energy depositions. A typical jet consists of particles such as π^0 and η mesons that decay only electromagnetically and thus produce EM showers, as well as charged and neutral hadrons such as protons, neutrons and $\pi^{\pm}$ mesons which initiate hadronic showers. Therefore, the overall jet response for a jet with energy E can be written as

$$j(E) = w_h\, r(w_h \cdot E) + w_{em}\, e(w_{em} \cdot E), \tag{5.2}$$

where w_h and w_{em} are the fractions of hadronic and electromagnetic particles in the jet at particle level. These fractions are determined solely by the fragmentation and hadronization processes, and are independent of the shower development in the calorimeter. It is assumed that w_h and w_{em} are independent of E. Using the parametrization in Eq. 2.6 for $f_{em}(E)$ and the energy dependence of α_0,

$$\alpha_0(E) = a_0 + a_1 \ln \frac{E}{E_{\text{scale}}}, \tag{5.3}$$

and assuming that e, h are independent of energy, the jet response can be parametrized by

$$j(E) = b_0 + b_1 \ln \frac{E}{E_{\text{scale}}} + b_2 \ln^2 \frac{E}{E_{\text{scale}}}, \tag{5.4}$$

where the constants w_h, h, w_{em}, and e have been absorbed into the constants b_0, b_1 and b_2. If we instead use the power law parameterization for $f_{em}(E)$ given in Eq. 2.7, the jet response is given by

$$j(E) = b_0 + b_1 \left(\frac{E}{E_0}\right)^{b_2 - 1}. \tag{5.5}$$

In this parameterization,

$$\begin{aligned} b_0 &= w_h\, e + w_{em}\, e = e \\ b_1 &= w_h(h - e) \\ b_2 &= m, \ \text{(see Section 2.3.1).} \end{aligned}$$

The ATLAS calorimeters are non-compensating ($e > h$) and therefore $b_0 > 0$ and $b_1 < 0$. These constraints are used in fitting $j(E)$ with the power law parameterization.

Using either parameterization, and by measuring the jet response as a function of measured jet energy, an in-situ calibration can be obtained using

$$E^{calib} = E^{meas} \cdot \frac{1}{j(E^{meas})}. \tag{5.6}$$

To achieve the absolute jet energy scale correction, further corrections for out-of-cone contributions, underlying event, etc. have to be applied. The jet response correction is by far the largest correction, especially for low energy jets.

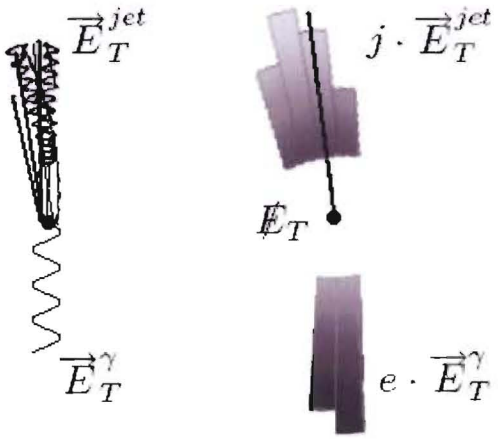

Figure 5.5: Momentum balance in γ + jet events at particle level (left) $\vec{E}_T^{\gamma} + \vec{E}_T^{\text{jet}} = 0$ and at calorimeter level (right) $e \cdot \vec{E}_T^{\gamma} + j \cdot \vec{E}_T^{\text{jet}} = -\not{E}_T$

5.3 $\not{E}_T$ Projection

In order to study the jet response separately from other effects, it is necessary to use quantities which are sensitive only to the response j [22]. Simply balancing the p_T of the jet and photon can result in undesirable dependencies on jet algorithms and models of underlying event distributions. An alternative approach is to use the $\not{E}_T$ projection fraction method (MPF), as described in the following section. This

method was used with success to set the jet energy scale in the DØ experiment [18]. The usefulness of this approach is that it is independent of the jet algorithm used to define the jet, and it is not affected by underlying event energy.

5.3.1 The MPF

At the parton level, momentum conservation between the photon and jet gives

$$\overrightarrow{E}_T^{\gamma} + \overrightarrow{E}_T^{parton} = 0. \tag{5.7}$$

In an ideal calorimeter, the photon and jet also satisfy the particle level momentum balance equation

$$\overrightarrow{E}_T^{\gamma} + \overrightarrow{E}_T^{jet} \approx 0, \tag{5.8}$$

neglecting fragmentation and hadronization effects. However, in the ATLAS calorimeters, the calorimeter level balance equation as shown in Figure 5.5 is modified to

$$e\,\overrightarrow{E}_T^{\gamma} + j(E_{jet})\,\overrightarrow{E}_T^{jet} = -\overrightarrow{\not{E}}_T, \tag{5.9}$$

where e, j are the EM and jet response of the calorimeters respectively. Anticipating that the EM scale can be measured well enough with $Z \rightarrow ee$ and π^0 data so that $e \approx 1$, this equation reduces to

$$\overrightarrow{E}_T^{\gamma} + j(E_{jet})\,\overrightarrow{E}_T^{jet} = -\overrightarrow{\not{E}}_T.$$

We can then project the quantities in the direction of the photon to yield

$$E_T^{\gamma} + j(E_{jet})\overrightarrow{E}_T^{jet} \cdot \hat{n}_{\gamma} = -\hat{n}_{\gamma} \cdot \overrightarrow{\not{E}}_T,$$

where $\hat{n}_{\gamma}$ is the unit vector in the direction of the photon. Using Eq. 5.8, this simplifies to

$$\begin{aligned} j(E_{jet}) &= 1 + \frac{\hat{n}_{\gamma} \cdot \overrightarrow{\not{E}}_T}{E_T^{\gamma}} \\ &= 1 + \frac{\overrightarrow{E}_T^{\gamma} \cdot \overrightarrow{\not{E}}_T}{(E_T^{\gamma})^2}. \end{aligned} \tag{5.10}$$

The term $\frac{\hat{n}_\gamma \cdot \vec{\not{E}}_T}{E_T^\gamma}$ is called the missing E_T projection fraction, or the *MPF*. It depends only on the photon and $\not{E}_T$ quantities. In words, the MPF method sums up all the $\vec{E}_T$ outside of the photon and balances this against the photon. Using the relation

$$\vec{\not{E}}_T = -\vec{E}_T^\gamma - \sum{}' \vec{E}_T, \tag{5.11}$$

where the $\sum'$ indicates a sum over the hadronic activity in the calorimeter, the response can be further simplified as

$$j = -\frac{\sum' \vec{E}_T \cdot \hat{n}_\gamma}{E_T^\gamma}.$$

In this form it is more obvious that the MPF method of measuring the response is independent of the underlying event. Since all of the hadronic activity outside of the γ + jet system is approximately ϕ-symmetric, the additional terms in the $\sum'$ sum due to the underlying event cancel out. The MPF is also independent of jet algorithms, because no terms are expressly dependent on jet quantities.

5.3.2 Biases Affecting the MPF Measurement

The measurement of the MPF is susceptible to a number of biases due to detector and physics effects. Radiative corrections to the leading order processes alter the momentum balance at parton level, which biases the MPF measurement low. Poor jet energy resolution, in combination with the steeply falling γ + jet cross-section, biases the MPF high, especially for low energy jets. Both of these biases are described in the following discussion. Biases due to trigger and reconstruction algorithm efficiencies are also expected, but are not discussed here because the parameters in these algorithms have not yet been finalized.

Initial and Final State Radiation

There are higher order diagrams, shown in Figure 5.6, which contribute to the direct photon production cross-section. These diagrams include radiation in the initial (ISR) and final (FSR) state. Each type of radiative process biases the measurement of the MPF in a different way.

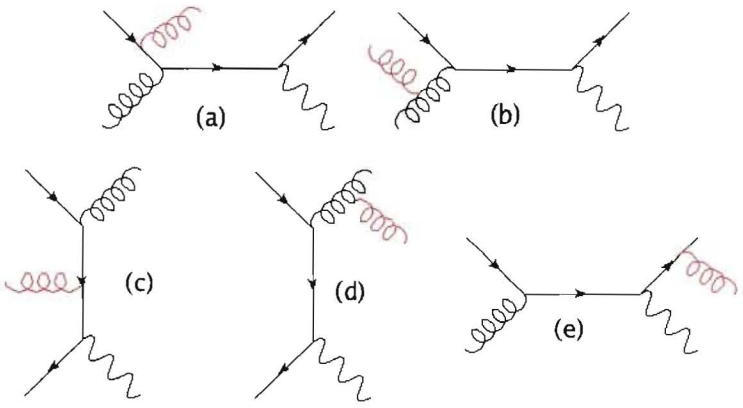

Figure 5.6: Some of the next-to-leading order (NLO) Feynman diagrams for γ + jet events with radiation in the initial (a – c) and final (d,e) state.

Radiation in the initial state has the affect of removing the *a priori* momentum balance of incoming partons. This modifies the outgoing momentum balance in Eq. 5.8 to

$$\vec{E}_T^{\gamma} + \vec{E}_T^{jet} \approx \vec{E}_T^{ISR}, \tag{5.12}$$

where E_T^{ISR} is the transverse energy carried away by the radiated gluon. Radiation in the final state carries momentum away from the final state jet, also modifying the momentum balance in Eq. 5.8.

In either case, both ISR and FSR have the effect of making the γ and jet not back-to-back, i.e., $\Delta\phi < \pi$. This makes it possible to cut out events where ISR or FSR may bias the response measurement, by applying stringent cuts on the angular separation of the photon and jet. This is illustrated in Figure 5.7, where events have been generated in Pythia with ISR/FSR turned off, compared to the case where ISR/FSR are allowed. By demanding that $\Delta\phi > 2.9$, a large fraction of the events with ISR or FSR can be removed from the sample.

Since ISR and FSR bias the response low, the measured momentum balance of the photon and jet is affected by a cut on $\Delta\phi$. This is shown in the fractional p_T balance ρ, defined by

$$\rho = \frac{p_T^{jet} - p_T^{\gamma}}{p_T^{\gamma}}. \tag{5.13}$$

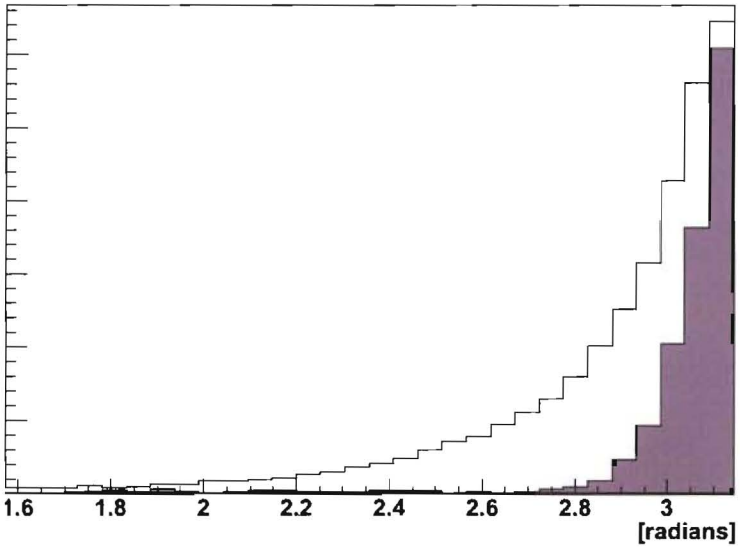

Figure 5.7: $\Delta\phi$ between the leading γ and jet in γ + jet events; (shaded) with ISR/FSR turned off in Pythia using `mstp 61 = 0` and `mstp 71 = 0`; (unshaded) ISR/FSR allowed. Note that these distributions are not normalized.

In Figure 5.8, ρ is shown in various bins of $(p_T^{jet}+p_T^{\gamma})$ before (in red) and after (in blue) applying the $\Delta\phi$ cut between the leading photon and jet. Applying the cut makes the distribution more Gaussian, reduces the RMS, and shifts the mean towards 0, i.e., towards improved balance.

Jet Resolution Bias

Although the jet response is measured using $\not\!\!E_T$, it depends on the jet energy (see Eq. 5.4), because the relative fraction of EM energy in the calorimeter level jet increases with increasing energy. Therefore, the response is measured as a function of measured jet energy. This introduces a bias on the measurement of the MPF, due to the poor jet energy resolution and steeply falling γ + jet cross-section, which is known to vary as $(E_T^{\gamma})^{-5}$ (see Figure 5.4). This bias is best explained with a concrete example[6].

Suppose we have an ensemble of back-to-back γ + jet events at $\eta = 0$ where the γ and parton level jet have a transverse energy of $E_T^{parton} = 50$ GeV. Suppose further

[6]The reasoning in this section is derived from discussions in [10] and [18].

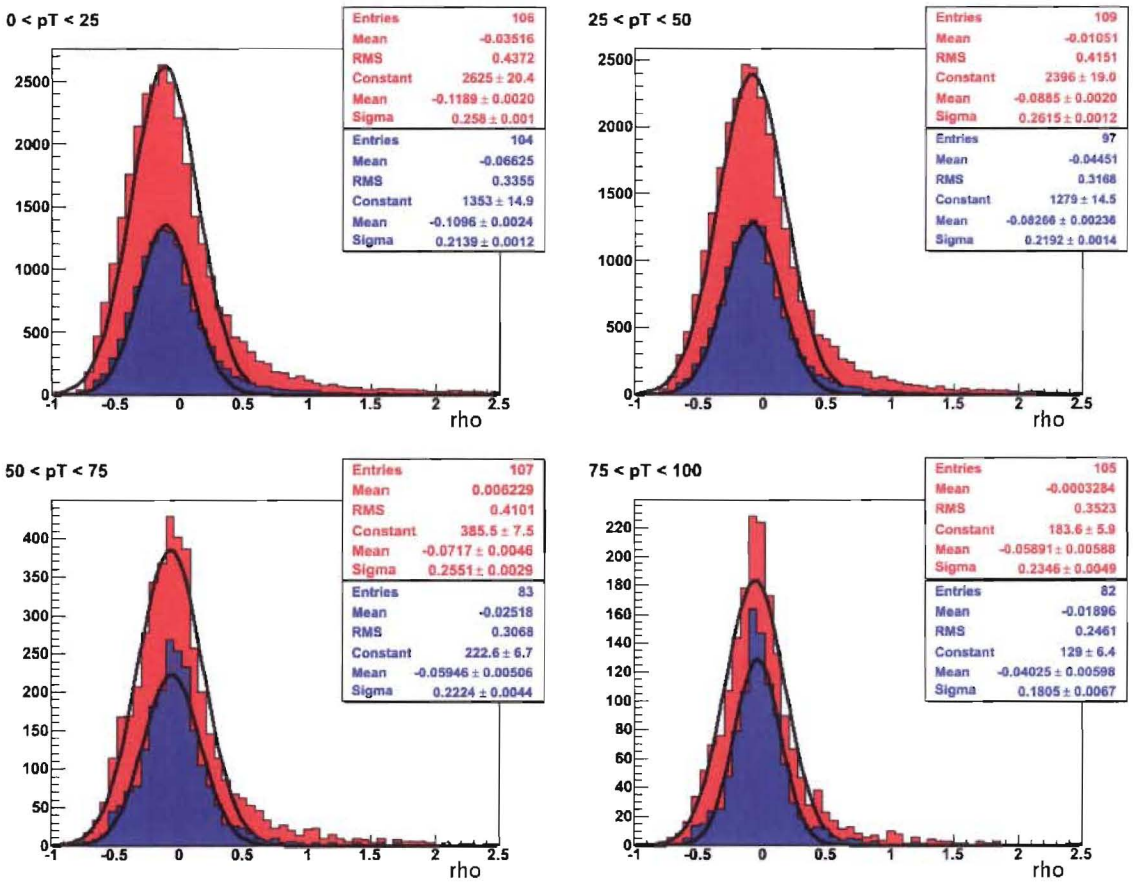

Figure 5.8: The fractional p_T balance, ρ, for events with $\frac{p_T^{jet}+p_T^{\gamma}}{2}$ ranges of 0–25 GeV, 25–50 GeV, 50–75 GeV, and 75–100 GeV. Plotted in red is ρ calculated from all events, and in blue is ρ calculated only from events with $\Delta\phi > 2.9$. Two means are shown for each distribution: the first is the histogram mean, and the second is the parameter of a Gaussian fit.

that the calorimeter has an intrinsic response to these jets of $j = 0.8$ and that the jet energy resolution is 10%, while the photon resolution is 2%. The distributions of measured jet and photon E_T will be as shown in Figure 5.9. The jet energy distribution has a mean of $\langle E_T^{meas,jet} \rangle = j\, E_T^{parton} = 40\,\text{GeV}$ and is considerably broader than the photon E_T distribution. These parameters are summarized in Table 5.2. Note that the measured photon E_T is an accurate measurement of the parton level E_T. In this ensemble, the response is measured correctly in the $E_T^{meas,jet} = 40$ GeV bin as

$$j = \frac{\langle E_T^{meas,jet} \rangle}{\langle E_T^{meas,\gamma} \rangle} = 0.8. \tag{5.14}$$

parameter	value
σ_{jet}	10%
σ_γ	2%
j	0.8
E_T^{parton}	50 GeV
$E_T^{meas,jet}$	40 GeV $\pm$ 5 GeV
$E_T^{meas,\gamma}$	50 $\pm$ 1 GeV

Table 5.2: Parameters for an ensemble of γ + jet events in the $E_T^{parton} = 50$ GeV bin. These distributions neglect the combined effect of the jet resolution and steeply falling cross-section.

However, in reality, we do not have an ensemble of parton level jets with known energies. Instead, we have an ensemble of measured calorimeter level jets. If we consider an ensemble of events binned by measured jet E_T, with no restriction on the parton E_T, we must remember that the cross-section varies as $(E_T^\gamma)^{-5}$. Using Bayes' Theorem, the distribution of parton energies given some measured jet energy is

$$\begin{aligned} p(E_T^{parton}; E_T^{meas,jet}) &\propto p(E_T^{parton}) \cdot p(E_T^{meas,jet}; E_T^{parton}) \\ &\propto (E_T^{parton})^{-5} \cdot \exp\left[\frac{-(E_T^{meas,jet} - 0.8 \cdot E_T^{parton})^2}{50\,\text{GeV}^2}\right]. \end{aligned} \tag{5.15}$$

This implies that low E_T events are much more probable than events in which the γ and jet have high E_T. Because of this, the distribution of parton energies that can give rise to a measured jet energy will be biased low. In other words, it is more probable

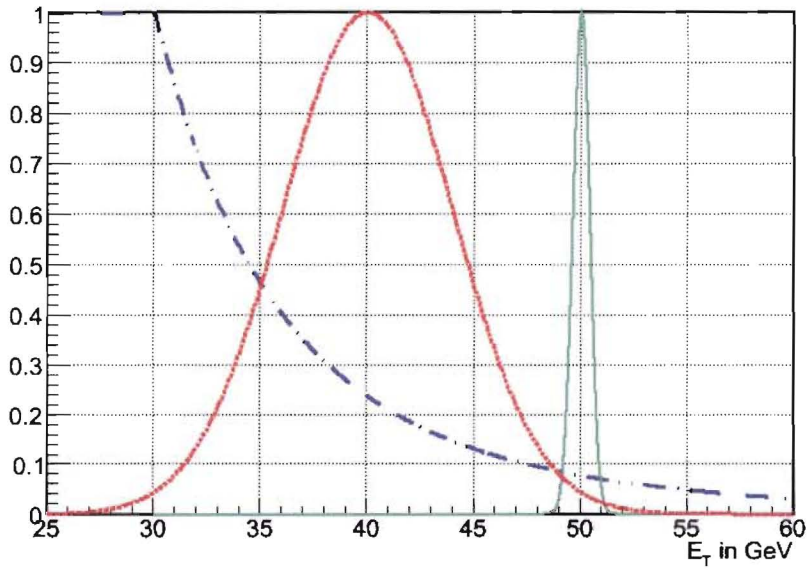

Figure 5.9: The measured γ and jet energy distributions in an ensemble of back-to-back γ + jet events. The green curve is the the photon E_T distribution. The red curve corresponds to the jet E_T distribution. Also shown in blue is the cross-section dependence on E_T (in arbitrary units).

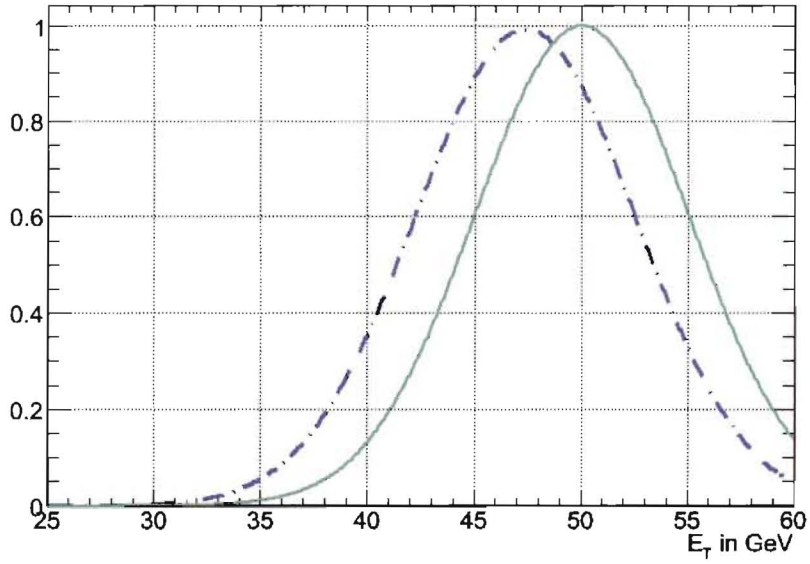

Figure 5.10: The unbiased parton E_T distribution, shown in green, that gives rise to $\langle E_T^{meas,jet} \rangle = 40$ GeV. The dashed blue curve is the parton E_T distribution including the bias introduced by the falling cross section. The mean of the biased distribution is about 5% lower than the unbiased distribution.

for a low E_T parton jet to be measured too high, and thus fall into the $E_T^{meas,jet} = 40$ GeV bin, than for a high E_T parton jet to be measured too low. Therefore, for an ensemble of γ + jet events with $E_T^{meas,jet} = 40$ GeV, the E_T of the photon, which is essentially a measure of the parton jet E_T, is biased low, as shown in Figure 5.10. In this example the bias on the $E_T^{meas,\gamma}$ is about 5%. The parameters defining this ensemble of events are summarized in Table 5.3. The response in these events will be biased as well, and in this case will be measured as

$$j = -\frac{\sum' \vec{E}_T \cdot \hat{n}_\gamma}{E_T^\gamma} = \frac{40\,\text{GeV}}{47.5\,\text{GeV}} = 0.84,$$

or about 5.3% too high. This bias is more prominent at low E_T because the slope of the cross section is steeper, and the resolution on the jet E_T is known to vary as $1/\sqrt{E}$, i.e., it is worse for low energy jets.

In order to get an unbiased measure of the jet energy, the quantity $E' = E_T^\gamma \cdot \cosh(\eta_{jet})$ is used. This quantity is an accurate estimation of the correct

parameter	value
σ_{jet}	10%
σ_{γ}	2%
j	0.8
E_T^{parton}	47.5 GeV $\pm$ 5 GeV
$E_T^{meas,jet}$	40 GeV $\pm$ 5 GeV

Table 5.3: Parameters for an ensemble of γ + jet events in the $E_T^{meas,jet} = 40$ GeV bin. These values take into account the combined effect of the poor jet resolution and steeply falling cross-section.

parton energy since it uses the well-measured photon energy, and it is strongly correlated with the measured jet energy, as shown in Figure 5.11. In order to determine the jet response as a function of jet energy, both the response and jet energy are binned in terms of E'. The mean of the response and jet energy distributions in each E' bin are then plotted against each other. The effect of binning the measured response in terms of this quantity is illustrated in a simulation in Figure 5.12.

5.4 Measurement of the Jet Response

In this section a simulated measurement of the jet response in ATLAS using the MPF method in γ + jet events is presented.

5.4.1 Signal Photon Selection

In order to calculate the response, selection criteria must be defined for identifying the photon in an event. Photons are reconstructed using the e/gamma reconstruction algorithms[7], which identify photon candidates based on discriminating variables from the calorimeters, including lateral and longitudinal shower profiles. The details of these cuts are shown in Table 5.4. Candidates from the e/gamma algorithms are identified as photons if there is no suitable match from the shower in the calorimeter to a track from the inner detector. The distributions of photon p_T and multiplicity

[7]See https://uimon.cern.ch/twiki/bin/view/Atlas/EgammaATLASRecoPerformance for details.

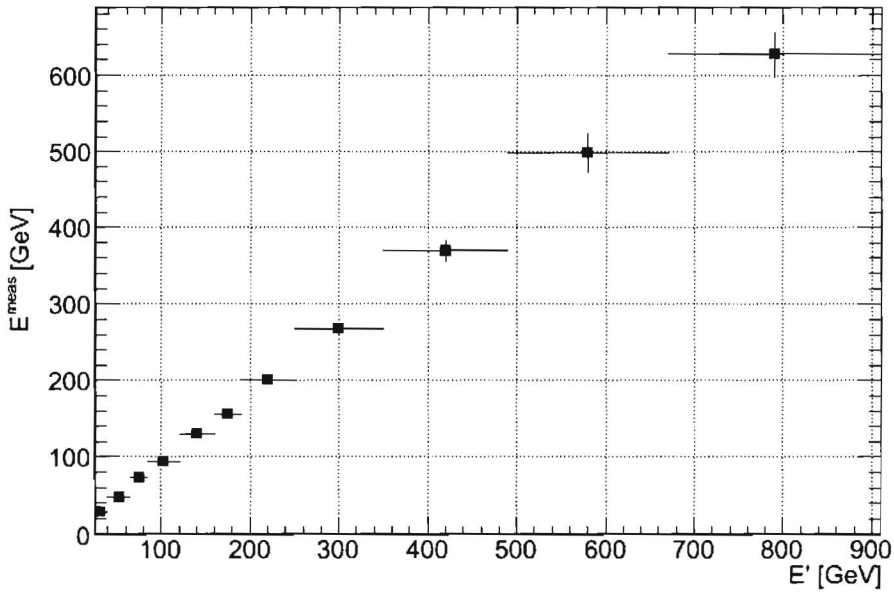

Figure 5.11: The measured jet energy E^{meas} versus the unbiased energy estimator E'.

are shown in Figure 5.13 for the CSC[8] datasets `PhotonJet1 - PhotonJet6`. The p_T ranges for these datasets are summarized in Table 5.5. Using the collection of photons identified by the e/gamma algorithms, further cuts are used to select the signal photon. The leading photon which satisfies the cuts in Table 5.6 is used. If no photon is found that satisfies these cuts, the event is discarded.

5.4.2 Signal Jet Selection

Jets are reconstructed with the seeded cone and k_T algorithms using the parameters in Table 5.7. Since the jet algorithms use signals from the calorimeter, the outputs from the cone and k_T algorithms contain jets reconstructed from hadrons as well as from electrons and photons which have p_T greater than the jet threshold. In order to remove the overlap between the jet collection and photon and electron lists, any jet which is matched to an electron or photon within $\Delta R < 0.2$ is removed from the

[8]CSC stands for Computing System Commissioning, which is an official test of the ATLAS Monte Carlo data production system.

e/gamma cut name	value	description
cluster η-range	$\|\eta\| < 2.47$	the center of the energy cluster is within the tracking volume
hadronic leakage	$E_T^{HAD}/E_T^{EM\ 3\times7} < 4\%$	E_T in the first layer of the hadronic calorimeter is less than 4% of the E_T deposited in the EM calorimeter
middle sampling	$E_T^{3\times7}/E_T^{7\times7} > 0.9$	shower profile is narrow: the E_T in a 3×7 cluster of cells in the middle sampling contains 90% of the E_T in a 7×7 cluster
early shower shape	$N_{peaks} = 1$	cuts on the number of peaks and shower width in the EM calorimeter strips to remove $\pi^0 \rightarrow \gamma\gamma$ from jets

Table 5.4: Details of the cuts on calorimeter variables used to identify photon candidates. For more details, consult the on line reference https://twiki.cern.ch/twiki/bin/view/Atlas/ElectronGamma_IsEM.

dataset	p_T^γ range	cross-section (pb)
`PhotonJet1` (5055)	17 - 35 GeV	$1.63 \cdot 10^5$
`PhotonJet2` (5056)	35 - 70 GeV	$1.64 \cdot 10^4$
`PhotonJet3` (5057)	70 - 140 GeV	$2.12 \cdot 10^3$
`PhotonJet4` (5058)	140 - 280 GeV	$1.87 \cdot 10^2$
`PhotonJet5` (5059)	280 - 560 GeV	11.8
`PhotonJet6` (5052)	560 - 1120 GeV	0.49

Table 5.5: Generated p_T ranges of the photon in γ + jet events for the CSC datasets `PhotonJet1` - `PhotonJet6`. Also shown are the cross-sections for each dataset, measured in pb (picobarns).

selection cut	description
$E_T^{isol}/E_T^\gamma < 0.2$	the E_T in an isolation cone of $\Delta R = 0.2$ surrounding the photon is less than 20% of the photon E_T
$E_T^{isol} < 20$ GeV	the E_T in an isolation cone of $\Delta R = 0.2$ surrounding the photon is less than 25 GeV

Table 5.6: Criteria for selecting signal photons in γ + jet events. These are in addition to the cuts used for defining candidate photons.

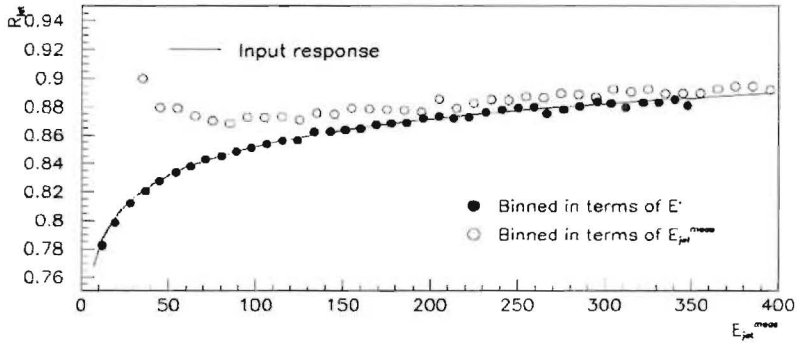

Figure 5.12: Resolution bias in the response measurement using a simulation: through binning the events in terms of E', the input response in the simulation is regained. Binning directly in terms of the measured jet energy results in a clear bias which is more prominent at low energies. This figure is copied from [10].

jet list. The leading jet which satisfies the angular separation cut $\Delta\phi(\gamma, \text{jet}) > 2.9$ is selected as the signal jet. If no jet is found that satisfies the angular separation with the signal photon, the event is discarded. The η and ϕ distributions of signal jets in the CSC datasamples are shown in Figure 5.14.

type	parameter	input	seed p_T	p_T^{jet} threshold	output name
cone	$R = 0.7$	towers	1.0 GeV	7.0 GeV	`ConeTowerJets`
cone	$R = 0.4$	towers	1.0 GeV	7.0 GeV	`Cone4TowerJets`
cone	$R = 0.7$	topo-clusters	1.0 GeV	7.0 GeV	`ConeClusterJets`
k_T	$D = 0.4$	towers	n/a	7.0 GeV	`Kt4TowerJets`

Table 5.7: Parameters used in the jet reconstruction algorithms for this study. See Section 4.1.1 and 4.1.2 for further details on jet algorithms.

5.4.3 $\not\!\!E_T$ Calculation

The $\not\!\!E_T$ quantity is quite simply defined in Eq. 1.1. However, there are a number of different methods which can be used to calculate the sum over the calorimeter cells. For this study, a sum over cells with $|E| > 2\,\sigma(\text{electronics})$ is used. This cut has been found to minimize the contribution of the electronics noise to the resolution of the $\not\!\!E_T$. A correction for energy lost in the dead material, especially in the calorimeter

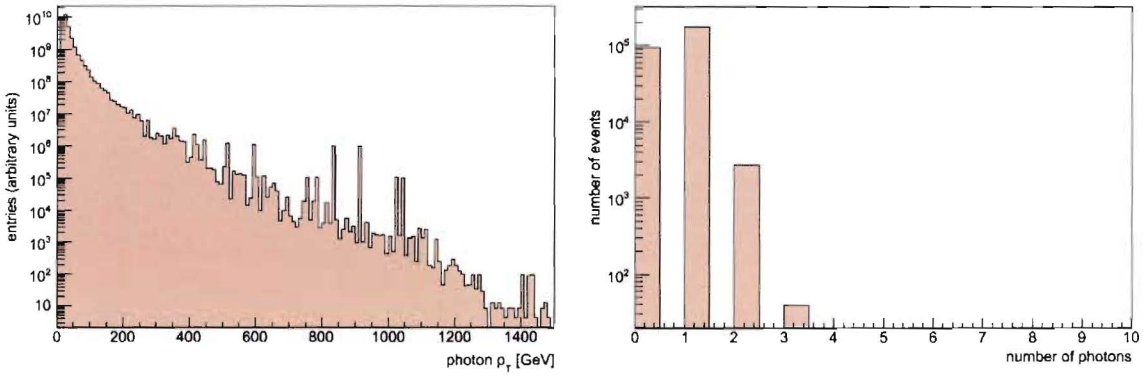

Figure 5.13: Shown are the p_T distribution (left) and photon multiplicity (right) for the CSC datasets `PhotonJet1` - `PhotonJet6`. Only photons which pass the signal selection cuts in Table 5.4 and 5.6 are considered in the plot of the p_T distribution.

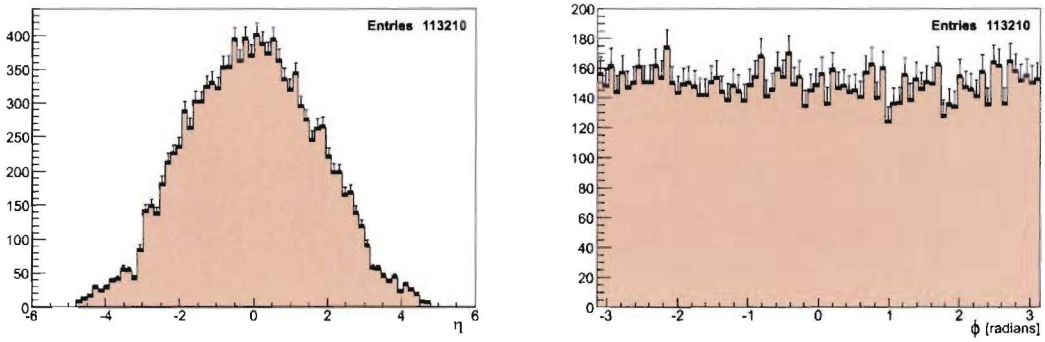

Figure 5.14: η (left) and ϕ (right) distributions for jets in the CSC datasamples which pass the signal selection cuts (see text for more details on the cuts).

cryostat wall, is also applied. This correction is based on the energy deposited by jets in the last layer of the EM barrel calorimeter and the first layer of the TILE. It is defined as

$$\not{E}_T^{corr} = w\sqrt{E_{\text{EM-3}}\,E_{\text{TILE-1}}}, \tag{5.16}$$

where w is a constant fit from Monte Carlo simulations [25].

5.4.4 Analysis Algorithm

As was shown in Section 5.3.2, an unbiased measurement of the energy dependence of the jet response can be performed by binning in E' the events which pass the signal selection criteria described above and then mapping the measured jet response to the measured jet energy in each E' bin. A detailed description of the analysis algorithm is provided below:

1. for each event, retrieve the signal jet and photon using the cuts defined in Sections 5.4.1 and 5.4.2. Calculate the jet response using Eq. 5.10, or veto the event if either a suitable jet or photon is not found.

2. store the jet energy and jet response in an E' bin, using the binning `E' = {25.0 GeV, 40.0 GeV, 65.0 GeV, 85.0 GeV, 120.0 GeV, 160.0 GeV, 190.0 GeV, 250.0 GeV, 350.0 GeV, 490.0 GeV, 670.0 GeV, 910.0 GeV}`.

3. calculate $\langle E^{meas,jet}\rangle$ and $\langle j\rangle$ for each E' bin. The jet response is calculated from a Gaussian fit of the j distribution, iterated over $\pm\sigma$ about the peak, while the jet energy is taken simply as the mean of the $E^{meas,jet}$ distribution.

4. fit $\langle j\rangle$ versus $\langle E^{meas,jet}\rangle$ using either of the theoretical response functions in Eq. 5.4 or Eq. 5.5. The fitted function is used to calibrate the energy of the jets, using Eq. 5.6.

Samples of the jet response and jet energy distributions and fits in each of the E' bins can be found in Appendix B.

jet algorithm	b_0	b_1	b_2
ConeTowerJets	0.751 ± 0.004	0.026 ± 0.005	-0.015 ± 0.004
Cone4TowerJets	0.755 ± 0.003	0.022 ± 0.006	-0.011 ± 0.004
ConeClusterJets	0.740 ± 0.003	0.021 ± 0.005	-0.011 ± 0.004
Kt4TowerJets	0.749 ± 0.004	0.015 ± 0.005	-0.015 ± 0.004

Table 5.8: The fit parameters b_0, b_1, and b_2, and the absolute errors on the fits for the four different jet algorithms. These parameters are used in the logarithmic parameterization of the theoretical response function (Eq. 5.4) shown in Figure 5.15. The scale parameter is $E_{scale} = 200.0$ GeV.

jet algorithm	b_0	b_1	b_2	E_0
ConeTowerJets	0.79 ± 0.025	-0.045 ± 0.012	0.38 ± 0.19	200.0
Cone4TowerJets	0.80 ± 0.017	-0.047 ± 0.013	0.48 ± 0.12	200.0
ConeClusterJets	0.76 ± 0.009	-0.024 ± 0.012	0.09 ± 0.15	200.0
Kt4TowerJets	0.77 ± 0.017	-0.020 ± 0.015	0.22 ± 0.22	200.0

Table 5.9: Shown are the fit parameters b_0, b_1, b_2, and E_0, and the absolute errors on the fits for the four different jet algorithms. These parameters are used in the power law parameterization of the theoretical response function (Eq. 5.5) shown in Figure 5.15.

5.4.5 Jet Response for Cone and k_T Jets

We applied the procedure for measuring the jet response in γ + jet events described in the previous sections to the CSC datasamples. The jet response was measured as a function of jet energy for the four types of jets ConeTowerJets, Cone4TowerJets, ConeClusterJets, and Kt4TowerJets. The results of the measurement are shown in Figure 5.15 and Tables 5.8 and 5.9. Details of the jet response and jet energy distributions and fits in each of the E' bins are shown in Appendix B.

Since the MPF is independent of jet quantities, we expect that the energy dependence of the response should not be strongly dependent on the type of jet algorithm used to define the jet in the measurement, although the different algorithms may result in different $\langle E_T^{meas,jet} \rangle$ for a given E' bin, which can shift the response slightly. This is shown in Table 5.8, where the constants b_0, b_1, and b_2 of Eq. 5.4 are shown to vary only slightly among the four types of jets used in this study. Most of the variations in

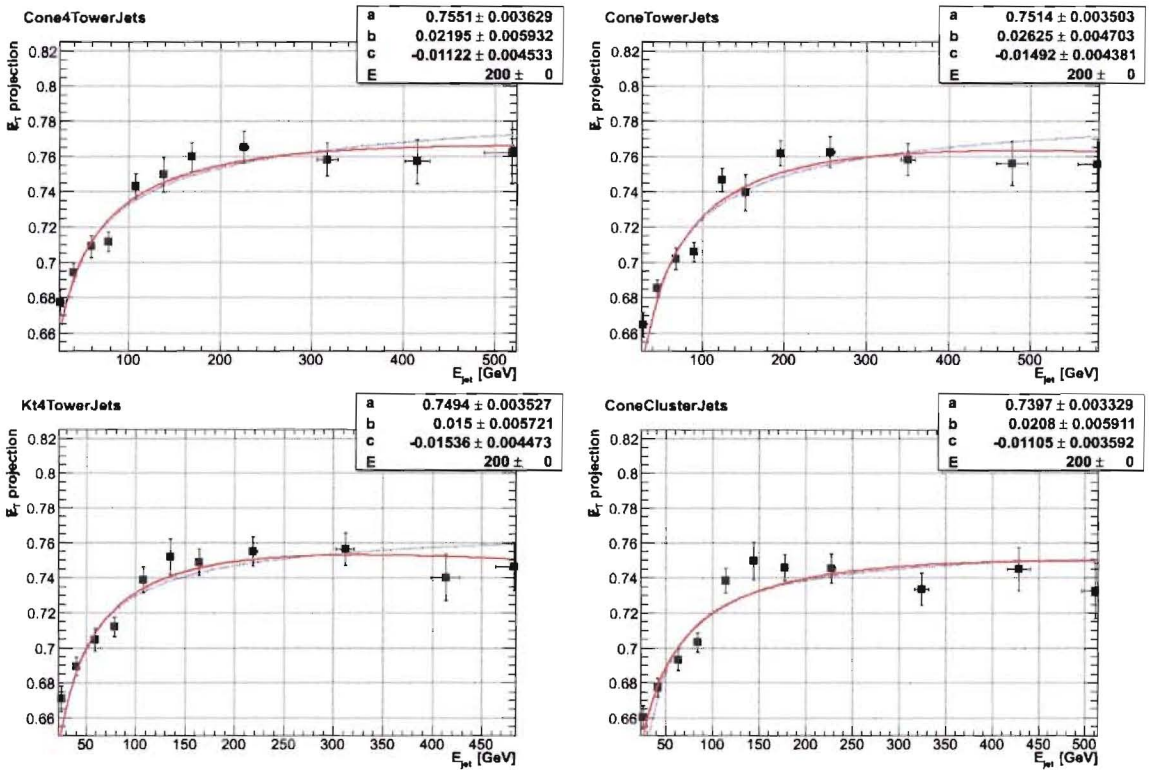

Figure 5.15: Plots showing the energy dependence of the jet response for `Cone4TowerJets` (top left), `ConeTowerJets` (top right), `Kt4TowerJets` (bottom left), and `ConeClusterJets` (bottom right). The points are given by the fits for the jet response and jet energy in each of the E' bins (the lowest E' bin is excluded in the fits and is not shown in these plots). The solid line corresponds to the fit using the logarithmic parameterization (Eq. 5.4) with the parameters in Table 5.8. The dashed line corresponds to the fit with the power law parameterization (Eq. 5.5) with the parameters in Table 5.9.

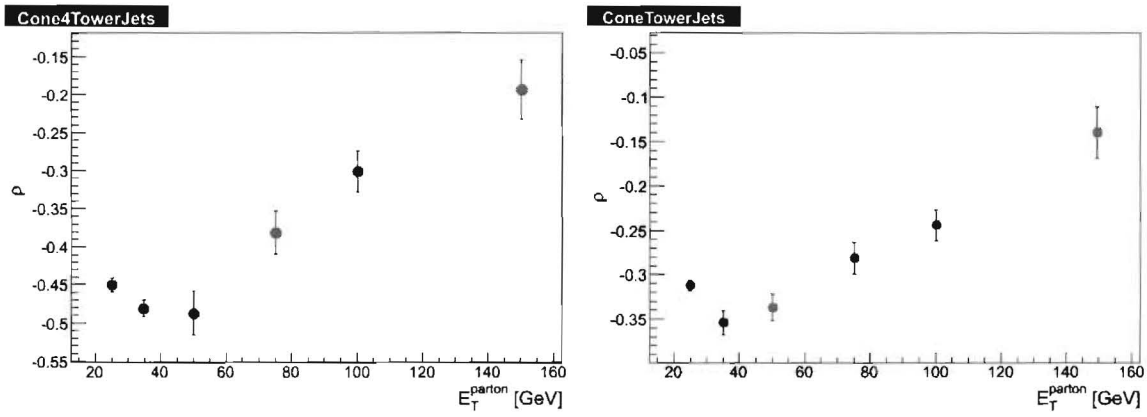

Figure 5.16: The fractional p_T balance, ρ, versus the parton level E_T for `Cone4TowerJets` (left) and `ConeTowerJets` (right). The parameter ρ is defined in Eq. 5.13. Notice the large variation in the range of ρ for the two different jet types.

the parameters are well within the errors in the fit. The ability to measure the jet response separately from jet algorithm effects is important in factoring the components of the jet energy scale. As shown in Figure 5.16, using a direct p_T balance approach between the γ and the jet makes it impossible to measure the jet response correction independently of jet algorithm. Even between the similar clustering algorithms in these calculations (the only difference being in the R parameter) the difference in ρ at low E_T^{parton} is greater than 15%. The parameter ρ for `Cone4TowerJets` is ≈ -0.5 and for `ConeTowerJets` it is ≈ -0.35. This means that ρ depends strongly on the details of the clustering algorithm.

The jet response is known to vary with η because of cracks in the calorimeter, dead material, and different calorimeter technologies in the barrel, endcap and forward regions of the detector. This is shown clearly in Figure 5.17, where the barrel region $|\eta| < 1.5$, the endcap region $1.5 < |\eta| < 3.2$ and the forward region $|\eta| > 3.2$ are clearly visible. The transition regions contain cracks and dead material such as cabling and LAr services. These regions correspond to the dips in the jet response. However, it is expected that the jet response is constant in ϕ, which is an important consideration for calculating $\not\!\!E_T$. This is shown in Figure 5.18.

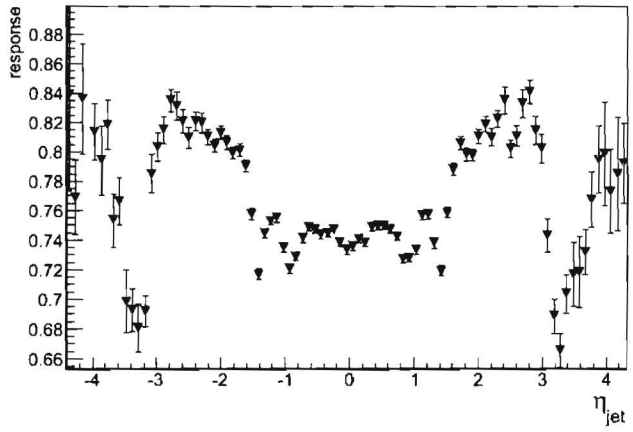

Figure 5.17: The jet response, calculated using the MPF method, versus η_{jet}. The dips correspond to known crack and dead material regions. The three main calorimeter subsystems are clearly visible as η regimes.

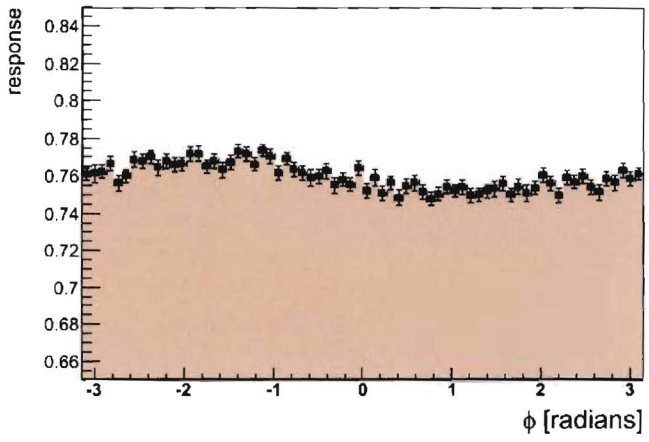

Figure 5.18: The jet response, calculated with the MPF method, versus ϕ_{jet}. The response is constant to within $< 1\%$ over the entire range.

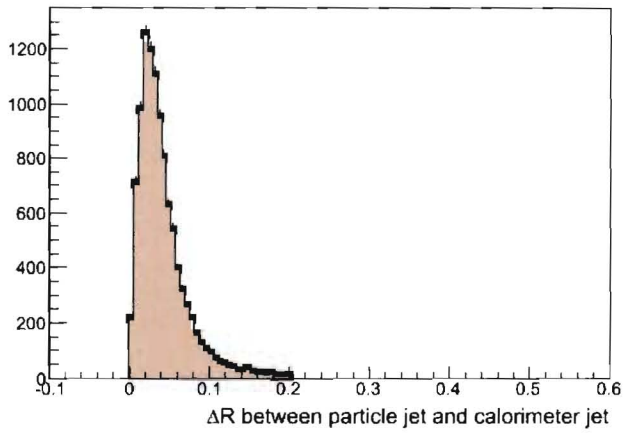

Figure 5.19: ΔR between the true particle level jet and the signal jet. Signal jets which are not matched to a particle level jet within $\Delta R < 0.2$ are not considered.

The quality of the jet response calibration using the MPF method can be cross-checked in the Monte Carlo data by comparing the corrected calorimeter level jet energy to the true particle level jet energy. The particle level jets are defined in the Monte Carlo by applying the various jet algorithms to the hadrons that are the outputs from the event generation step (see Figures 3.11 and 4.1). Calorimeter level jets are then matched to the particle level jets using a nearest neighbour match, requiring that $\Delta R < 0.2$. Figure 5.19 shows the distribution of ΔR in matching calorimeter level jets to particle level jets. If the ratio of the particle level jet energy ($E_T^{true,jet}$) to the corrected calorimeter level jet energy ($E_T^{calib,jet}$, see Eq. 5.6) is flat, then the jet response calibration has been applied correctly. Note that it is not expected that this ratio be unity, since biases due to the underlying event and showering will affect the overall jet calibration differently for the various jet algorithms.

In order to perform this cross check, the ratios $r_{calib} \equiv E_T^{true,jet}/E_T^{calib,jet}$ and $r_{meas} \equiv E_T^{true,jet}/E_T^{meas,jet}$ were calculated for all jets in the CSC datasets using the logarithmic parameterization of the jet response, and then binned in $E_T^{true,jet}$. The mean of a Gaussian fit, iterated over $\pm\sigma$ about the peak, is plotted versus the particle level jet energy for both quantities in Figure 5.20. The good linearity of the ratio r_{calib} shows the consistency of the jet response calibration using the MPF method (compare

this to the ratio for the uncalibrated jets in the same plots). The response correction results in linearity within 2-3% over the entire energy range 50 - 900 GeV.

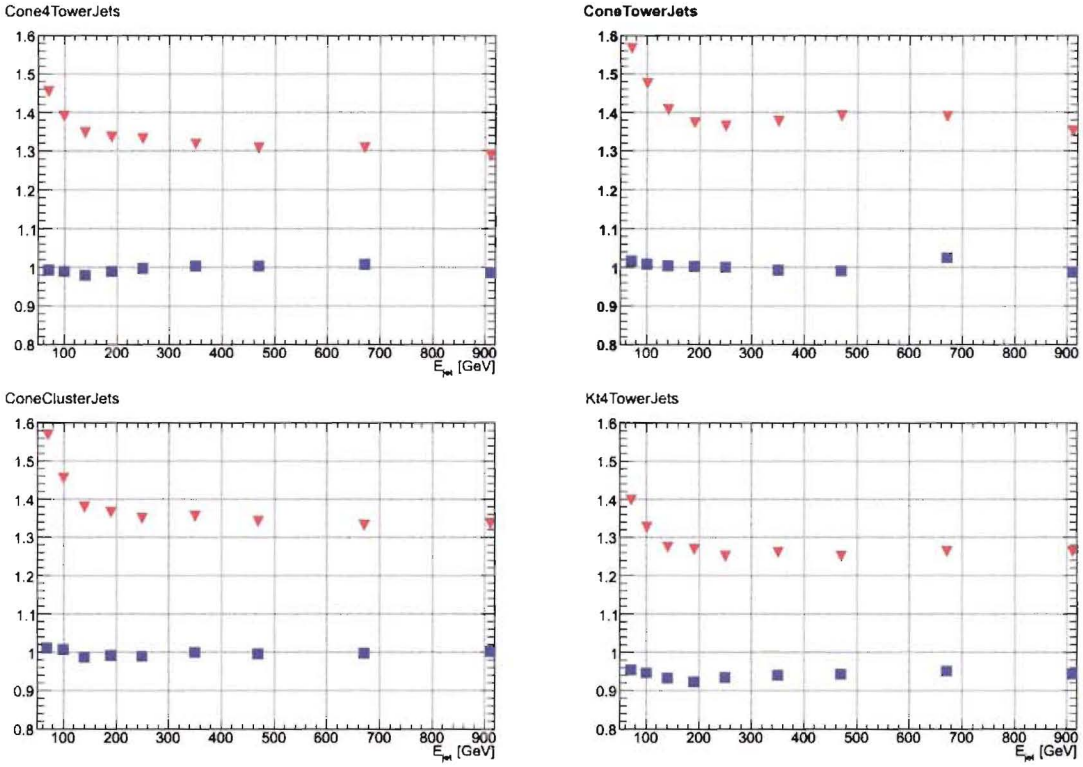

Figure 5.20: Plots showing the ratios r_{calib} (squares) and r_{meas} (triangles) for `Cone4TowerJets` (top left), `ConeTowerJets` (top right), `ConeClusterJets` (bottom left), and `Kt4TowerJets` (bottom right). The points in each bin are given by the mean of a Gaussian fit for the ratio r_{calib} or r_{meas}, and the particle level jet energy. This calibration is done using the logarithmic parameterization of the jet response.

5.5 Dijet Background

The main background to γ + jet events is from dijet events in which one of the jets fluctuates into a highly electromagnetic jet (eg., a high π^0 content at particle level) and is wrongly identified as a photon. Although the occurrence of such fluctuations is rare, the dijet cross section is so large that even with a very low relative rate of "fake-photon" dijet events, the background to γ + jet events is significant.

dataset name	p_T range	number of events	cross section (pb)
J1	17 - 35 GeV	150 K	$1.38\ 10^9$
J2	35 - 70 GeV	150 K	$9.33\ 10^7$
J3	70 - 140 GeV	150 K	$5.88\ 10^6$
J4	140 - 280 GeV	150 K	$3.08\ 10^5$
J5	280 - 560 GeV	150 K	$1.25\ 10^4$

Table 5.10: The p_T ranges and cross sections for the dijet datasets used in this study. Notice that the cross section varies over five orders of magnitude between the J1 and J5 datasets.

dataset	number of signal events	number of events
J1	709	150 K
J2	2555	150 K
J3	2659	150 K
J4	2767	150 K
J5	2794	150 K

Table 5.11: The number of "fake photon" dijet events for each of the dijet datasets. Notice that the rate increases with increasing p_T.

In order to estimate the background, we applied the signal photon and jet selection criteria to dijet events from the CSC datasets J1 - J5. These datasets were produced entirely using the Athena release 11.0.42. The p_T ranges and cross sections for these datasets are summarized in Table 5.10. Note that the extremely high rates of low-p_T dijet events (J1 & J2) are not representative of ATLAS running conditions because the Monte Carlo simulation did not take the ATLAS trigger system into account. In real ATLAS running, the event triggers will reject the vast majority of low-p_T dijet events.

The number of dijet events containing a reconstructed photon and jet which passed the signal selection cuts is shown in Table 5.11 for the datasets J1 - J5. Note that for technical reasons, the EM-scale jet and $\not\!\!E_T$ quantities were not available in the dijet datasets. Therefore a quantitative study on how the dijet events bias the response calculation could not be performed. Further studies are anticipated when a revised dataset becomes available.

5.6 Underlying Event

One part of the total jet energy scale correction is a correction for the underlying event energy. This correction is simplest for cone algorithms because of their more regular shape. Using the truth tools available in the Athena framework, particles coming from the γ + jet signal process can be filtered out from the particles coming from any additional interactions in the event. Jets are constructed from these filtered hadrons using the cone jet algorithms. The same algorithms are applied to the default truth particle collection, which also contains particles from the underlying event and any additional processes in the event. By matching and comparing the jets at particle level we are able to derive an estimation for the level of underlying event activity in cone jets. This is summarized in Table 5.12 and Figure 5.21.

R parameter	UE energy (GeV)	Error (GeV)
0.4	1.45	0.015
0.7	3.17	0.022

Table 5.12: Estimated levels of underlying event activity in cone jets with $R = 0.4$ and $R = 0.7$. Calculated from the average of the distributions in Figure 5.21.

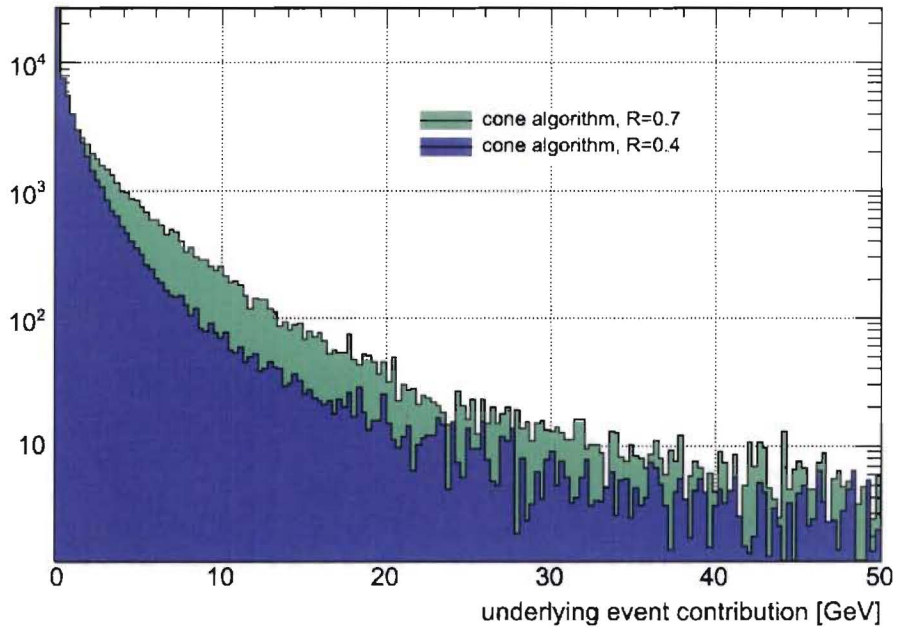

Figure 5.21: Distributions of energy from underlying event at particle level in cone jets with $R = 0.4$ and $R = 0.7$.

Chapter 6

Pileup

The LHC is designed to collide bunches of protons every 25 ns at each of the interaction regions for the four experiments[1]. Because of the high design luminosity, there is a Poisson mean of 23 collisions on top of any signal processes that occur at each bunch crossing in ATLAS. Hence, there are signals from many proton-proton collisions at any time in the detector. These additional collisions are so-called minimum bias collisions, which are low E_T parton scattering events. The overall pileup effect is further exacerbated by the fact that the detector response is up to 500ns long in the liquid argon calorimeters. In the following discussion, the general term *pileup* refers to the additional minimum bias collisions 'piled up' in each bunch crossing, called *event pileup*, as well as the out-of-time pileup signals from previous bunch crossings (signals which take $t > 25$ ns to propagate), which is called *detector pileup*.

In Section 6.1 a model for event pileup is presented. This model is used to show that pileup distributions are strongly correlated. Detector pileup is presented in Section 6.2. A possible technique for supressing pileup noise is analyzed in Section 6.4, and is shown to introduce a bias on the mean energy. This is followed in Section 6.5 by a discussion of the physics signals from pileup that will have an effect on in situ calibration using γ + jet events.

[1]It should be mentioned that the bunch structure is more complicated because of the addition of abort gaps in the LHC and the SPS. These are empty bunches that are necessary because of the time needed to dump the beam.

6.1 Event Pileup

In the minimum bias collisions there is structure to the events. This is because particle showers spread across multiple calorimeter cells, jets from the minimum bias collisions are localized in space, and there is a global structure to the events due to purely statistical effects [26]. In studying these effects of spatial pileup correlations, it is assumed that across bunch crossings there are no correlations, so that only event pileup is considered. To get a handle on the global structure, we use the model presented in the work of Chollet in [27]. This model is purely statistical and neglects to consider physical effects such as showering or jet structures. The model assumes that the number of proton-proton collisions in each bunch crossing follows a Poisson distribution with mean N_{mb}

$$P_{N_{mb}}(n) = \frac{(N_{mb})^n}{n!} \cdot e^{-N_{mb}}. \tag{6.1}$$

For each collision, a possible m particles are generated from a Poisson distribution with mean N_p

$$P_{N_p}(m) = \frac{(N_p)^m}{m!} \cdot e^{-N_p}. \tag{6.2}$$

6.1.1 Event Pileup Distribution

Number of Generated Particles

The probability to generate N total charged and neutral particles is ρ_N. It is given by

$$\begin{aligned} \rho_N &= \sum_{n=0}^{\infty} P_{N_{mb}}(n) \cdot \sum_{m_1=0}^{\infty} \cdot \sum_{m_2=0}^{\infty} \cdots \sum_{m_n=0}^{\infty} P_{N_p}(m_1) \cdot P_{N_p}(m_2) \cdots \\ &\quad P_{N_p}(m_n) \cdot \delta(m_1 + m_2 + \cdots + m_n - N) \\ &= \sum_{n=0}^{\infty} P_{N_{mb}}(n)\, p(N|n) \end{aligned} \tag{6.3}$$

This is a sum over all possible numbers of minimum bias collisions n, weighted by the probabilities $p(N|n)$ to get N particles from n collisions. To simplify this expression,

consider that any of the N particles may be generated in collision i with probability p_i $(i = 1, 2, \cdots n)$ such that

$$\sum_{i=1}^{n} p_i = 1. \tag{6.4}$$

If m_i is the number of particles generated by collision i, then the probability distribution for the variables m_i is the multinomial distribution

$$f(m_1, m_2, \cdots, m_n) = \frac{N!}{\prod_{i=1}^{n} m_i!} \cdot \prod_{i=1}^{n} p_i^{m_i}, \tag{6.5}$$

where $m_i \epsilon [0, N]$ and $\sum_{i=1}^{n} m_i = N$. A particle is equally likely to be generated in any of the minimum bias collisions, so that

$$\prod_{i=1}^{n} p_i^{m_i} = \left(\frac{1}{n}\right)^{\sum_{i=1}^{n} m_i} = \frac{1}{n^N}. \tag{6.6}$$

The sum of the probabilities for all possible arrangements for m_i is unity, i.e.,

$$\sum_{m_1=0}^{\infty} \cdot \sum_{m_2=0}^{\infty} \cdots \sum_{m_n=0}^{\infty} f(m_1, m_2, \cdots, m_n)\delta(m_1 + m_2 + \cdots + m_n - N) = 1. \tag{6.7}$$

To continue, rearrange Eq. 6.3 using the definition 6.2:

$$\begin{aligned} p(N|n) &= \sum_{m_1=0}^{\infty} \cdot \sum_{m_2=0}^{\infty} \cdots \sum_{m_n=0}^{\infty} P_{N_p}(m_1) \cdot P_{N_p}(m_2) \cdots P_{N_p}(m_n) \cdot \delta(m_1 + \cdots + m_n - N) \\ &= \sum_{m_1=0}^{\infty} \cdot \sum_{m_2=0}^{\infty} \cdots \sum_{m_n=0}^{\infty} \frac{(N_p)^{m_1+m_2+\cdots+m_n}}{\prod_{i=1}^{n} m_i!} e^{-n \cdot N_p} \delta(m_1 + \cdots + m_n - N). \end{aligned}$$

This is simplified by using Eq. 6.5 and Eq. 6.6 to get the relation

$$\frac{(N_p)^{m_1+m_2+\cdots+m_n}}{\prod_{i=1}^{n} m_i!} = \frac{(n \cdot N_p)^N}{N!} f(m_1, m_2, \cdots, m_n) \tag{6.8}$$

so that

$$\begin{aligned} p(N|n) &= \sum_{m_1=0}^{\infty} \cdots \sum_{m_n=0}^{\infty} P_{N_p}(m_1) \cdot P_{N_p}(m_2) \cdots P_{N_p}(m_n) \cdot \delta(m_1 + \cdots + m_n - N) \\ &= e^{-n \cdot N_p} \frac{(n \cdot N_p)^N}{N!} \underbrace{\sum_{m_1=0}^{\infty} \cdots \sum_{m_n=0}^{\infty} f(m_1, m_2, \cdots, m_n)\delta(m_1 + \cdots + m_n - N)}_{=1 \text{ by } (6.7)} \\ &= e^{-n \cdot N_p} \frac{(n \cdot N_p)^N}{N!}. \end{aligned} \tag{6.9}$$

This is seen to be a Poisson distribution with a mean of $(n \cdot N_p)$, which is the number of collisions multiplied by the mean number of particles per collision. Finally then, the probability to generate N particles is

$$\rho_N = \sum_{n=0}^{\infty} P_{N_{mb}}(n) \cdot e^{-n \cdot N_p} \frac{(n \cdot N_p)^N}{N!} \tag{6.10}$$

which is not a Poisson distribution. The mean number of particles is just the mean number of collisions multiplied by the mean number of particles generated by each collision [27]

$$\langle N \rangle = N_{mb} N_p. \tag{6.11}$$

Variance Calculation

The variance on the number of generated particles is calculated as

$$\begin{aligned}
\sigma^2(N) &= \sum_{N=0}^{\infty} N^2 \rho_N - \langle N \rangle^2 \\
&= \sum_{N=0}^{\infty} N(N-1)\rho_N + \sum_{N=0}^{\infty} N \rho_N - (N_{mb}N_p)^2 \\
&= \sum_{N=0}^{\infty} \left[\sum_{n=0}^{\infty} P_{N_{mb}}(n) \cdot N(N-1) \cdot e^{-n \cdot N_p} \frac{(n \cdot N_p)^N}{N!} \right] + \langle N \rangle - (N_{mb}N_p)^2 \\
&= \sum_{n=0}^{\infty} \left[P_{N_{mb}}(n) \left(\sum_{N=0}^{\infty} \cdot N(N-1) \cdot e^{-n \cdot N_p} \frac{(n \cdot N_p)^N}{N!} \right) \right] + N_{mb}N_p - (N_{mb}N_p)^2
\end{aligned}$$

where the exponential term can be rewritten as

$$\frac{1}{e^x} = \frac{1}{\sum_{N=2}^{\infty} \frac{x^{N-2}}{(N-2)!}}$$

so that

$$\begin{aligned}
\sigma^2(N) &= \sum_{n=0}^{\infty} P_{N_{mb}}(n) \, (n \cdot N_p)^2 \cdot \underbrace{\sum_{N=2}^{\infty} \left(\frac{(n \cdot N_p)^{N-2}}{(N-2)!} e^{-n \cdot N_p} \right)}_{=1} + N_{mb}N_p - (N_{mb}N_p)^2 \\
&= N_p^2 \left(\sum_{n=0}^{\infty} n^2 P_{N_{mb}}(n) \right) + N_{mb}N_p - (N_{mb}N_p)^2
\end{aligned}$$

$$
\begin{aligned}
&= N_p^2\langle n^2\rangle + N_{mb}N_p - (N_{mb}N_p)^2 \\
&= N_p^2\left(\sigma^2(n) + \langle n\rangle^2\right) + N_{mb}N_p - (N_{mb}N_p)^2 \\
&= N_p^2\left(N_{mb} + N_{mb}^2\right) + N_{mb}N_p - (N_{mb}N_p)^2 \\
&= N_{mb}\left(N_p^2 + N_p\right) \qquad (6.12)
\end{aligned}
$$

Number of Detected Particles

To calculate the pileup distributions in a real detector, only detected particles need be considered. This is different from the distribution of generated particles in the minimum bias collisions because

- there is a cutoff on low energy particles due to the magnetic field - particles with low E_T are curled away before reaching the calorimeter
- the detection surface $\neq$ generation surface - there are gaps in ϕ and η as well as inactive material in front of the detectors. Also, one is often only interested in the pileup distribution in some localized region of the detector.

The first effect can be dealt with by introducing an efficiency ϵ for the relative number of particles above the energy threshold. This will come from Monte Carlo simulations of the p_T distributions of charged particles from minimum bias collisions. The second effect is more complicated. Supposing that the particles are generated approximately uniformly in (η, ϕ)[2], the probability to reach some region of the detection surface for each particle is $\alpha \equiv$ detection/generation surface ratio. The probability to get K particles in the detection area out of N in total is a binomial distribution

$$\Lambda_N(K) = \frac{N!}{(N-K)!\,K!}\alpha^K(1-\alpha)^{N-K}. \qquad (6.13)$$

The mean $\langle N\rangle$ is modified by the factor α

$$\langle K\rangle = \alpha\,\langle N\rangle \qquad (6.14)$$

[2]This is a valid approximation, cf Figure 1.5.

Variance Calculation

The variance of particles incident in some region of the detector is

$$\sigma^2(K) = \sum_{K=0}^{\infty} K^2 \Omega_N(K) - \langle K \rangle^2 \tag{6.15}$$

where $\Omega_N(K)$ is defined as the probability to detect K particles

$$\Omega_N(K) = \sum_{N=0}^{\infty} \rho_N \Lambda_N(K) \tag{6.16}$$

so that the variance is [27]

$$\begin{aligned}
\sigma^2 &= \sum_{K=0}^{\infty} K(K-1)\Omega_N(K) + \sum_{K=0}^{\infty} K\Omega_N(K) - \langle K \rangle^2 \\
&= \sum_{N=0}^{\infty} \rho_N \sum_{K=0}^{\infty} K(K-1) \frac{N!}{(N-K)!\,K!} \alpha^K (1-\alpha)^{N-K} + \langle K \rangle - \langle K \rangle^2 \\
&= \sum_{N=0}^{\infty} \rho_N N(N-1) \cdot \sum_{K=0}^{\infty} K(K-1) \frac{(N-2)!}{(N-K)!\,K!} \alpha^K (1-\alpha)^{N-K} + \langle K \rangle - \langle K \rangle^2 \\
&= \sum_{N=0}^{\infty} \rho_N N(N-1) \cdot \sum_{K=0}^{\infty} \frac{(N-2)!}{(N-K)!\,(K-2)!} \alpha^K (1-\alpha)^{N-K} + \langle K \rangle - \langle K \rangle^2 \\
&= \sum_{N=0}^{\infty} \rho_N N(N-1) \cdot \alpha^2 \underbrace{\sum_{K=2}^{\infty} \frac{(N-2)!}{(N-K)!\,(K-2)!} \alpha^{K-2} (1-\alpha)^{N-K}}_{=\sum_K \Lambda_N(K)=1} + \langle K \rangle - \langle K \rangle^2 \\
&= \alpha^2 \left(\left\langle N^2 \right\rangle - \langle N \rangle - \langle N \rangle^2 \right) + \alpha \langle N \rangle \\
&= \alpha^2 \left(\sigma^2(N) - \langle N \rangle \right) + \alpha \langle N \rangle .
\end{aligned} \tag{6.17}$$

With the results from Eq. 6.11 and 6.12, $\sigma^2(N)$ and $\langle N \rangle$ can be substituted to give the final result

$$\sigma^2(K) = \alpha \cdot (N_p\, N_{mb})(1 + \alpha\, N_p) . \tag{6.18}$$

Equation 6.18 is an expression for the variance of number of particles, K, which are incident on some surface region of the detector, parametrized by α.

Energy Deposition

It is clear that $\sigma(K)$ grows faster than $\sqrt{\alpha}$, i.e. faster than $\sqrt{\text{surface}}$. Therefore, it can be seen that the extra α term in Eq. 6.18 implies a positive lateral correlation

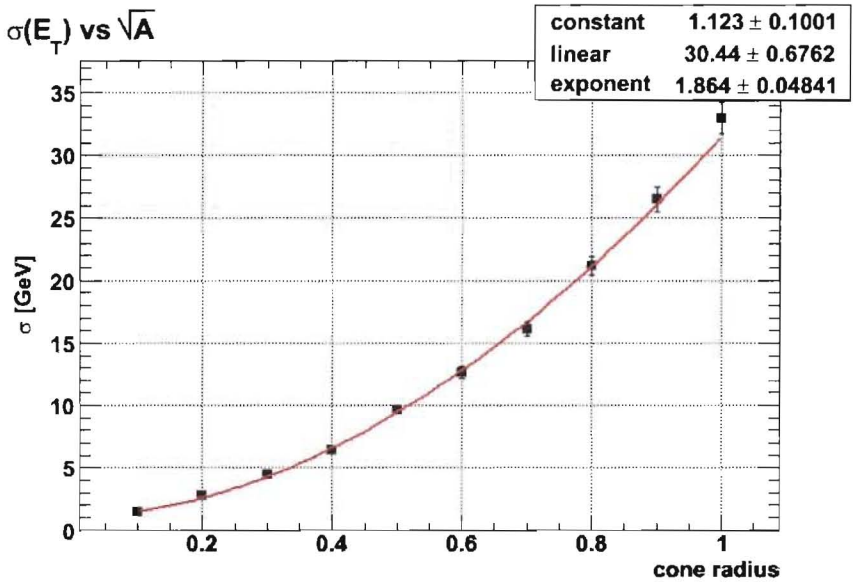

Figure 6.1: Transverse energy RMS versus the square root of detection area ($= \Delta R$) for the barrel region $(\eta, \phi) = (1.5, 0.5)$ of the calorimeter. This figure uses minimum bias collisions fully simulated in Geant4 @ low-luminosity (1/5 design luminosity). The curve is fitted to the form $a + b \cdot (\Delta R)^c$

to the pileup energy distribution [26]. It is easiest to explain by assuming a normal pileup distribution with E_T RMS σ_i in all cells. If the cells are uncorrelated, then the total RMS is given as

$$\sigma_T = \sqrt{\sum_i \sigma_i^2} = \sqrt{Q\sigma_i^2} \tag{6.19}$$

where Q is the total number of cells considered. Neglecting granularity effects for very small surfaces, $Q \propto \alpha$ so that for uncorrelated pileup signals,

$$\sigma_T \propto \sqrt{\alpha}. \tag{6.20}$$

However, if the pileup signals are correlated, Eq. 6.19 is modified

$$\sigma_T = \sqrt{\sum_i \sigma_i^2 + cov\,(\sigma_i, \sigma_j)} \tag{6.21}$$

in which $cov\,(\sigma_i, \sigma_j)$ can be identified here with the $\alpha^2 N_p^2 \cdot N_{mb}$ term in Eq. 6.18. Figure 6.1 shows that σ scales with $\sqrt{\text{area}}^{1.9}$, indicating a strong lateral correlation.

Distributions of the RMS versus $\sqrt{\text{area}}$ for the various calorimeter subsystems are shown in Appendix A.

6.2 Detector Pileup

In the liquid argon calorimeters the drift time for signals across the argon gap is $\geq$ 400ns. This means that signals from more than 20 bunch crossings are superimposed. In order to limit the effects of detector pileup, and to yield a fast response for energy measurements in calorimeter cells, a fast shaped pulse is derived from the drift current signal. A bipolar pulse is used that yields a peak proportional to the peak drift current (and thus to the shower energy) in about 40ns. A plot of the bipolar response is shown in Figure 6.2. The choice of electronics shaping was made to optimize the sum

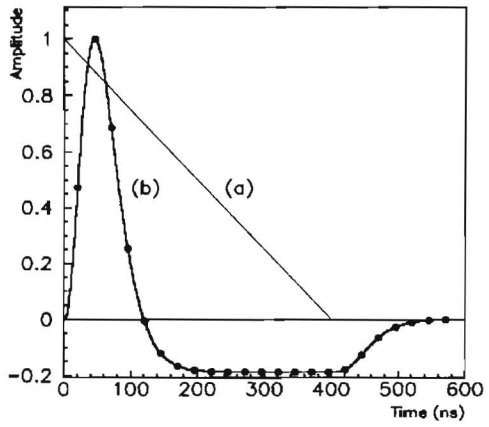

Figure 6.2: Drift current versus time corresponding to the input signal (a), and response of the bipolar shaper (b). The black dots indicate the beam crossings [28].

of electronics noise (such as time jitter, which increases with faster shaping) and the detector pileup noise due to signal processing (which increases with slower shaping). In fact, pileup noise is not a true noise source, since it is not purely random [29]. However, in ATLAS where the number of collisions is so high, there is an essentially continuous background which can be treated as a noise source assuming, as above, that there are no correlations between bunch crossings. In a single calorimeter cell

there is an energy deposition E_j from event pileup in each bunch crossing j. There is also energy deposition from high-p_T physics processes, but these are so rare compared to the contribution from event pileup that they are ignored for this discussion. The readout signal for a single bunch crossing is then

$$S = \sum_j E_j g(t_j), \tag{6.22}$$

where $g(t_j)$ is the pulse shape sampled at time t_j, so that the mean signal is given by

$$\begin{aligned} \langle S \rangle &= \sum_j \langle E_j \rangle g(t_j) \\ &= \langle E \rangle \sum_j g(t_j). \end{aligned} \tag{6.23}$$

However, because the positive and negative areas of the signal shape balance each other,

$$\sum_j g(t_j) = 0 \tag{6.24}$$

and so $\langle S \rangle = 0$. On average then, the measured signal should have no positive offset due to the additional minimum bias collisions in each crossing. This is shown in Figure 6.3 where the total E_T in the ATLAS calorimeters has been summed in a minimum bias event with pileup corresponding to 4/5 design luminosity. The total E_T in the entire calorimeter is < 15 GeV.

However, on an event-by-event basis, there will be large fluctuations due to variances in the number of minimum bias collisions and in the number of particles (and hence in the deposited energy), as described above. The variance in the measured signal is derived in [29], and is shown to be

$$\sigma^2(S) = \sigma^2(E) \sum_j g^2(t_j), \tag{6.25}$$

where $\sigma(E)$ is the RMS of the energy deposited by minimum bias collisions from each bunch crossing. This simplification is only valid if the number of minimum bias collisions is very high. If the luminosity is very low, then the distribution of energy from pileup is very non-Gaussian. However, at the luminosities of the LHC, this is a

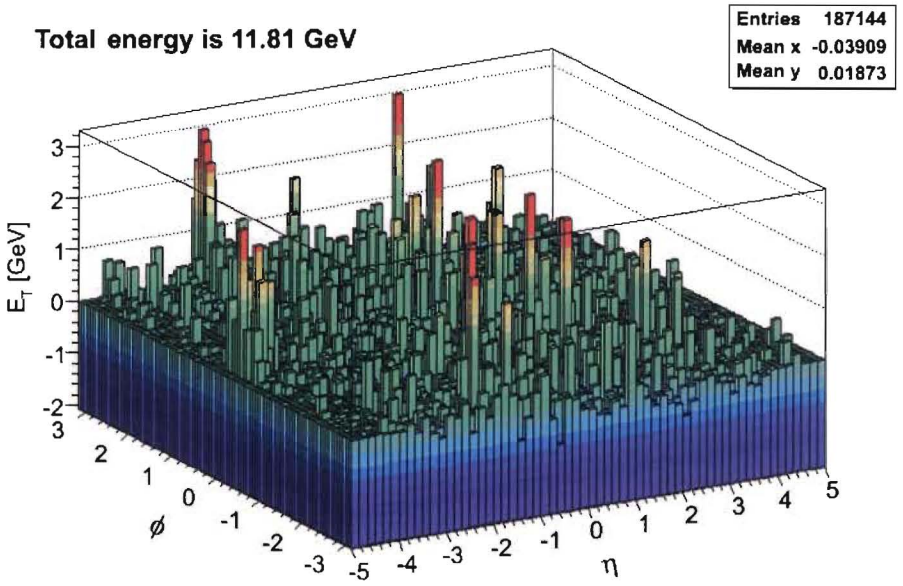

Figure 6.3: Total E_T from pileup in the ATLAS calorimeter. This plot uses a minimum bias event with pileup at 4/5 design luminosity. Since the total E_T in the entire calorimeter is so low, the result that the measured signal should have no positive offset is verified.

valid assumption, and the non-zero response time of the ATLAS calorimeters has the effect of increasing the width of the signal distribution due only to event pileup

$$\sigma^2_{\text{total-pileup}} = \sigma^2_{\text{event-pileup}} \times I_{\text{electronics}}, \tag{6.26}$$

where $I_{\text{electronics}}$ is a multiplicative factor > 1 depending on the calorimeter pulse shape. For the ATLAS EM calorimeters it is about 2.18 [28].

6.3 Pileup Datasamples

In order to measure the pileup noise correlations discussed in Section 6.1, and to study pileup suppression techniques, minimum bias events were simulated at various luminosity settings. The events were generated in Pythia 6.22 and were simulated in the detector using Geant4. This was done as part of the Monte Carlo production for

the Rome Physics Workshop in 2005[3]. The Pythia datacards used for generating the minimum bias events are shown in Table 6.1.

pysubs msel 1	*select* $2 \longrightarrow 2$ *dijet processes*
pypars mstp 82 4	
pydat1 mstj 11 3	*fragmentation scheme is a hybrid Lund model*
pydat1 mstj 22 2	*cut off on decay length for allowed particle decays*
pydat1 parj 54 -0.07	*parameter for c quark fragmentation*
pydat1 parj 55 -0.006	*parameter for b quark fragmentation*
pypars parp 82 1.8	*scale for* p_T *in underlying event*
pypars parp 84 0.5	*parameter for matter distribution in colliding hadrons*

Table 6.1: Datacard options used to generate minimum bias events for this study. The second group of parameters are common for all processes.

6.4 Pileup Suppression

One of the ways that pileup contributions to the noise can be reduced is by using topological clustering to preferentially select cells with a high signal to noise ratio. Topological clusters are constructed using an algorithm which considers the energy distribution among neighbouring cells:

- each cell with $|E_T| > 4\sigma$ is taken as a seed, where σ is the noise RMS (pileup $\oplus$ electronic)
- the cluster is extended to all cells with $|E_T| > 2\sigma$
- all cells neighbouring $|E_T| > 2\sigma$ cells are also kept ($|E_T| > 0\sigma$).

This scheme is referred to as $4-2-0$ topological clustering. These clusters can be 3-dimensional and can span across different subdetectors. A simple 2-dimensional example of a topological cluster is shown in Figure 6.4. Analogous algorithms exist using different noise cuts, eg. the 6-3-0 topological cluster. In calculating σ, the expected contribution of pileup noise to the total cell noise is used. This is currently

[3]The data was simulated in Athena r10.0.1 using the 'Rome-Initial' geometry version.

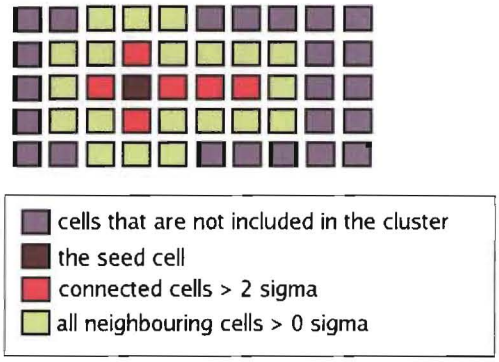

Figure 6.4: An example of a topological cluster using the 4-2-0 algorithm. The seed cell satisfies $|E_T| > 4\sigma$. The cluster grows to all connected cells with $|E_T| > 2\sigma$. Finally, all neighbouring cells are added to the cluster.

calculated from Monte Carlo simulations. The values for the noise are dependent on the luminosity, specified by the number of minimum bias collisions per bunch crossing, and are calculated by a software tool in the Athena framework.

We found that introducing topological clustering is effective in reducing the level of pileup noise. However, a bias is introduced in the mean pileup E_T. This is shown in Figures 6.5 - 6.10 where various values for $\sigma(\text{pileup} \bigoplus \text{electronic})$ were used in the topological clustering algorithm. Studies were performed on the barrel and endcap regions of the calorimeter, and at three luminosity levels.

By introducing topological clustering with a σ(pileup) appropriate for the luminosity conditions (in this case 1/2 design luminosity, or 11.5 minimum bias collisions per crossing), Figure 6.6 shows that the level of pileup noise in a $\Delta R = 0.7$ cone of the barrel calorimeter can be reduced by half from the case where no topological clustering is used. However, a 10 GeV bias is introduced in the mean E_T. This is worse for high luminosity pileup, where the bias introduced into the mean is 14 GeV. This may have a strong effect on jet reconstruction for low-E_T jets in the barrel region.

In the endcap region the effect of the topological clustering is more effective in reducing the pileup noise. Also, the bias on the mean introduced by the clustering is less severe, as shown in Figure 6.9, where the mean E_T is 5 GeV in a $\Delta R = 0.7$ cone. At high luminosity the mean is even less biased in the endcap, and the topological

clustering reduces the pileup noise RMS to below 4 GeV, as shown in Figure 6.10. This is attributed to the fact that the pulse shaping in the LAr calorimeters is more effective at higher luminosities, where the approximation of pileup as a constant noise source is more valid.

The situation is slightly different in the barrel region, because the TILE calorimeter does not employ bipolar pulse shaping. Therefore, a slight positive bias in the mean from pileup energy is expected in the barrel. The larger positive bias introduced by topological clustering may be understood by considering the distribution of pileup energy in a $\Delta\eta \times \Delta\phi$ region as shown in Figure 6.11. There is a clear asymmetric tail at large positive energies. Thus, when applying cuts to $|E_T|$, one is effectively making the positive tail more significant by increasing the fraction of topoclusters made from positive pileup noise. The effect of increasing the pileup cuts in the topological clustering is also apparent in the E_T distribution of all topological clusters, as shown in Figure 6.12.

6.5 Minimum Bias

Besides adding noise to the detector, pileup also adds real physics signals (such as jets). This was neglected in developing the model of event pileup in Section 6.1. In order to estimate how pileup physics signals affect the γ + jet in-situ calibration scheme, datasets of minimum bias events were reconstructed using the algorithms in release 11.0.41 of the Athena framework. Using the seeded-cone $\Delta R = 0.4$ jet algorithm (see Section 4.1.1) we found that there is a non-negligible probability to reconstruct jets with significant p_T just from pileup at 1/2 design luminosity. This is summarized in Table 6.2. The reconstructed jet p_T spectrum and multiplicity for 1/2 and 4/5 design luminosity pileup are shown in Figures 6.13 - 6.14. The p_T spectrum of photons reconstructed from minimum bias collisions at 1/2 and 4/5 design luminosity pileup is shown in Figures 6.15 - 6.16. These photons pass the cuts for signal photons in the MPF calibration shown in Tables 5.4 and 5.6. The fact that jets and photons with significant p_T are reconstructed from pileup indicates one of the ways that pileup will affect the in situ calibration scheme. This is the focus of the following chapter.

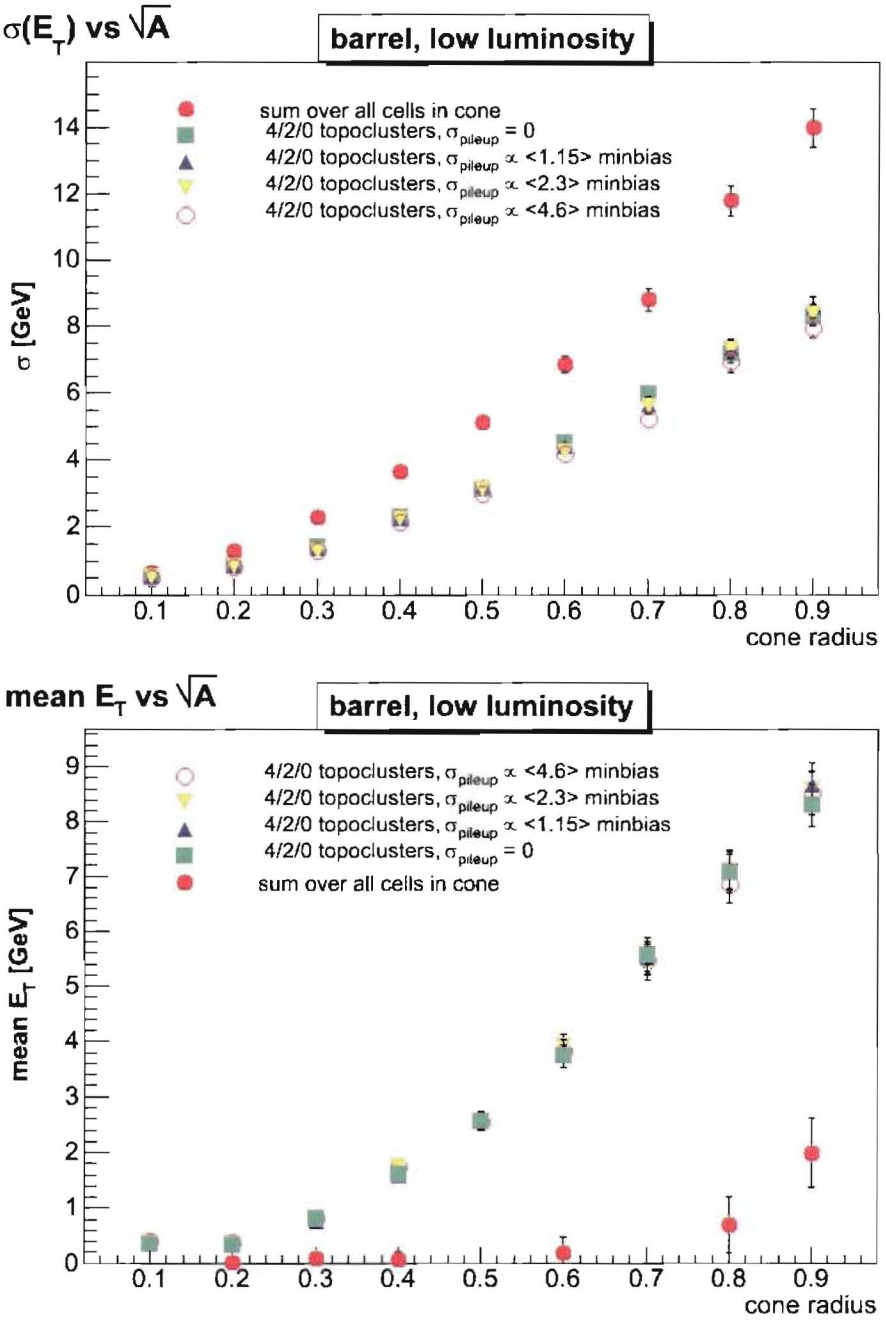

Figure 6.5: The pileup E_T RMS (top) and $\langle E_T \rangle$ (bottom) versus cone radius in the barrel, shown for various cuts on σ and for no topological clustering. The cone is centered at $(\eta, \phi) = (0.15, 1.25)$. Rome M1 minbias data were used, with pileup corresponding to 1/5 design luminosity (4.6 minimum bias events per crossing).

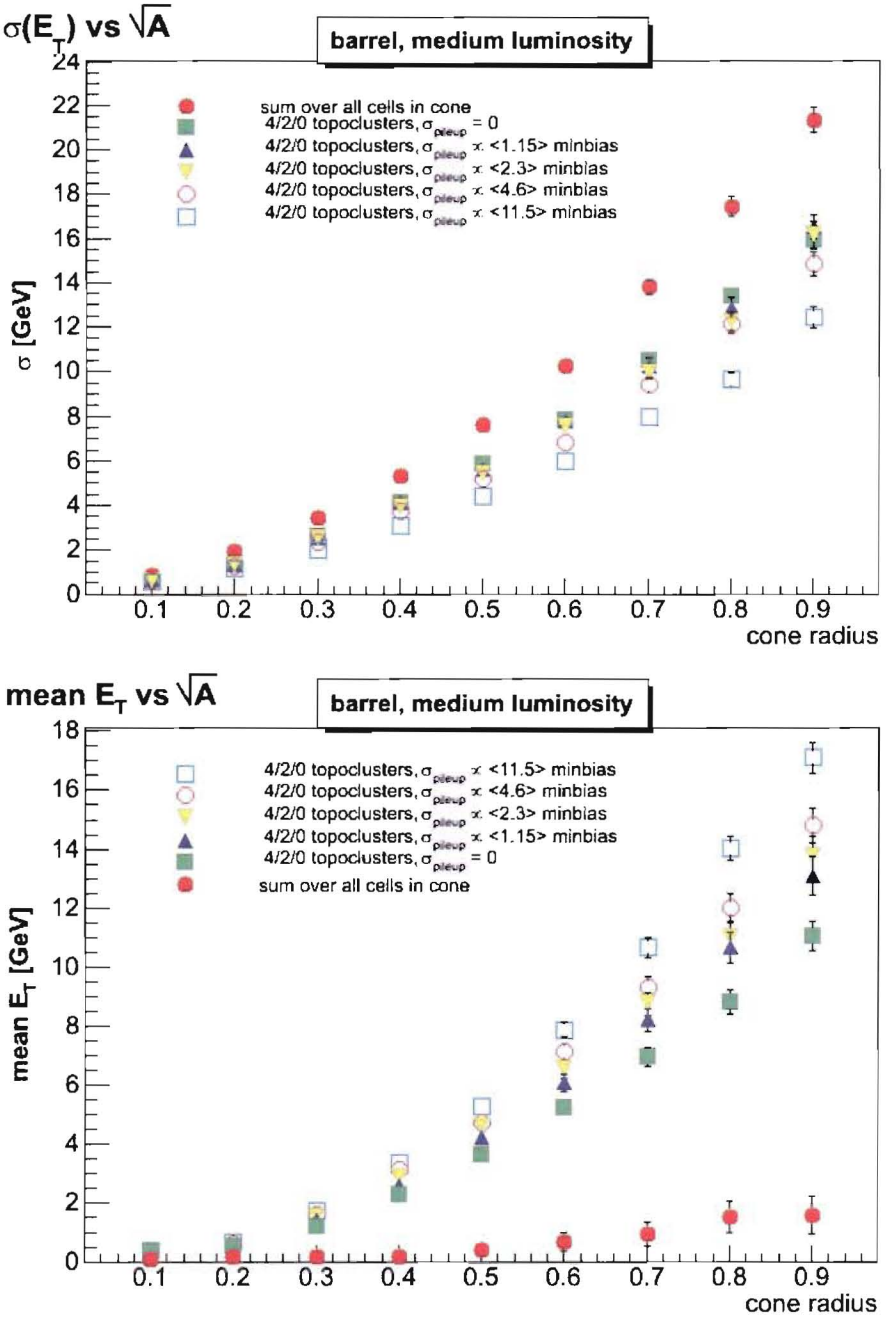

Figure 6.6: The pileup E_T RMS (top) and $\langle E_T \rangle$ (bottom) versus cone radius in the barrel, shown for various cuts on σ and for no topological clustering. The cone is centered at $(\eta, \phi) = (0.15, 1.25)$. Rome M1 minbias data were used, with pileup corresponding to 1/2 design luminosity (11.5 minimum bias events per crossing).

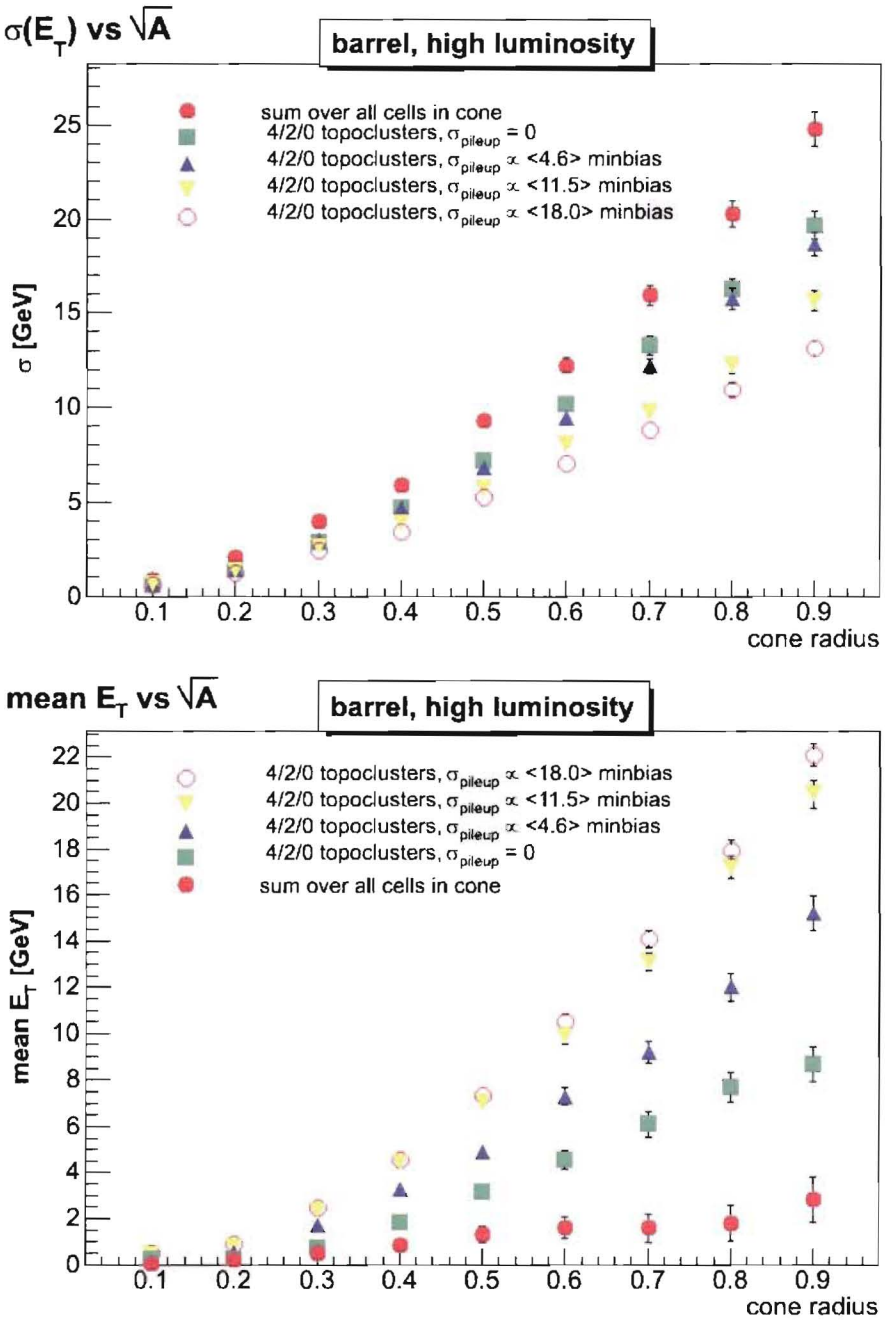

Figure 6.7: The pileup E_T RMS (top) and $\langle E_T \rangle$ (bottom) versus cone radius in the barrel, shown for various cuts on σ and for no topological clustering. The cone is centered at $(\eta, \phi) = (0.15, 1.25)$. Rome M1 minbias data were used, with pileup corresponding to 4/5 design luminosity (18.0 minimum bias events per crossing).

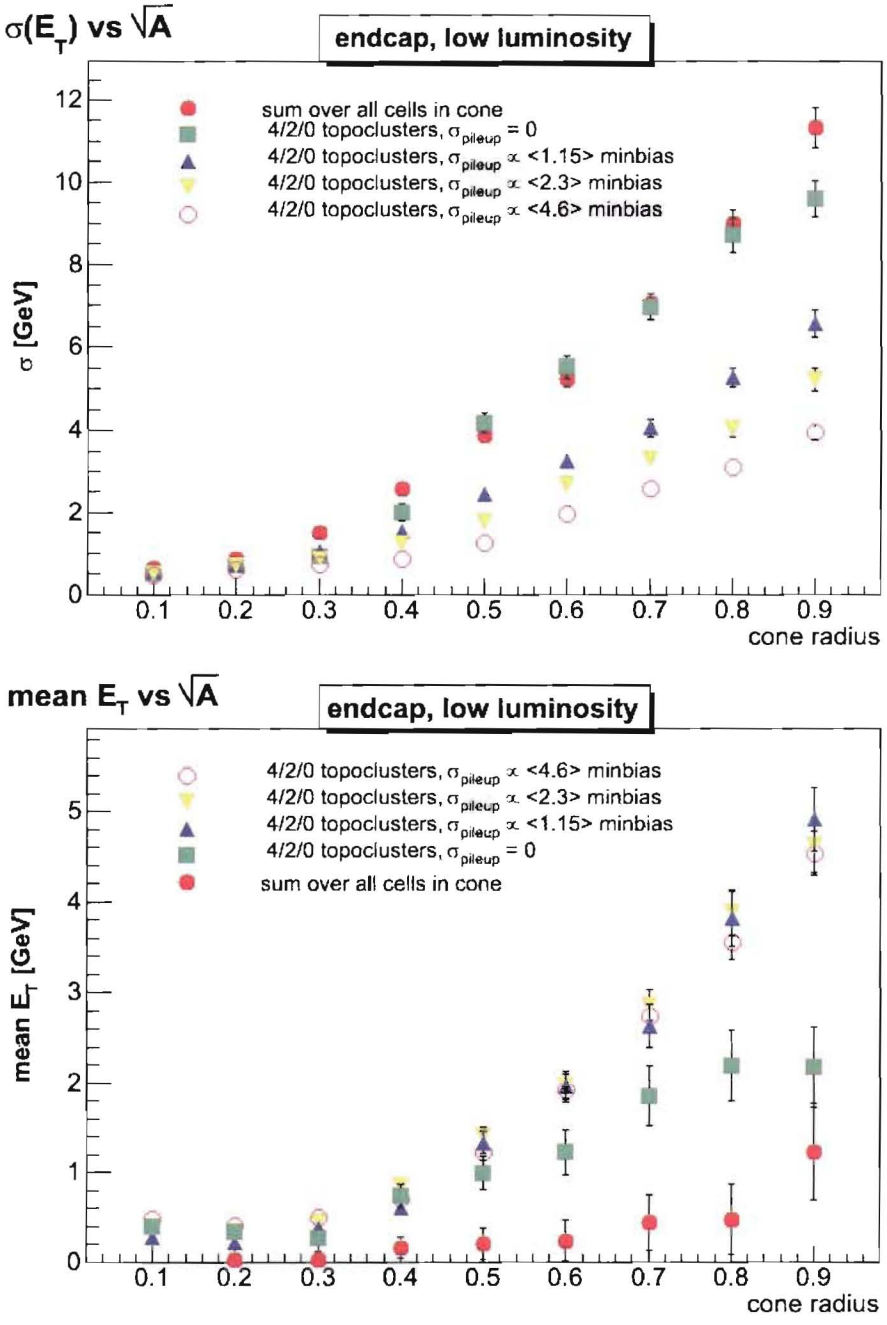

Figure 6.8: The pileup E_T RMS (top) and $\langle E_T \rangle$ (bottom) versus cone radius in the endcap, shown for various cuts on σ and for no topological clustering. The cone is centered at $(\eta, \phi) = (2.4, 1.25)$. Rome M1 minbias data were used, with pileup corresponding to 1/5 design luminosity (4.6 minimum bias events per crossing).

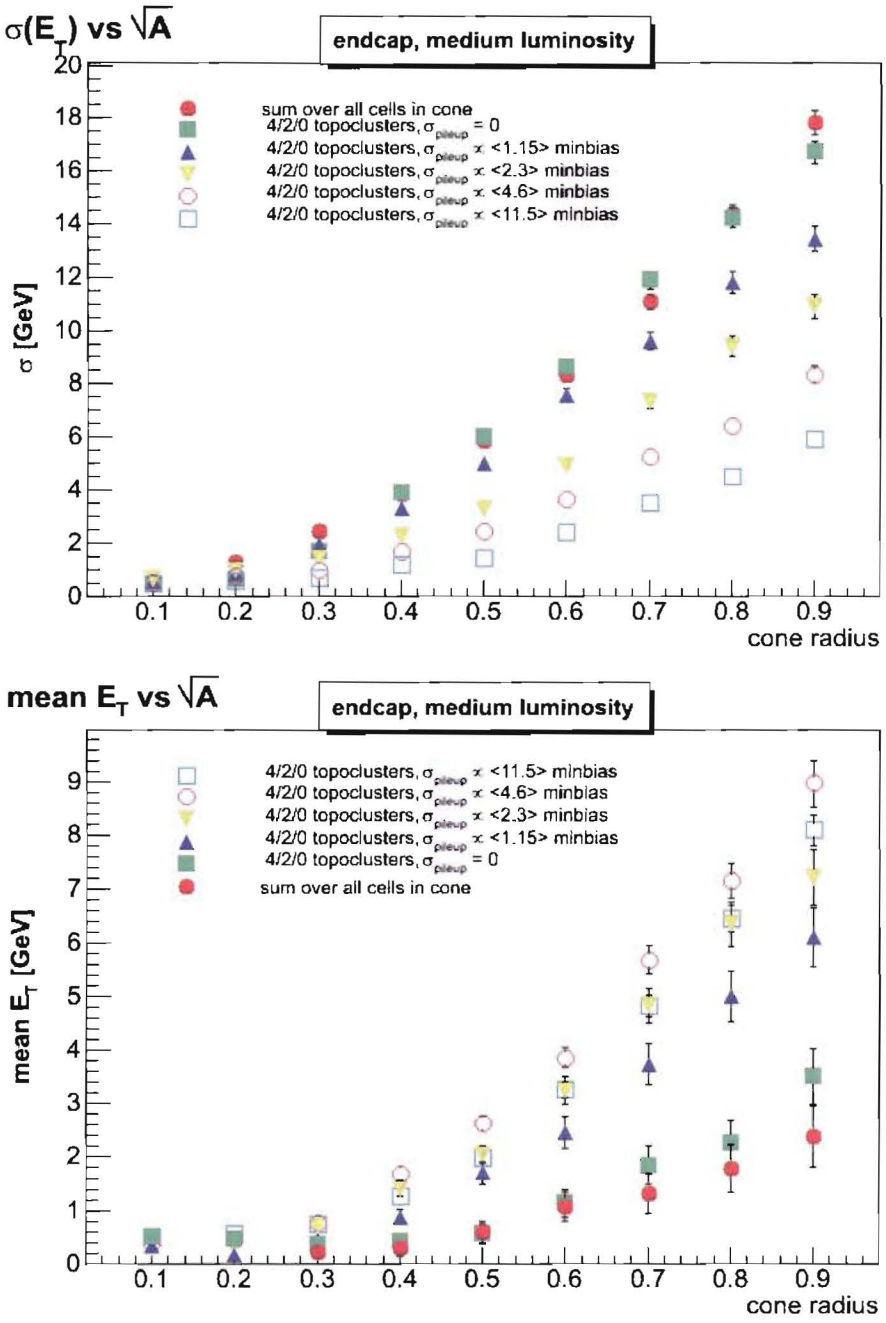

Figure 6.9: The pileup E_T RMS (top) and $\langle E_T \rangle$ (bottom) versus cone radius in the endcap, shown for various cuts on σ and for no topological clustering. The cone is centered at $(\eta, \phi) = (2.4, 1.25)$. Rome M1 minbias data were used, with pileup corresponding to 1/2 design luminosity (11.5 minimum bias events per crossing).

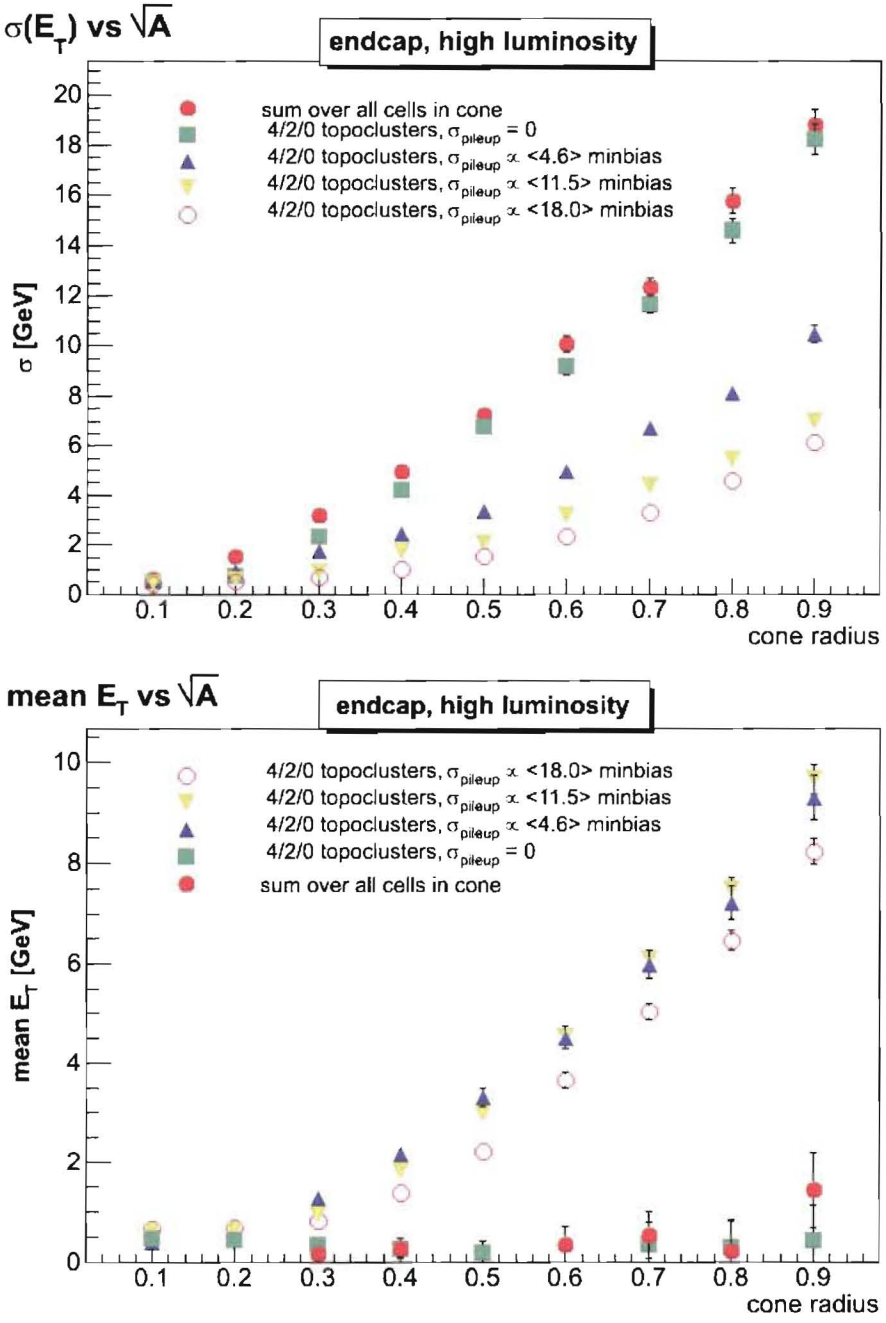

Figure 6.10: The pileup E_T RMS (top) and $\langle E_T \rangle$ (bottom) versus cone radius in the endcap, shown for various cuts on σ and for no topological clustering. The cone is centered at $(\eta, \phi) = (2.4, 1.25)$. Rome M1 minbias data were used, with pileup corresponding to 4/5 design luminosity (18.0 minimum bias events per crossing).

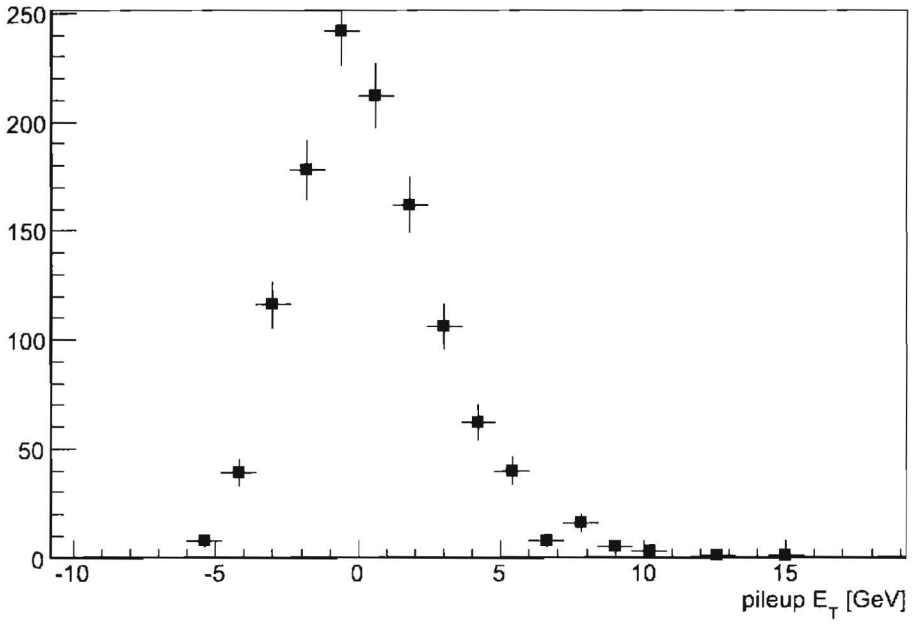

Figure 6.11: The E_T distribution of pileup energy in a $\Delta R = 0.2$ region of the barrel calorimeter centered at $(\eta, \phi) = (0.15, 1.25)$. The non-Gaussian positive tail is clearly visible. This plot uses pileup data at 1/2 design luminosity.

jet p_T threshold cut	11.5 mb/crossing (%)	18 mb/crossing (%)
20.0 GeV	33.5	42.6
30.0 GeV	15.1	21.9
40.0 GeV	8.8	12.8

Table 6.2: Fraction of events that have $N_{\text{jets}} \geq 1$ and $p_T^{\text{leading}} \geq p_T^{\text{threshold}}$ using the seeded cone algorithm with $R = 0.4$.

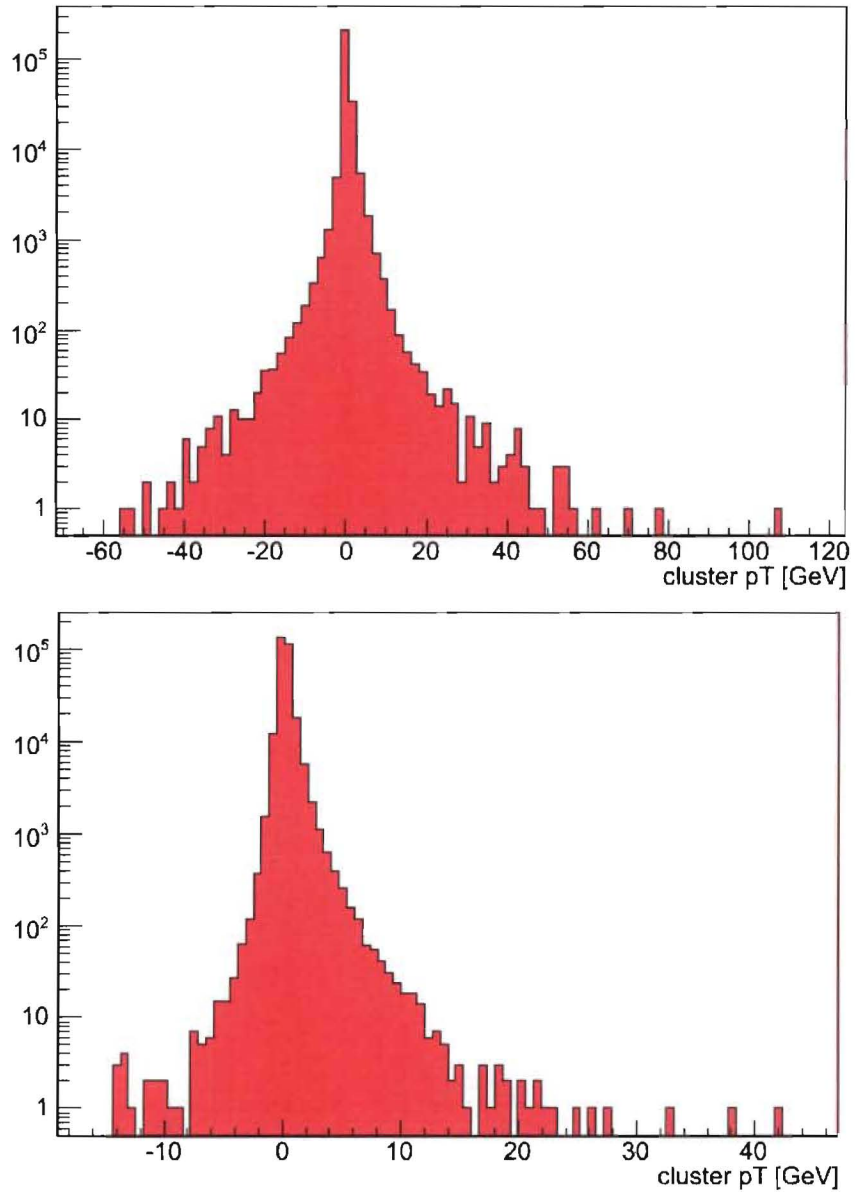

Figure 6.12: The E_T distribution of topological clusters from pileup, with no cut on pileup noise (top) and with σ(pileup) set for 1/2 design luminosity (bottom). Both plots use Rome M1 minimum bias data at 1/2 design luminosity. It is clear that the cut on pileup noise skews the E_T distribution of topological clusters made from pileup. Note that the horizontal scale changes between the two plots.

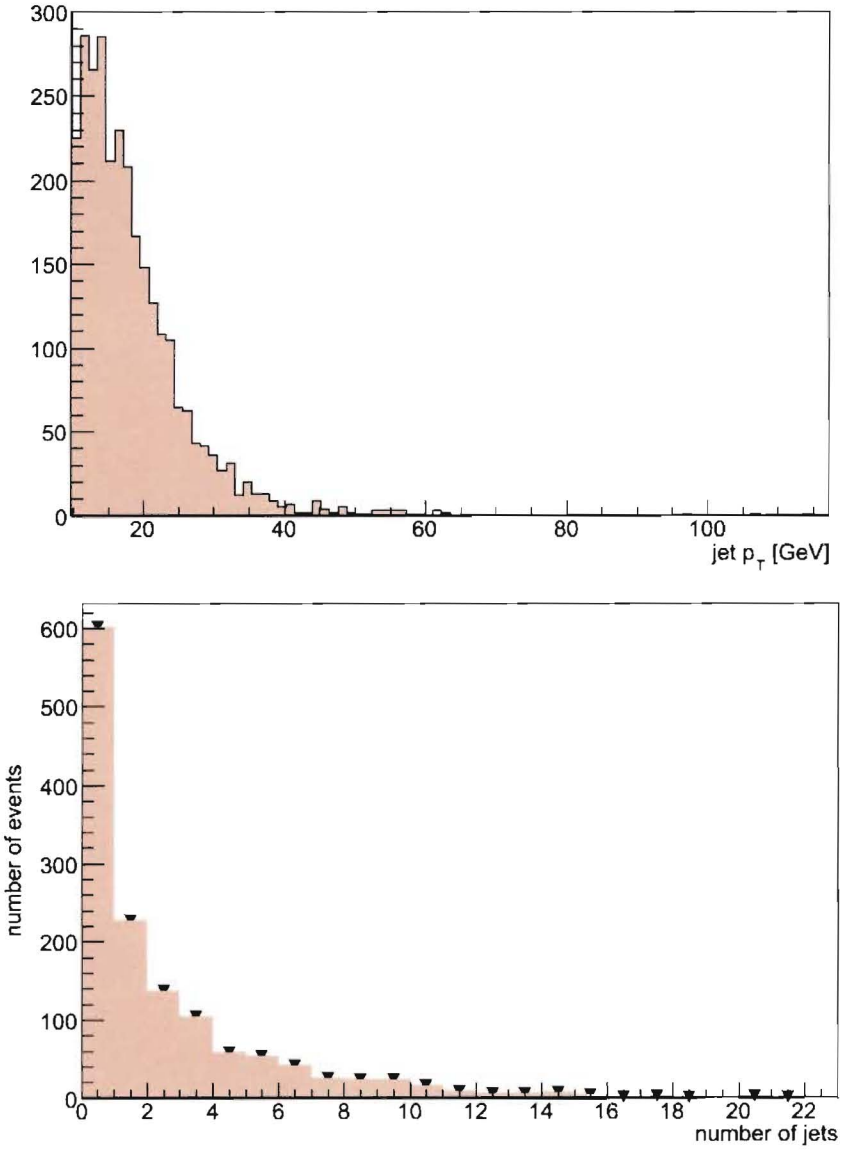

Figure 6.13: The p_T spectrum (top) and multiplicity of jets (bottom) from pileup at 1/2 design luminosity.

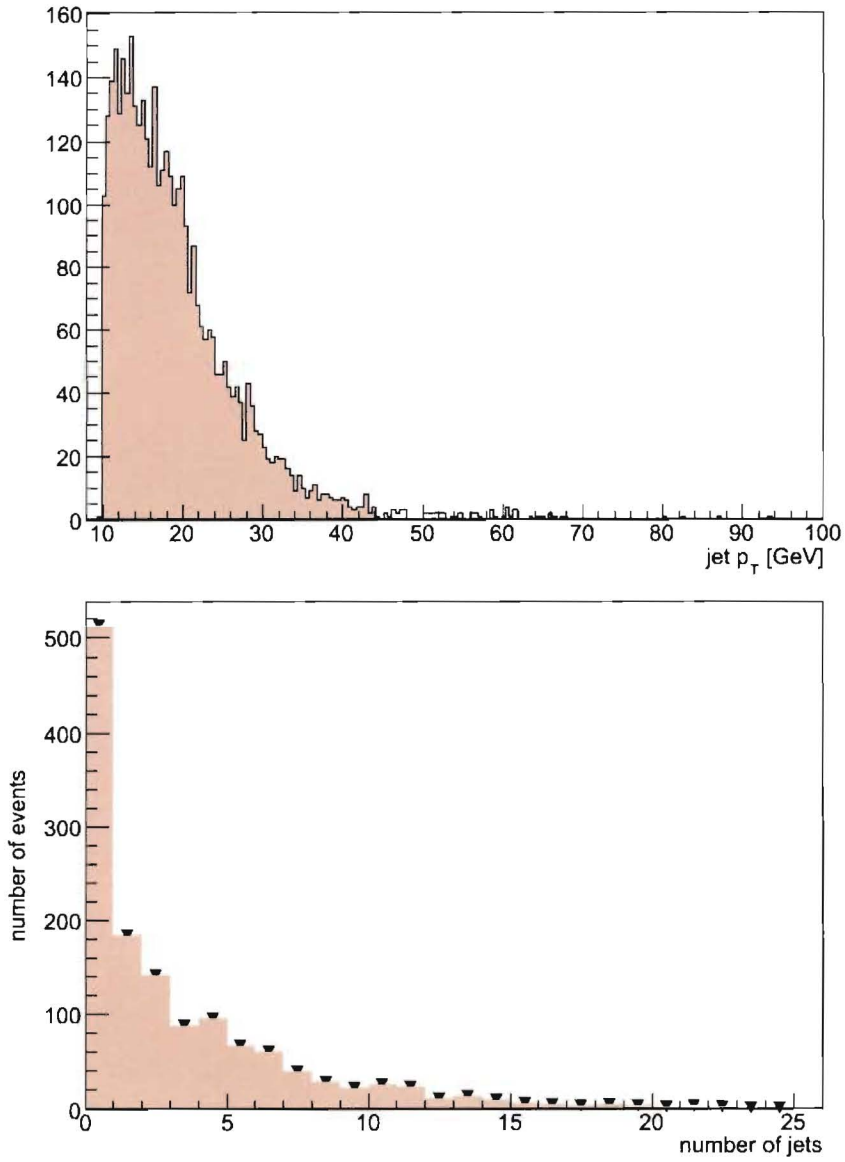

Figure 6.14: The p_T spectrum (top) and multiplicity of jets (bottom) from pileup at 4/5 design luminosity.

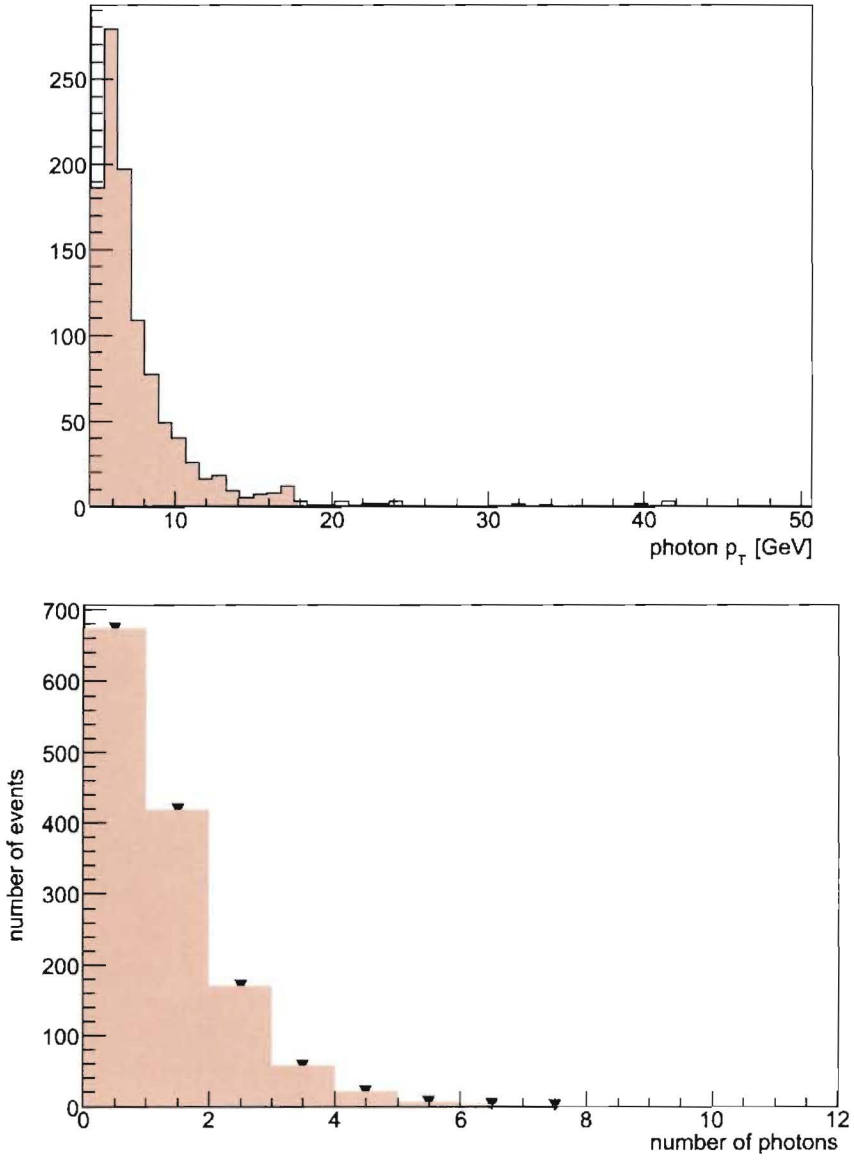

Figure 6.15: The p_T spectrum (top) and multiplicity (bottom) of photons from pileup at 1/2 design luminosity.

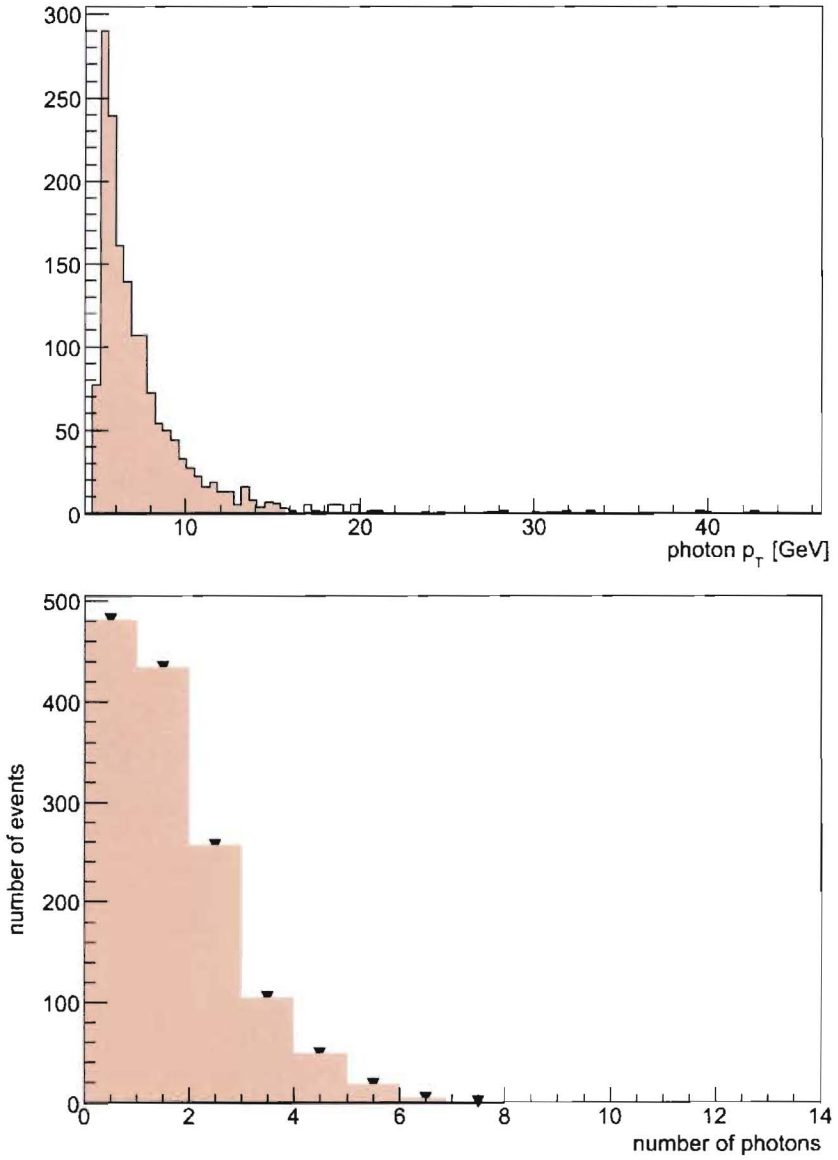

Figure 6.16: The p_T spectrum (top) and multiplicity (bottom) of photons from pileup at 4/5 design luminosity.

Chapter 7

Pileup and the Jet Energy Scale

The jet response calculation is, in a naive sense, unaffected by the presence of pileup noise since, as was shown in Section 6.2, there is not a significant baseline energy shift due to the addition of pileup energy. This is because of the electronics pulse shaping employed by the LAr calorimeters. Therefore, it is expected that although the resolution of the jet energy may be aversely affected by pileup fluctuations, the energy scale should remain unchanged.

However, upon closer inspection it becomes apparent that the measurement of the jet energy scale is susceptible to pileup effects in a number of ways. First, as was shown in Section 6.5, the additional minimum bias collisions from event pileup add real physics signals to the event. Photons and jets from these minimum bias collisions are indistinguishable from the photon and jet which come from the 'Compton-like' and quark annihilation hard scatter processes in Figure 5.2. The jet response calculation may be biased from events in which the signal photon and jet are misidentified. This signal misidentification is discussed in Section 7.2.

Another way that pileup can affect the jet energy scale measurement is by skewing the $\not{E}_T$ calculation due to the addition of poorly calibrated jets outside of the γ + jet system. In other detector environments this bias can be reduced by discarding events that have a significant amount of energy deposited outside of the γ + jet system [23]. However, such a cut is untenable in ATLAS because of the high level of pileup activity. This is further discussed in detail in Section 7.3.

Finally, we expect that pileup affects the measurement of the jet energy scale by biasing the energy clustered by the jet algorithms. For example, as was shown in Section 6.4, a large positive offset can be expected when using topological clusters as inputs to the jet algorithms. This bias on the jet energy is discussed in Section 7.4.

7.1 Pileup Datasets

In order to generate γ + jet datasets with additional pileup interactions, minimum bias events were overlaid on top of events from the CSC `PhotonJet` datasets at the digitization stage (see Figure 3.11). Fully simulated events from the CSC `MinBias` (5001) dataset were used in this analysis. Pileup corresponding to three different luminosity levels was added as summarized in Table 7.1. The events digitized with pileup were then reconstructed using the standard Athena algorithms in release 12.0.3.

name	description	$< N_{mb} >$
`Lumi00`	no pileup	0.00
`Lumi02`	1/5 design luminosity	4.60
`Lumi05`	1/2 design luminosity	11.5

Table 7.1: The levels of pileup added to the `PhotonJet` datasets. The first column is the name used to identify the luminosity level. The second column contains a description with respect to the ATLAS design luminosity ($10^{34}\text{cm}^{-2}\text{s}^{-1}$). The third column specifies the pileup level in terms of the number of additional minimum bias events overlaid onto each γ + jet event. For `Lumi02` and `Lumi05`, this is the mean of a Poisson distribution (see Section 6.1).

7.2 Signal Misidentification

7.2.1 Photons

Figures 6.15 and 6.16 show the distributions of transverse momentum for photons reconstructed from pileup. It is seen that these photons have low transverse momentum. Recall that one of the signal photon criteria is that it be the leading photon

(see Section 5.4.1). Thus, for events in which the hard scatter photon is within the tracking range $\eta < 2.5$, the photon will not be misidentified, except for very low E_T events.

By applying the photon signal selection criteria and comparing the selected photon to the known true photon in the Monte Carlo, we can determine what the expected misidentified photon rate due to pileup is. A plot of the signal photon p_T versus ΔR between the true photon and the signal photon for three levels of pileup is shown in Figure 7.1. This shows that by applying a 15.0 GeV cut on the minimum p_T of the signal photon, a significant fraction of the pileup fakes can be removed.

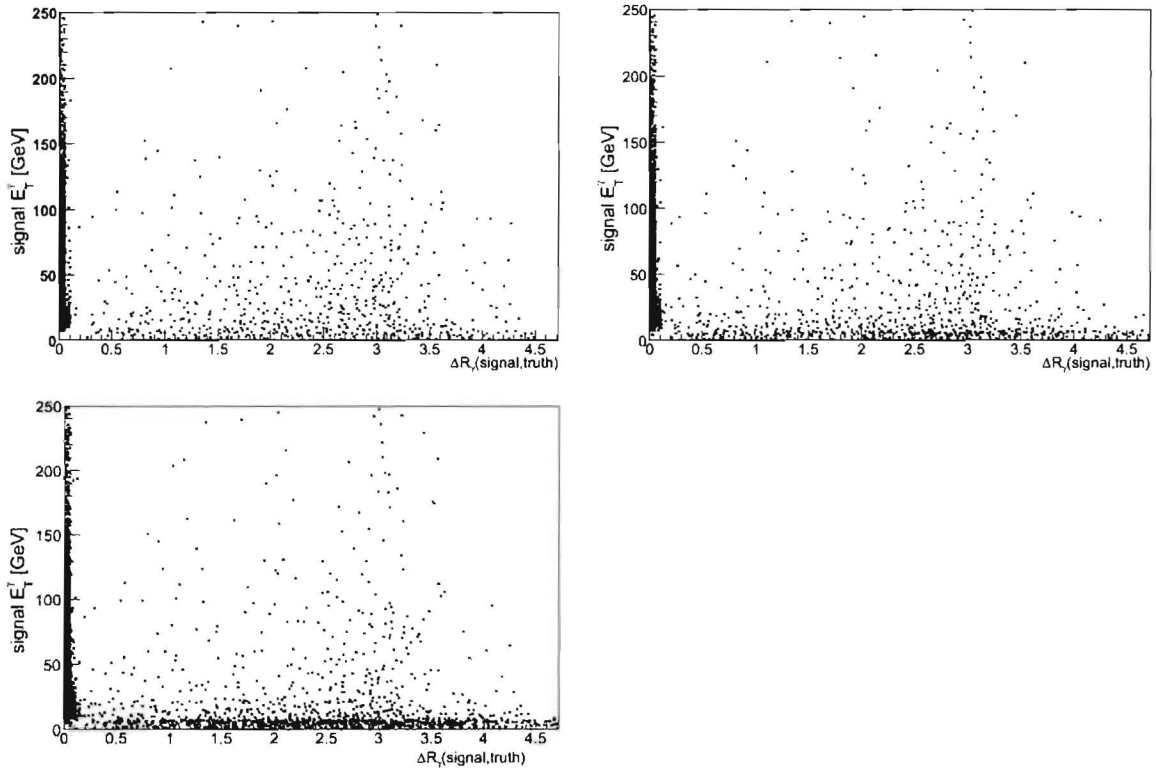

Figure 7.1: Distributions of the E_T of the signal photon versus ΔR between the signal photon and the photon from the hardscatter process (ISUB=14 or 29) for the pileup datasets `Lumi00` (top left), `Lumi02` (top right), and `Lumi05` (bottom left). The photon is said to be misidentified if $\Delta R > 0.1$. These figures show that the fraction of misidentified photons increases with the addition of pileup and that a large fraction of the misidentified photons have $E_T < 15.0$ GeV.

luminosity	leading in $\Delta\phi$ window	leading in the event
no pileup	18.3%	14.1%
1/5 design luminosity	36.7%	22.2%
1/2 design luminosity	50.3%	28.8%

Table 7.2: The fraction of misidentified signal jets for three luminosity levels. This fraction is shown for two signal jet requirements: (1) leading in a $\Delta\phi$ window; (2) leading in the event with $\Delta\phi > 2.8$.

7.2.2 Jets

Signal jets are selected by choosing the leading jet which satisfies the angular separation $\Delta\phi > 2.9$ cut. When jet multiplicities are very high due to the addition of jets from pileup there is an increased probability that the signal jet is misidentified. The signal jet is said to be misidentified when ΔR between the nearest true jet from the hard scatter and the selected signal jet exceeds 0.2. Using this criterion, the fraction of misidentified signal jets exceeds 50% for `Lumi05` data[1]. However, by demanding that the matched jet be the leading jet in the event instead of only the leading jet in a $\Delta\phi$ window, the background from pileup fakes is significantly reduced.

This cut significantly reduces the statistics for the low E_T γ + jet events however, since there are significant numbers of events with pileup jets that have large transverse energies. This motivates loosening the angular separation cut to $\Delta\phi > 2.8$. The effect of the leading jet requirement is shown for three luminosity settings in Figure 7.2 and Table 7.2, which shows that for `Lumi05` data, the fake rates from pileup are reduced by $> 20\%$. For the `Lumi00` data, this additional cut is essentially moot, since the only jets in the event are the ones from the hardscatter and underlying event.

7.3 $\not\!\!E_T$ Pileup Bias

By using the $\not\!\!E_T$ projection fraction method of calculating the jet response (see Eq. 5.10), the measured response is strongly affected by biases in the $\not\!\!E_T$ measurement,

[1]Although this may be somewhat of an overestimation because the signal jets can have their energy-weighted centroids shifted by the addition of pileup energy.

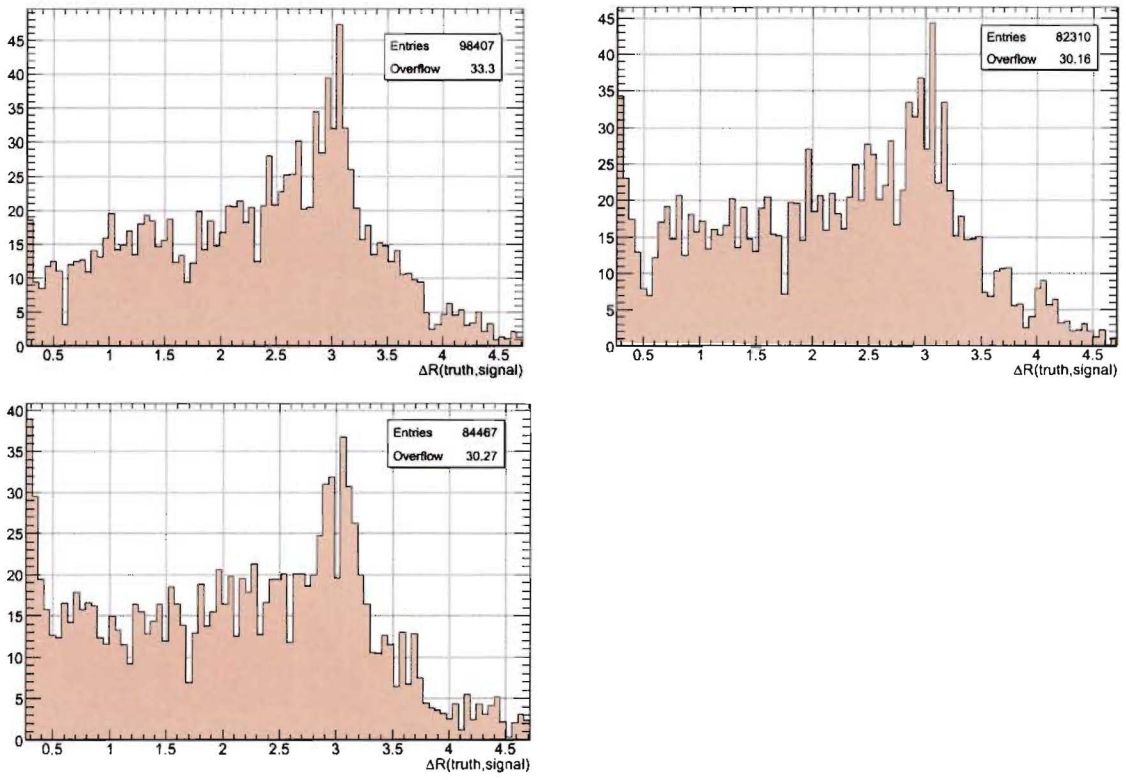

Figure 7.2: The distributions of ΔR between the signal jet and nearest match in the Monte Carlo from the hardscatter process for the datasets `Lumi00` (top left), `Lumi02` (top right), and `Lumi05` (bottom left). Note that the horizontal axis is truncated.

especially for low p_T events. In order to see how pileup can affect the response measurement, consider that

$$\vec{\not{E}}_T^{meas} = \vec{\not{E}}_T^{\gamma+jet} + \vec{\not{E}}_T^{pileup}, \tag{7.1}$$

i.e., the measured $\vec{\not{E}}_T$ in γ + jet events consists of a part due to the imbalance in the γ + jet system due to hadronic shower development and a part from the imbalances due to poorly measured jets or mini-jets in the pileup and underlying event. The necessary condition for pileup to bias the response measurement is that

$$\langle \vec{\not{E}}_T^{pileup} \cdot \hat{n}_\gamma \rangle \neq 0. \tag{7.2}$$

In other words, the transverse energy imbalance from pileup must not be azimuthally symmetric, but must rather be (anti)correlated with the direction of the γ. If the transverse energy imbalance from pileup was ϕ symmetric on average, the resolution of the response measurement would worsen but the mean would remain unchanged.

7.3.1 A Plausibility Argument

It is counter-intuitive to expect that the condition in Eq. 7.2 is true since the minimum bias events in pileup are distributed symmetrically in ϕ. However, consider the simple γ + jet event in Figure 7.3. In this picture, the condition that $\langle \vec{\not{E}}_T^{pileup} \cdot \hat{n}_\gamma \rangle > 0$ is equivalent to the condition that pileup energy in the jet hemisphere is preferentially included in the $\not{E}_T$ calculation versus pileup energy in the photon hemisphere. This condition is seen to be plausible because of three considerations:

- the jet(s) from the γ + jet event spread across many more cells than the photon, and therefore deposit appreciable energy in many more cells;
- a noise cut is applied such that only cells with $|E_T| > 2\sigma$ are included in the $\not{E}_T$ sum;
- the energy distribution in each cell from pileup is slightly asymmetric (see Figure 6.11).

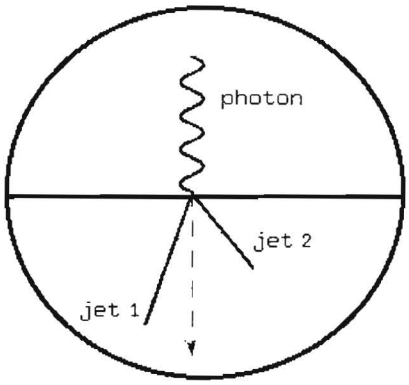

Figure 7.3: A simple γ + jet event in the transverse plane. The direction of the missing energy is shown by the dashed arrow. The plane is divided into a "photon hemisphere" (top) and a "jet hemisphere" (bottom).

These effects could combine such that on average, more cells with positive pileup noise from the jet hemisphere are included in the $\not\!\!E_T$ sum than from the photon hemisphere.

7.3.2 Measuring the Bias

In order to measure the existence of a bias on the $\not\!\!E_T$ measurement due to pileup, the quantities $\not\!\!E_T^{\gamma+jet}$ and $\not\!\!E_T^{pileup}$ must be disentangled. This can be done by considering that[2]

$$\vec{\not\!\!E}_T^{\gamma+jet} \approx -(\vec{E}_T^{\gamma} + \sum_{j*} \vec{E}_T), \tag{7.3}$$

where j^* refers to all energy depositions in the calorimeter from jets connected to the outgoing parton, shown pictorially in Figure 7.4. Therefore, $\not\!\!E_T^{\gamma+jet}$ can be calculated independently of $\not\!\!E_T^{meas}$ using only measured jet and photon quantities. The pileup imbalance term can then be calculated as

$$\begin{aligned} \vec{\not\!\!E}_T^{pileup} &= \vec{\not\!\!E}_T^{meas} - \vec{\not\!\!E}_T^{\gamma+jet} \\ &\approx \vec{\not\!\!E}_T^{meas} + \vec{E}_T^{\gamma} + \sum_{j*} \vec{E}_T. \end{aligned} \tag{7.4}$$

[2]This is only an approximation because there will be unclustered energy from the outgoing parton that is not included in any calorimeter level jet.

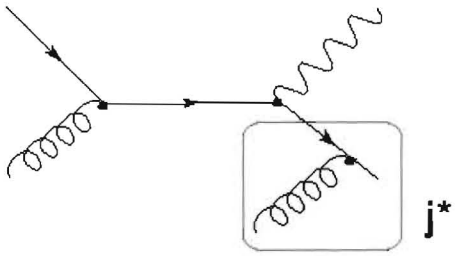

Figure 7.4: Feynman diagram of the "Compton like" scattering process showing possible FSR. Everything connected to the outgoing parton is included in j^*.

Thus, by measuring $\overrightarrow{\not{E}}_T^{pileup} \cdot \hat{n}_\gamma$ at the three luminosity levels we can ascertain the sign and approximate size of any bias from pileup. This is shown in Figures 7.5 and 7.6, which indicate that the pileup biases the response calculation positively. The fit for the bias term $\overrightarrow{\not{E}}_T^{pileup} \cdot \hat{n}_\gamma / p_T^\gamma$ grows from -3.6% without pileup to 8.7% with the `Lumi05` data. Since the positive bias from pileup is independent of the p_T of the photon, the effect will be larger for low p_T γ + jet events.

7.4 Jet Energy Bias

It has been shown already in Section 6.4 that topological clustering, while reducing the level of noise due to pileup, results in a large positive bias on the measured signal. It is therefore expected that jet algorithms which use topological clusters as input will create jets with positively biased energies. This bias will increase with the level of pileup. In order to demonstrate this, the quantity ΔE_T is measured for each jet in each event, where

$$\Delta E_T = E_T^{true,jet} - E_T^{meas,jet}. \tag{7.5}$$

This is shown in Figure 7.7 for `ConeClusterJets` and `ConeTowerJets`. There is an obvious increase in $E_T^{meas,jet}$ with the addition of pileup for `ConeClusterJets`, whereas there is no such increase for `ConeTowerJets`. In both cases, the RMS of the distributions also grows with the addition of pileup. This is summarized in Table 7.3.

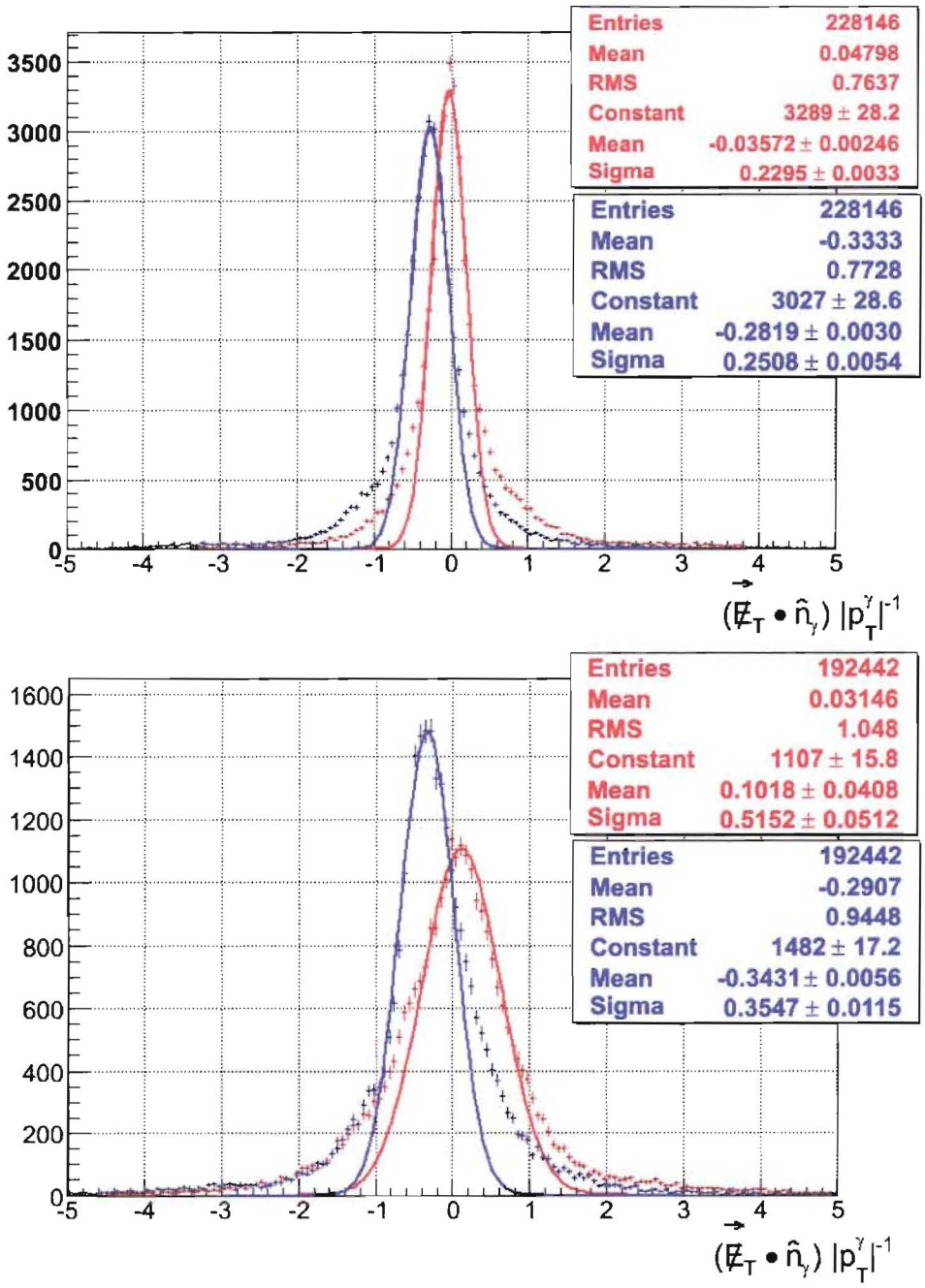

Figure 7.5: Distributions of the quantities $\overrightarrow{\not\!\!E}_T^{\gamma+jet} \cdot \hat{n}_\gamma/p_T^\gamma$ (blue) and $\overrightarrow{\not\!\!E}_T^{pileup} \cdot \hat{n}_\gamma/p_T^\gamma$ (red) for the `Lumi00` and `Lumi02` datasets. The bias term (red) is shown to increase with the addition of pileup.

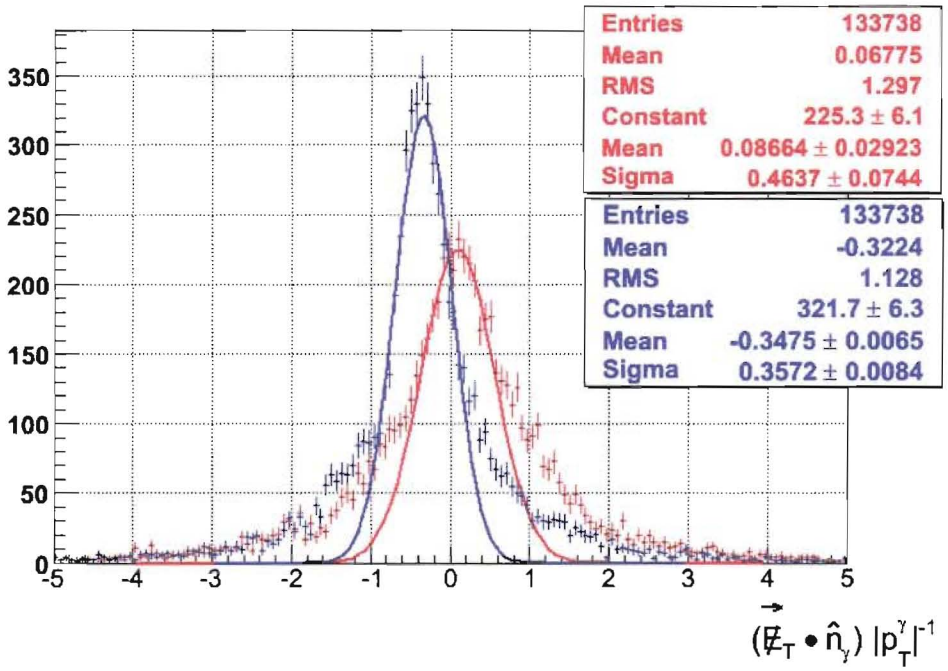

Figure 7.6: Distributions of the quantities $\vec{\not{E}}_T^{\gamma+jet} \cdot \hat{n}_\gamma / p_T^\gamma$ (blue) and $\vec{\not{E}}_T^{pileup} \cdot \hat{n}_\gamma / p_T^\gamma$ (red) for the `Lumi05` dataset. The bias term (red) is shown to increase with the addition of pileup.

jet algorithm	luminosity	$\langle E_T^{true,jet} - E_T^{meas,jet} \rangle$ in GeV
`ConeTowerJets`	no pileup	7.9
`ConeTowerJets`	1/5 design luminosity	9.2
`ConeTowerJets`	1/2 design luminosity	9.3
`ConeClusterJets`	no pileup	8.3
`ConeClusterJets`	1/5 design luminosity	3.7
`ConeClusterJets`	1/2 design luminosity	1.5

Table 7.3: The mean values of $E_T^{true,jet} - E_T^{meas,jet}$ for `ConeTowerJets` and `ConeClusterJets` with three levels of pileup. There is an obvious downward trend for `ConeClusterJets`.

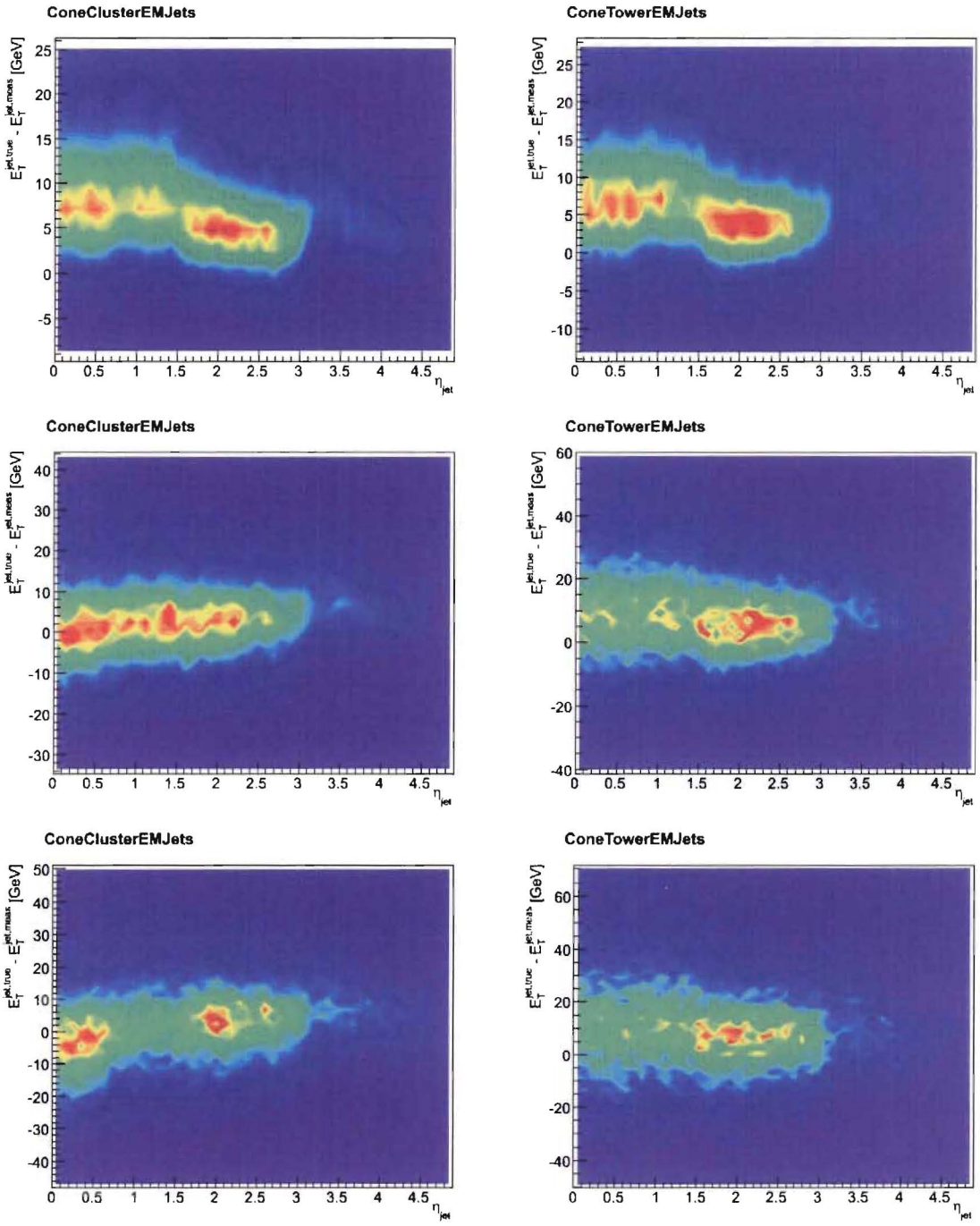

Figure 7.7: Energy offsets $E_T^{true} - E_T^{meas,jet}$ versus η for `ConeClusterJets` and `ConeTowerJets` and at `Lumi00` (top), `Lumi02` (middle), and `Lumi05` (bottom). The energy offset is calculated by comparing the E_T in calorimeter level jets to the nearest particle level jet within $\Delta R < 0.1$. There is a clear downward trend in the energy offset for `ConeClusterJets` with increased levels of pileup.

jet algorithm	b_0	b_1	b_2
ConeTowerJets	0.769 ± 0.009	0.042 ± 0.010	–0.014 ± 0.018
Cone4TowerJets	0.781 ± 0.009	0.030 ± 0.012	–0.017 ± 0.016
Kt4TowerJets	0.782 ± 0.009	0.027 ± 0.011	–0.016 ± 0.017
ConeClusterJets	0.777 ± 0.009	0.056 ± 0.010	–0.036 ± 0.020

Table 7.4: The fit parameters b_0, b_1, and b_2, and the absolute errors on the fits for the four different jet algorithms. These parameters are used in the logarithmic parameterization of the theoretical response function (Eq. 5.4). The scale parameter is $E_{scale} = 200.0$ GeV. This fit was performed using the Lumi02 data.

7.5 Measurement of the Jet Response

7.5.1 Signal Selection

The criteria used for identifying the signal photon and jet are identical to the criteria used in Section 5.4, with the following modifications:

1. a minimum cut of 15.0 GeV is applied to the photon E_T to minimize the effect of pileup fakes. Also, because of the high levels of pileup energy, the photon isolation criteria (Table 5.6) are somewhat weakened in the high luminosity environment in order to increase statistics. Specifically, $E_T^{isol} < 25.0\,\text{GeV}$ and $E_T^{isol} < 0.2E_T^{\gamma}$;

2. the signal jet is required to be the leading jet in the event, and is separated from the signal γ by $\Delta\phi > 2.8$.

7.5.2 Response for Lumi02 Data

The jet response was calculated in the Lumi02 data for Cone4TowerJets, ConeTowerJets, Kt4TowerJets, and ConeClusterJets. Only the logarithmic parameterization was used to fit the function $j(E)$. Otherwise, the analysis procedure is identical to the one specified in Section 5.4.4. The results of the calculation are summarized in Table 7.4 and Figure 7.8, and distributions of the measured jet energy and response in each E' bin are shown in Appendix C. The following observations can be made:

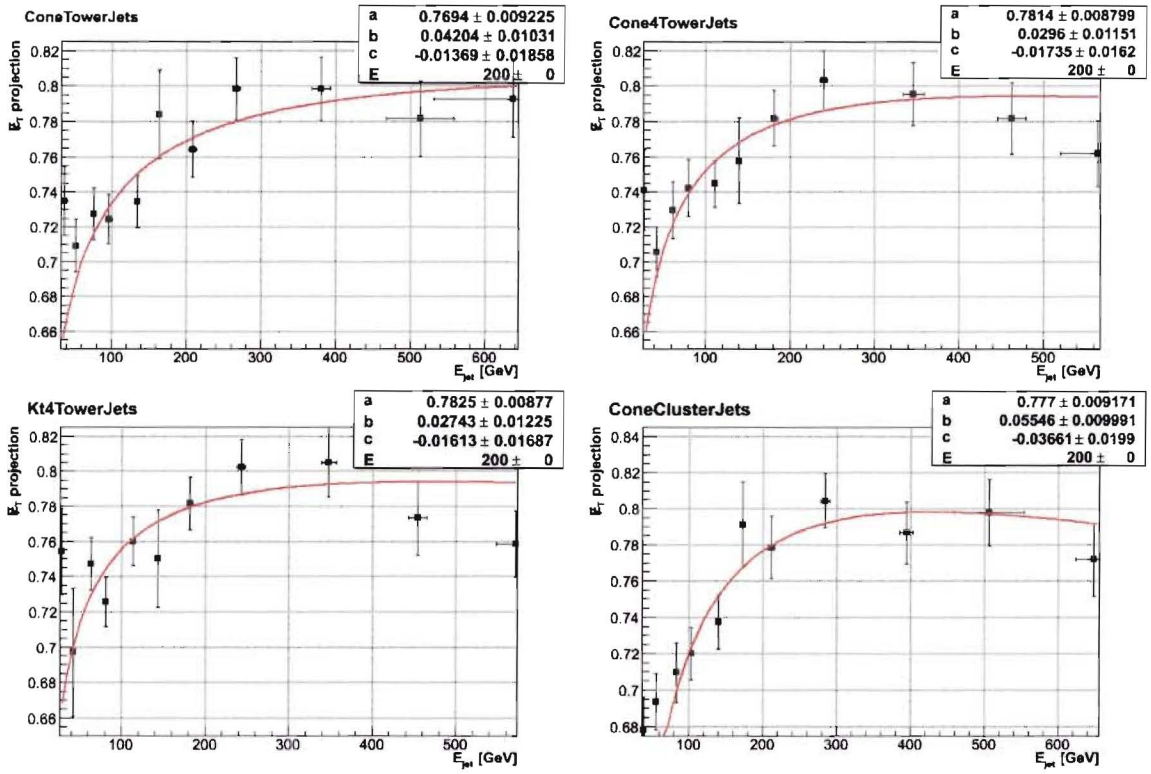

Figure 7.8: The energy dependence of the jet response for `ConeTowerJets` (top left), `Cone4TowerJets` (top right), `Kt4TowerJets` (bottom left), and `ConeClusterJets` (bottom right). These calculations are performed on the `Lumi02` data. The points are given by the fits for the jet response and jet energy in each of the E' bins (the lowest E' bin is excluded in the fits and is not shown in these plots). The solid line corresponds to the fit using the logarithmic parameterization (Eq. 5.4) with the parameters in Table 7.4.

1. the response distributions in each E' bin are much broader than for the case when there is no pileup. This is consistent with an increase in σ_{noise} from pileup.

2. there is an overall upwards shift of about 3 - 4% in the measured jet response from the case when there is no pileup, consistent with the observation of a bias from $\not{E}_T^{pileup}$.

The quality of the measured jet response calibration in the `Lumi02` data can be checked by calculating the quantities $r_{calib} \equiv E_T^{true,jet}/E_T^{calib,jet}$ and $r_{meas} \equiv E_T^{true,jet}/E_T^{meas,jet}$. These ratios are shown in Figure 7.9 for the four different jet algorithms. These plots indicate that the jet response calibration overestimates the response, and thus undercorrects the jet energy for `Cone4TowerJets` and `Kt4TowerJets`. However, it is apparent that a positive bias from pileup is introduced in the `ConeTowerJets` and `ConeClusterJets`. This is consistent with results found earlier in Section 6.4. We can therefore conclude that jets based on topological clusters are not suitable in an environment with significant pileup energy depositions.

If we instead use the measured jet response calibration for `Lumi00` data from Section 5.4.5, the linearity of the ratio r_{calib} for all but the `ConeClusterJets` is essentially regained. This is shown in Figure 7.10. This means that the jet energy scale remains unchanged with the addition of pileup even though the measurement of the jet response is positively biased and therefore incorrect. Therefore, a measurement of the jet response at low luminosity can be extrapolated to a higher luminosity environment.

7.5.3 Response for `Lumi05` Data

The jet response was calculated once more for the `Lumi05` data. The results are summarized in Table 7.5 and Figure 7.11. Due to the significant broadening of the jet energy and jet response distributions, the measurement is limited by statistics. The quality of the measured response calibration is shown in Figure 7.12. The `Lumi00` response calibration is applied to the `Lumi05` data in Figure 7.13. Similar conclusions

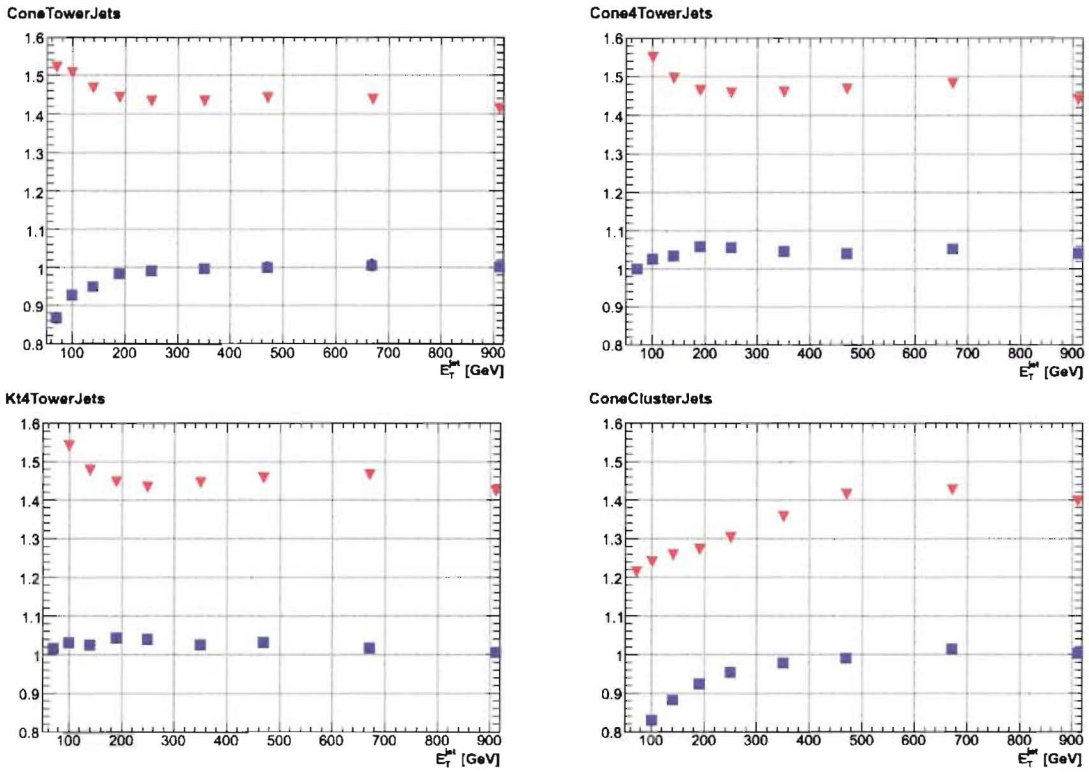

Figure 7.9: Plots showing the ratios r_{calib} (squares) and r_{meas} (triangles) for `ConeTowerJets` (top left), `Cone4TowerJets` (top right), `ConeClusterJets` (bottom left), and `Kt4TowerJets` (bottom right). The points in each bin are given by the fits for the ratio r_{calib} or r_{meas}. The calibration is done using the logarithmic parameterization of the jet response. The quantity $E_T^{calib,jet}$ is calculated using the calibration parameters in Table 7.4.

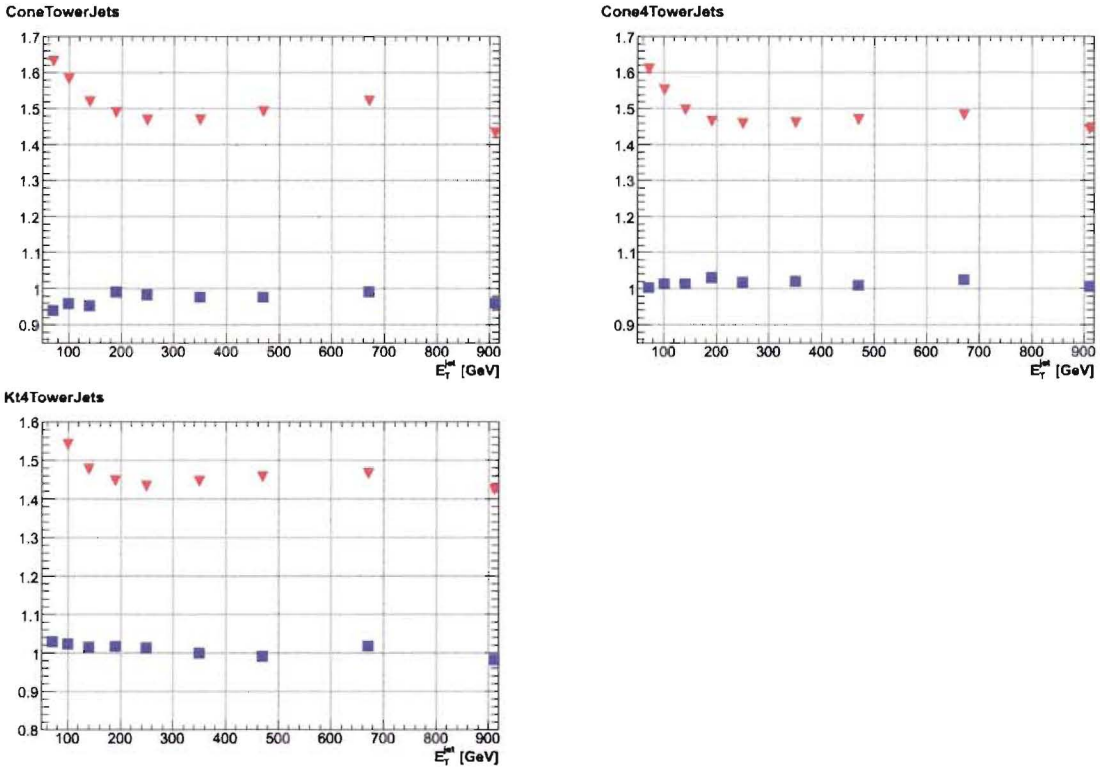

Figure 7.10: Plots showing the ratios r_{calib} (squares) and r_{meas} (triangles) for `ConeTowerJets` (top left), `Cone4TowerJets` (top right), and `Kt4TowerJets` (bottom left). The calibration is done using the logarithmic parameterization of the jet response using the calibration parameters for `Lumi00` data shown in Table 5.8.

jet algorithm	b_0	b_1	b_2
ConeTowerJets	0.781 ± 0.056	0.042 ± 0.016	-0.026 ± 0.032
Cone4TowerJets	0.786 ± 0.029	0.030 ± 0.012	-0.013 ± 0.016
Kt4TowerJets	0.800 ± 0.043	0.027 ± 0.011	-0.018 ± 0.017

Table 7.5: The fit parameters b_0, b_1, and b_2, and the absolute errors on the fits for the four different jet algorithms. These parameters are used in the logarithmic parameterization of the theoretical response function (Eq. 5.4). The scale parameter is $E_{scale} = 200.0$ GeV. These values are derived for Lumi05 data.

can be drawn for the Lumi05 data as for the Lumi02 data. Also, it is apparent that jets with a smaller R parameter are more suitable in the high luminosity environment, as shown by the better linearity in Cone4TowerJets and Kt4TowerJets over ConeTowerJets in Figures 7.12 and 7.13.

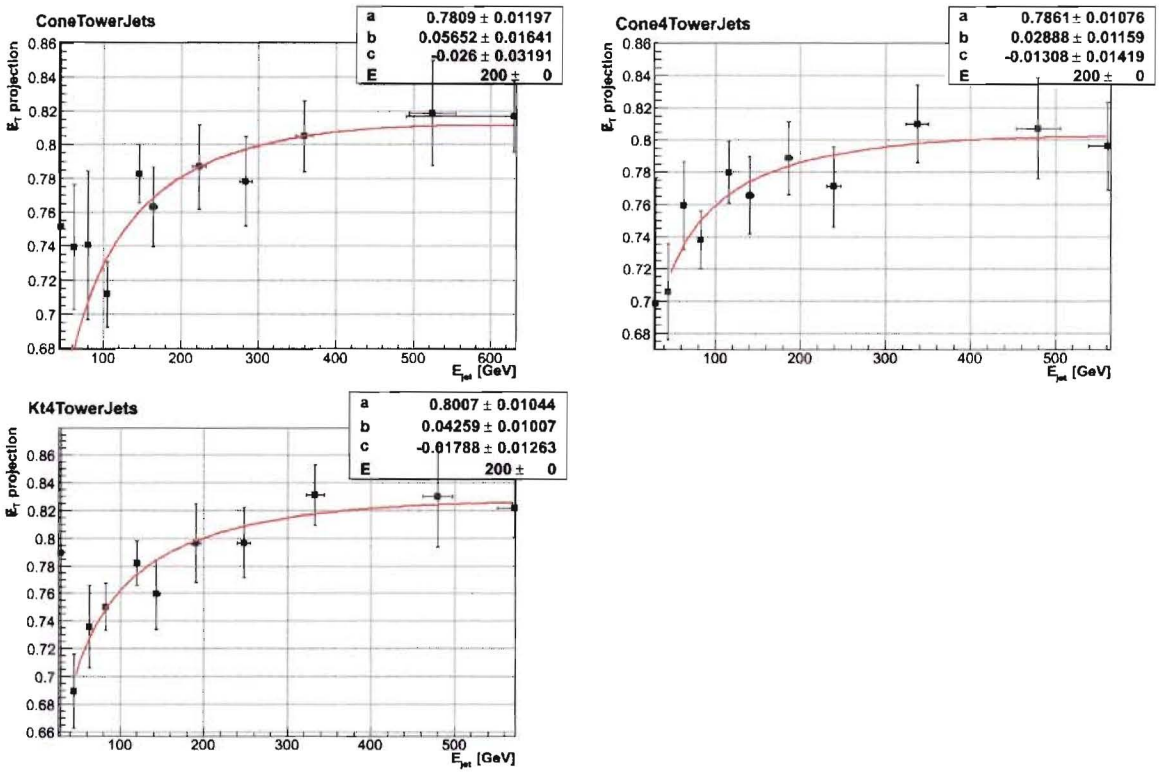

Figure 7.11: The energy dependence of the jet response for `ConeTowerJets` (top left), `Cone4TowerJets` (top right), and `Kt4TowerJets` (bottom left). These calculations are performed on the `Lumi05` data. The points are given by the fits for the jet response and jet energy in each of the E' bins (the lowest E' bin is excluded in the fits and is not shown in these plots). The solid line corresponds to the fit using the logarithmic parameterization (Eq. 5.4) with the parameters in Table 7.5.

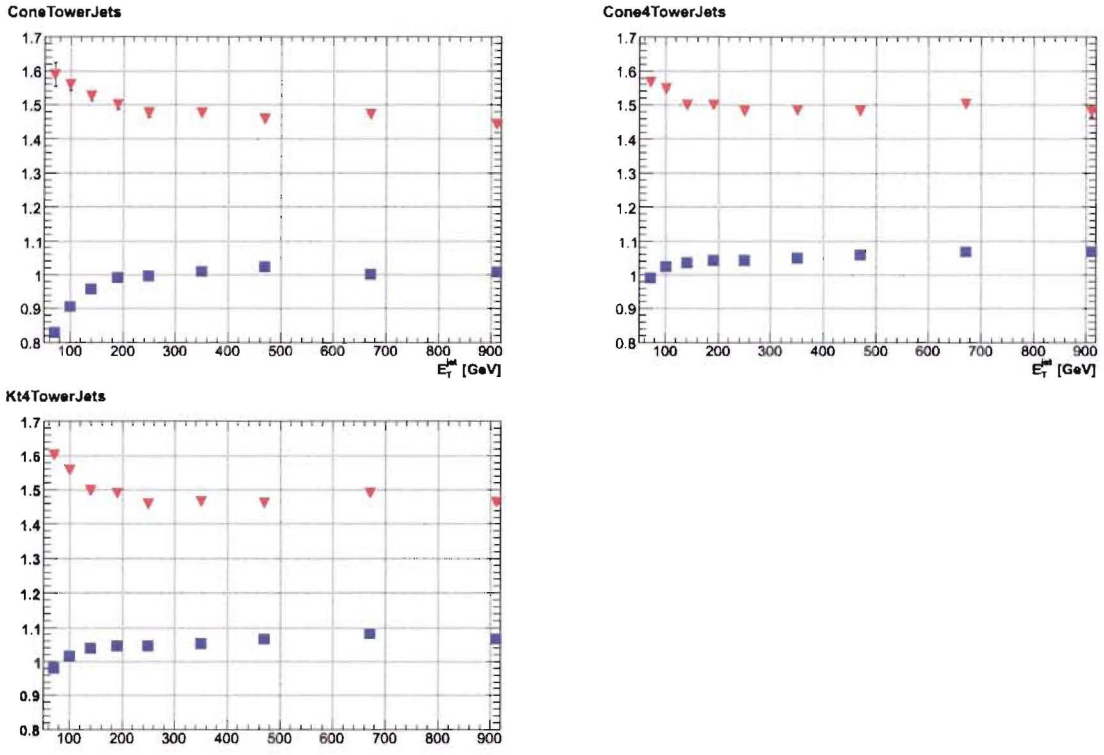

Figure 7.12: The ratios r_{calib} (squares) and r_{meas} (triangles) for `ConeTowerJets` (top left), `Cone4TowerJets` (top right), and `Kt4TowerJets` (bottom right). The points in each bin are given by the fits for the ratio r_{calib} or r_{meas}. This calibration is done using the logarithmic parameterization of the jet response. The quantity $E_T^{calib,jet}$ is calculated using the calibration parameters in Table 7.5.

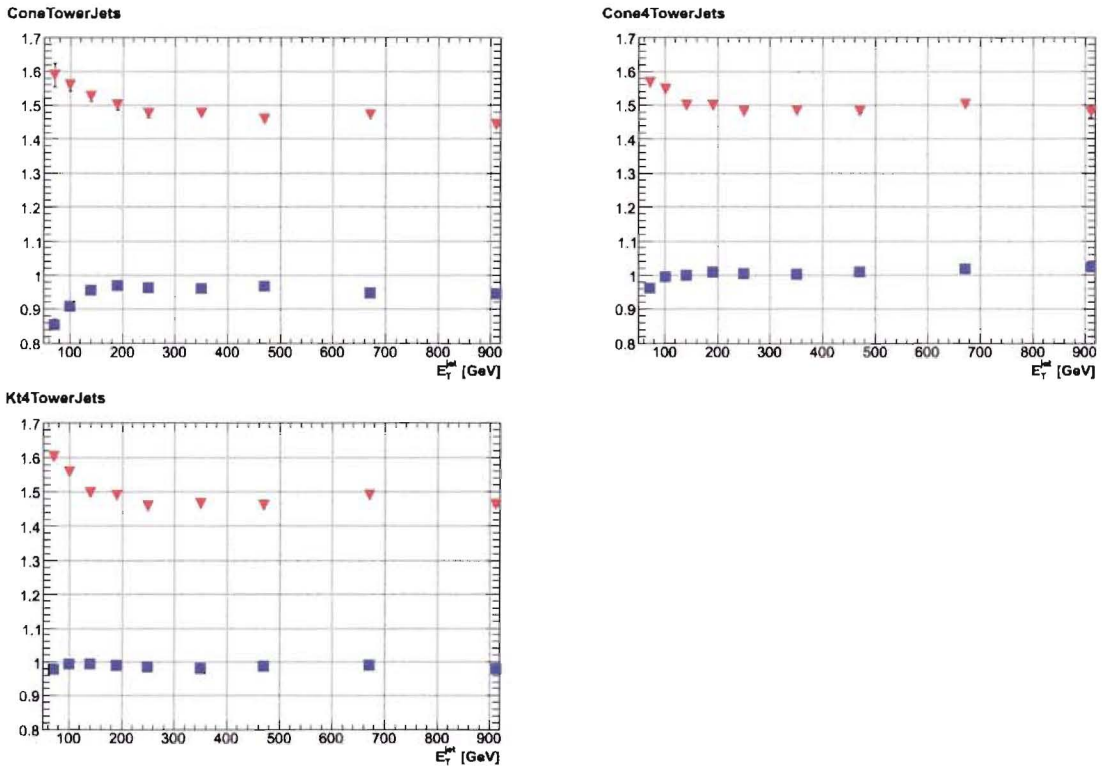

Figure 7.13: The ratios r_{calib} (squares) and r_{meas} (triangles) for `ConeTowerJets` (top left), `Cone4TowerJets` (top right), and `Kt4TowerJets` (bottom right). The points in each bin are given by the fits for the ratio r_{calib} or r_{meas}. This calibration is done using the logarithmic parameterization of the jet response. The quantity $E_T^{calib,jet}$ is calculated using the calibration parameters in Table 5.8.

Chapter 8

Conclusions

A precise knowledge of the jet energy scale is essential to the ATLAS physics programme. In this thesis, the utility of the $\not\!\!E_T$ projection fraction method in determining the jet response portion of the overall scale has been shown. Some of the negative effects that the additional minimum bias events have on the overall resolution and energy scale of the various calorimeter subsystems have also been shown. The measurement of the jet response in situ was shown to be biased due to the presence of pileup, but the energy scale of cone and k_T jets constructed from calorimeter towers remains effectively unchanged.

However, further study is required to understand how the local hadronic calibration depends on the level of pileup activity. Only overall jet corrections have been addressed in this thesis. Also, to limit the effects of limited statistics, much larger γ + jet datasets are required for detailed pileup studies. New, large scale productions of simulated ATLAS data which are currently underway should be useful in this regard.

The coming two years will no doubt bring a whole host of surprises as the ATLAS collaboration shifts from making predictions with simulated data to making actual measurements with the detector. The amount of work that needs to be done to fully understand the intricacies of the physics and the detector seems almost insurmountable, but we remain confident that research on ATLAS in the coming years will be very fruitful to our understanding of the basic construction of the universe.

Appendix A

Pileup Distributions

This appendix details the expected levels of pileup noise in each of the calorimeter subsystems as a function of the radius of a cone centered at some typical point in the detector.

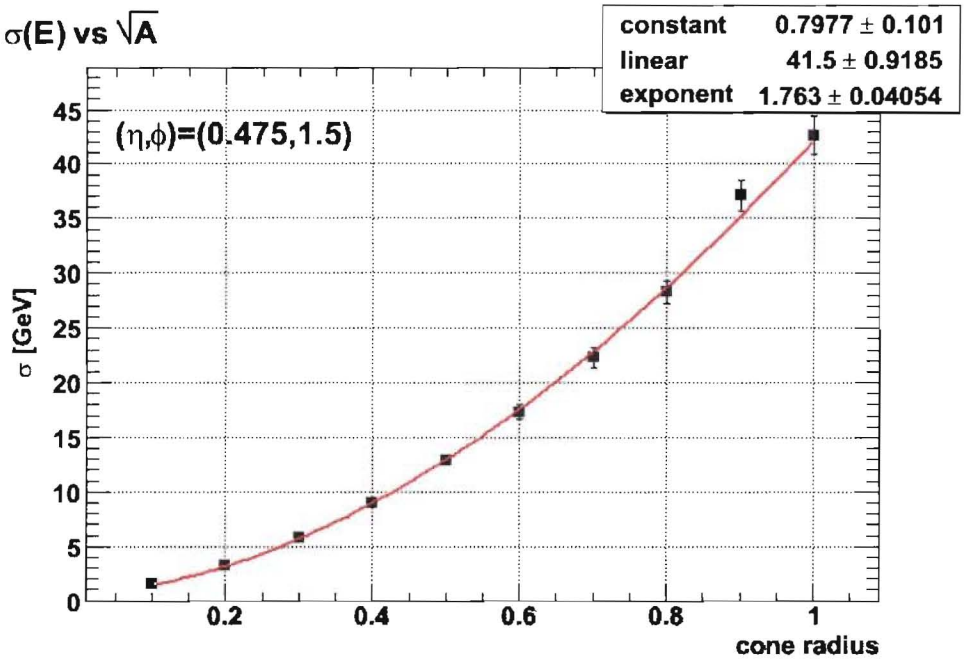

Figure A.1: Pileup $\sigma(E)$ at 1/2 design luminosity (11.5 minimum bias collisions per bunch crossing) versus ΔR in the EM barrel calorimeter. The calculation considers only energy deposition in the EM barrel calorimeter inside cones centered at $(\eta, \phi) = (0.475, 1.5)$. Events were generated using the parameters listed in Table 6.1. Curves are fitted to the form $f(\Delta R) = a + b\,(\Delta R)^c$.

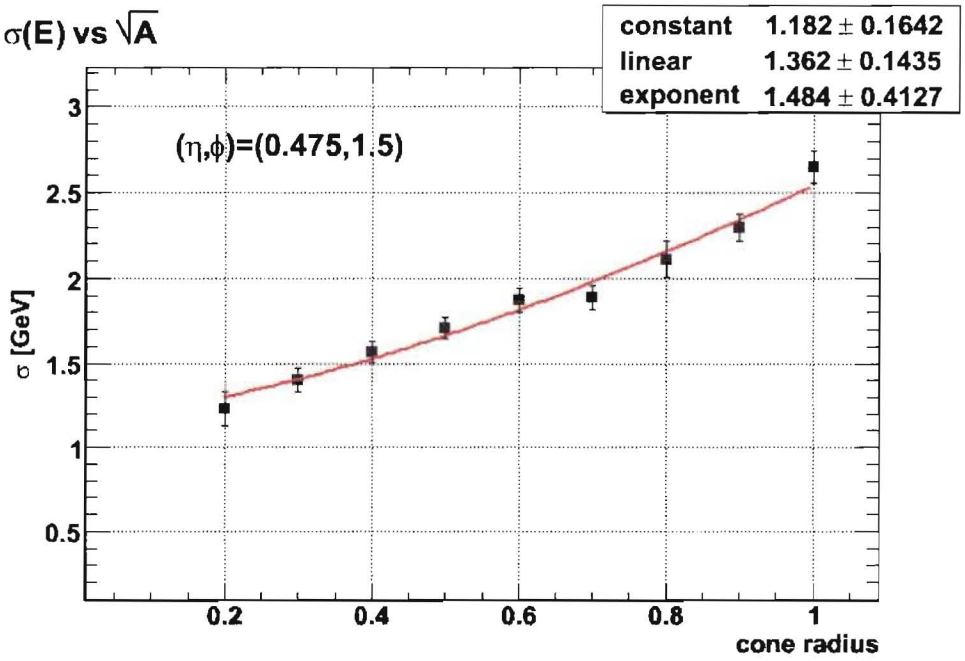

Figure A.2: Pileup $\sigma(E)$ at 1/2 design luminosity versus ΔR inside cones in the TILE calorimeter entered at $(\eta, \phi) = (0.475, 1.5)$.

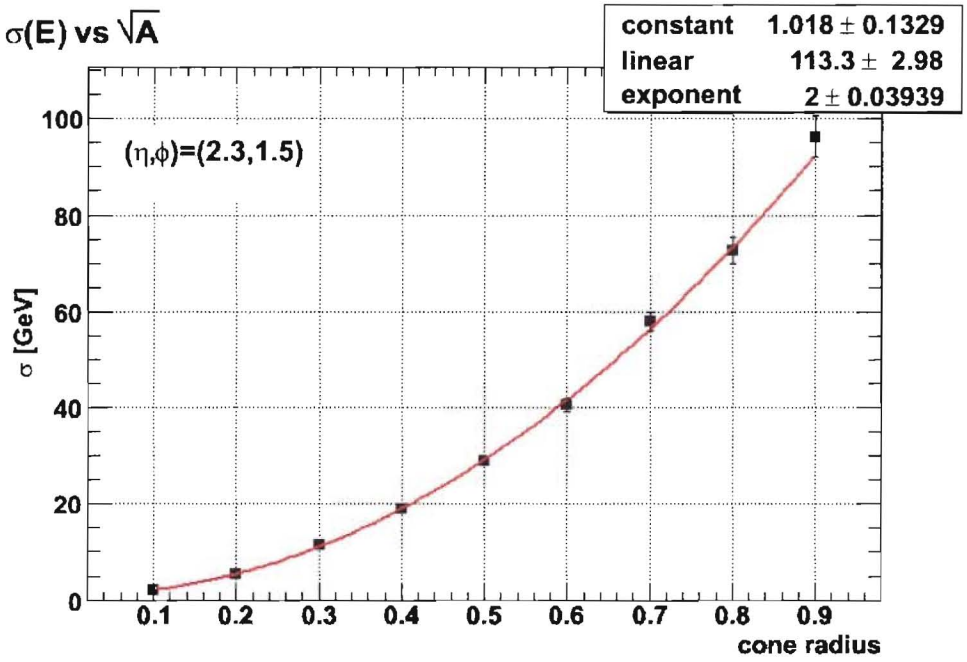

Figure A.3: Pileup $\sigma(E)$ at 1/2 design luminosity versus ΔR inside cones in the EMEC centered at $(\eta, \phi) = (2.3, 1.5)$.

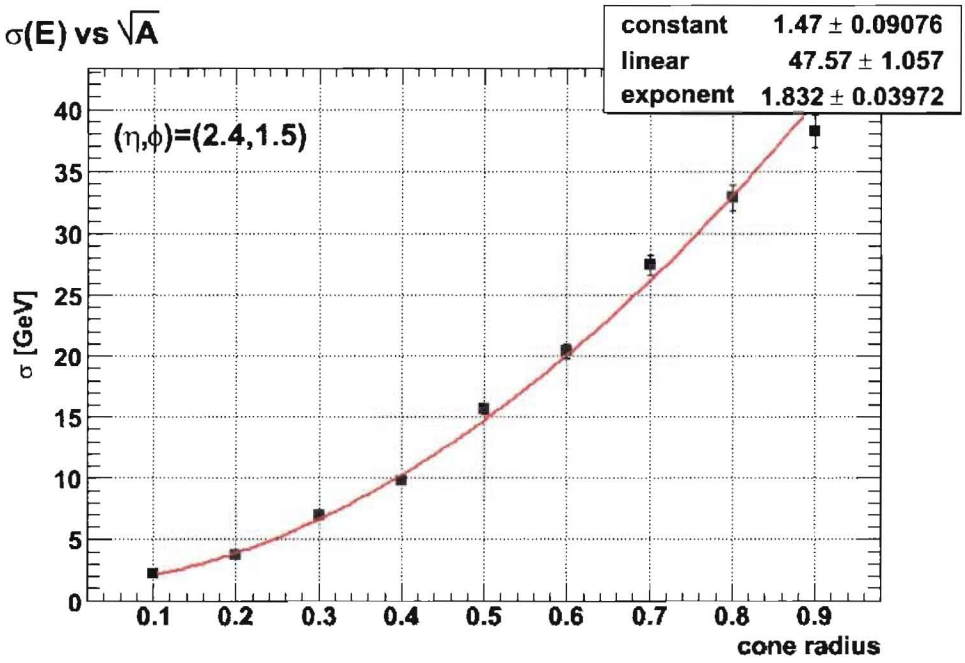

Figure A.4: Pileup $\sigma(E)$ at 1/2 design luminosity versus ΔR inside cones in the HEC centered at $(\eta, \phi) = (2.4, 1.5)$.

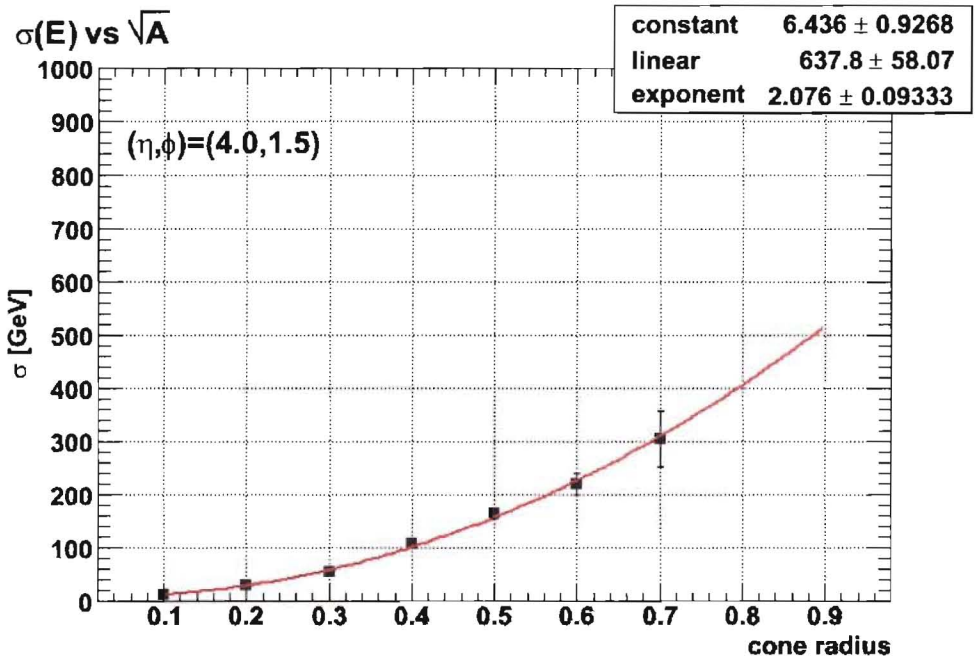

Figure A.5: Pileup $\sigma(E)$ at 1/2 design luminosity versus ΔR inside cones in the FCAL centered at $(\eta, \phi) = (4.0, 1.5)$.

Appendix B

Jet Response Distributions

This appendix contains the fit results for the jet response and jet energy in each of the eleven E' bins E' = {25.0 GeV, 40.0 GeV, 65.0 GeV, 85.0 GeV, 120.0 GeV, 160.0 GeV, 190.0 GeV, 250.0 GeV, 350.0 GeV, 490.0 GeV, 670.0 GeV, 910.0 GeV}. These measurements were performed on the data consisting of γ + jet events without additional minimum bias interactions.

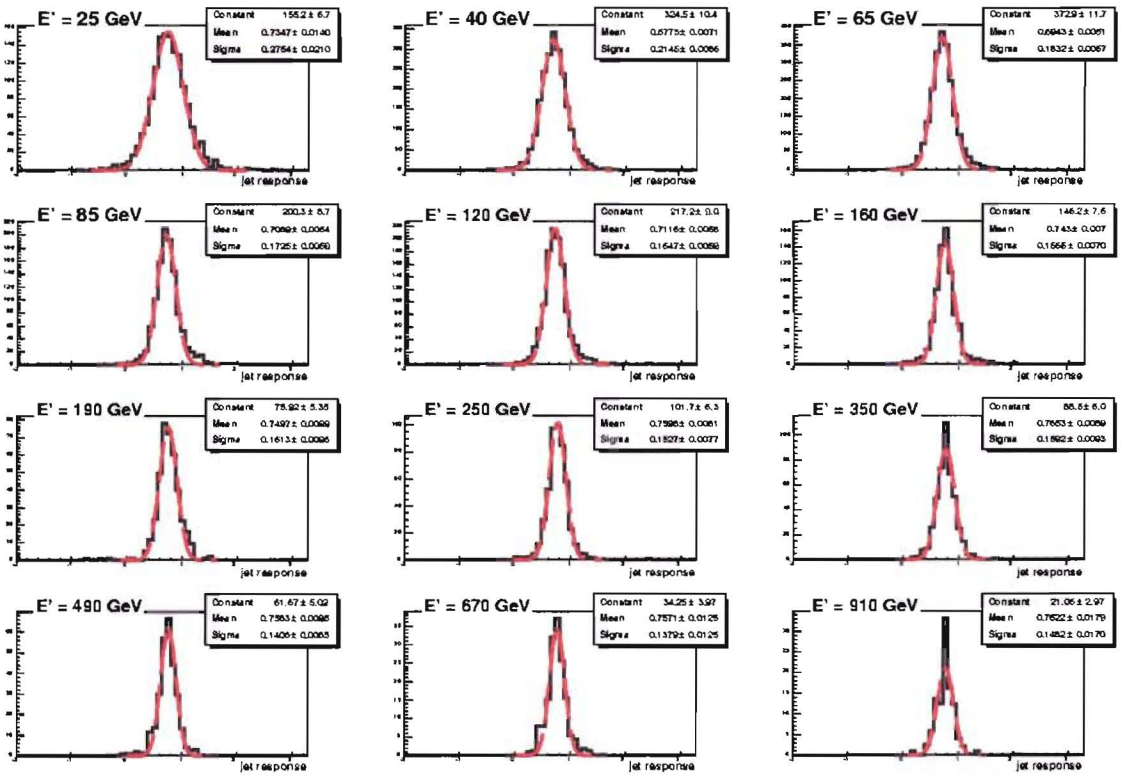

Figure B.1: Distributions of the jet response in the eleven E' bins for `Cone4TowerJets`. The fit results are shown for each E' bin for a Gaussian fit.

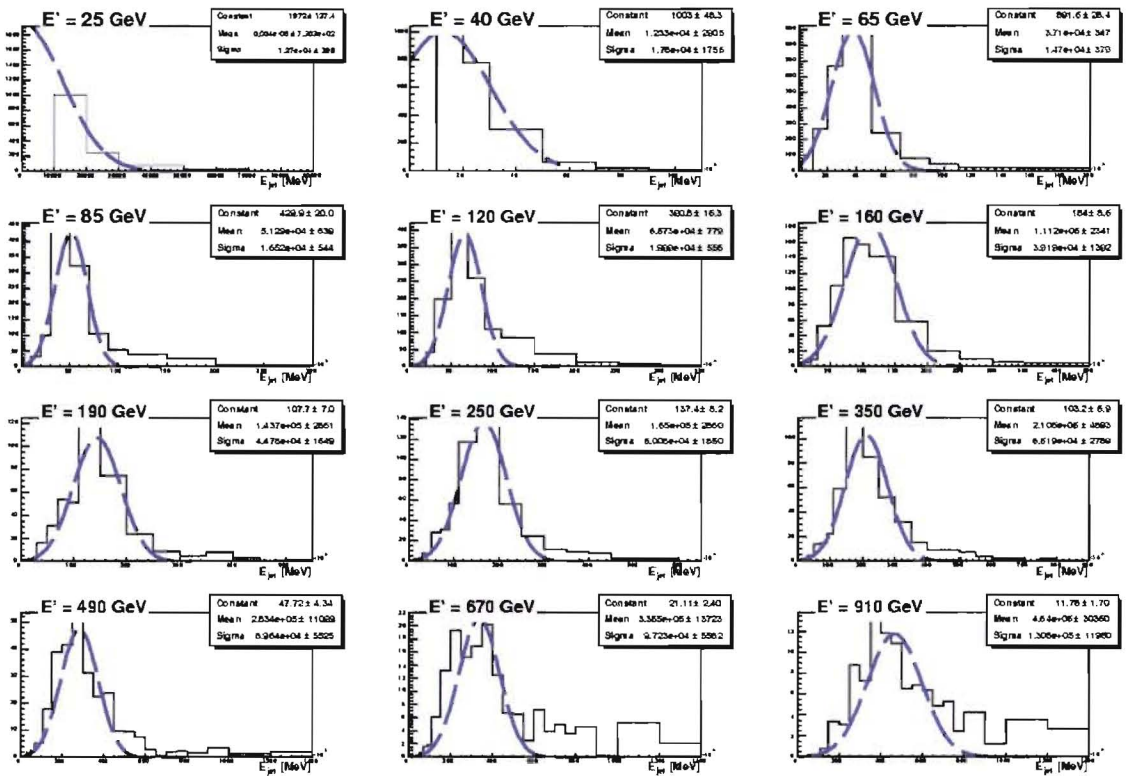

Figure B.2: Distributions of the jet energy in the eleven E' bins for `Cone4TowerJets`. The fit results are shown for each E' bin for a Gaussian fit; however, only the mean of the distribution is used in plotting j versus $E^{meas,jet}$.

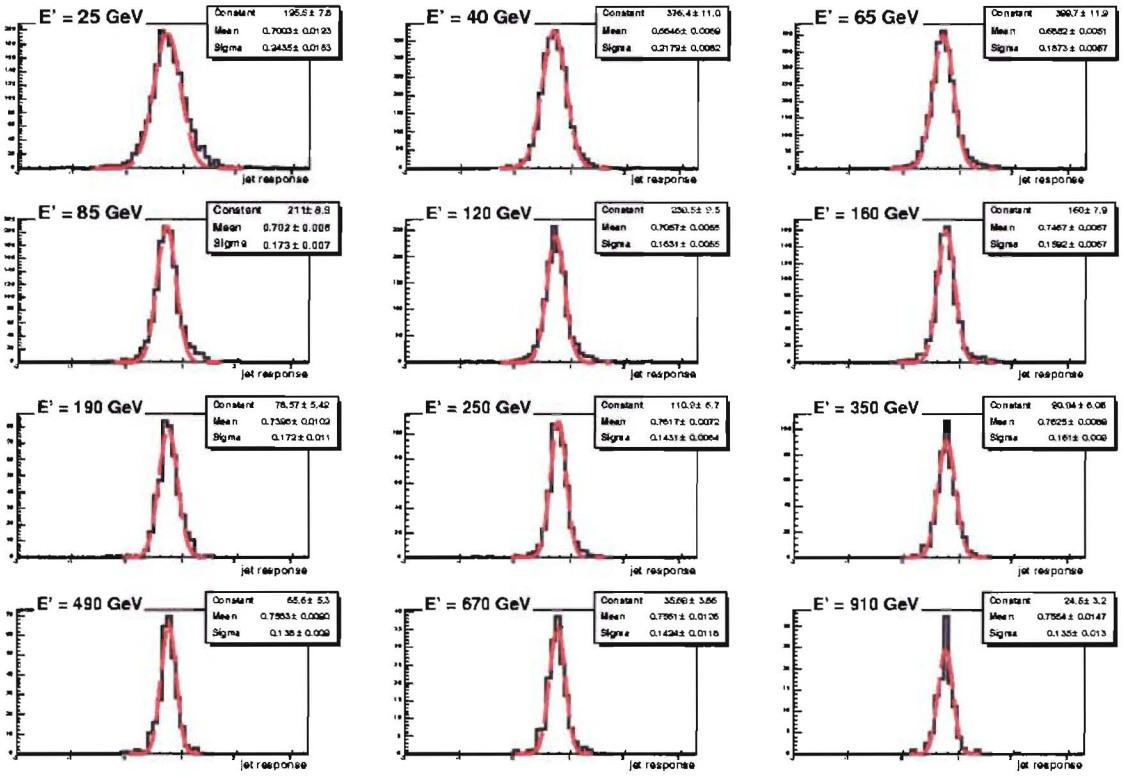

Figure B.3: Distributions of the jet response in the eleven E' bins for `ConeTowerJets`. The fit results are shown for each E' bin for a Gaussian fit.

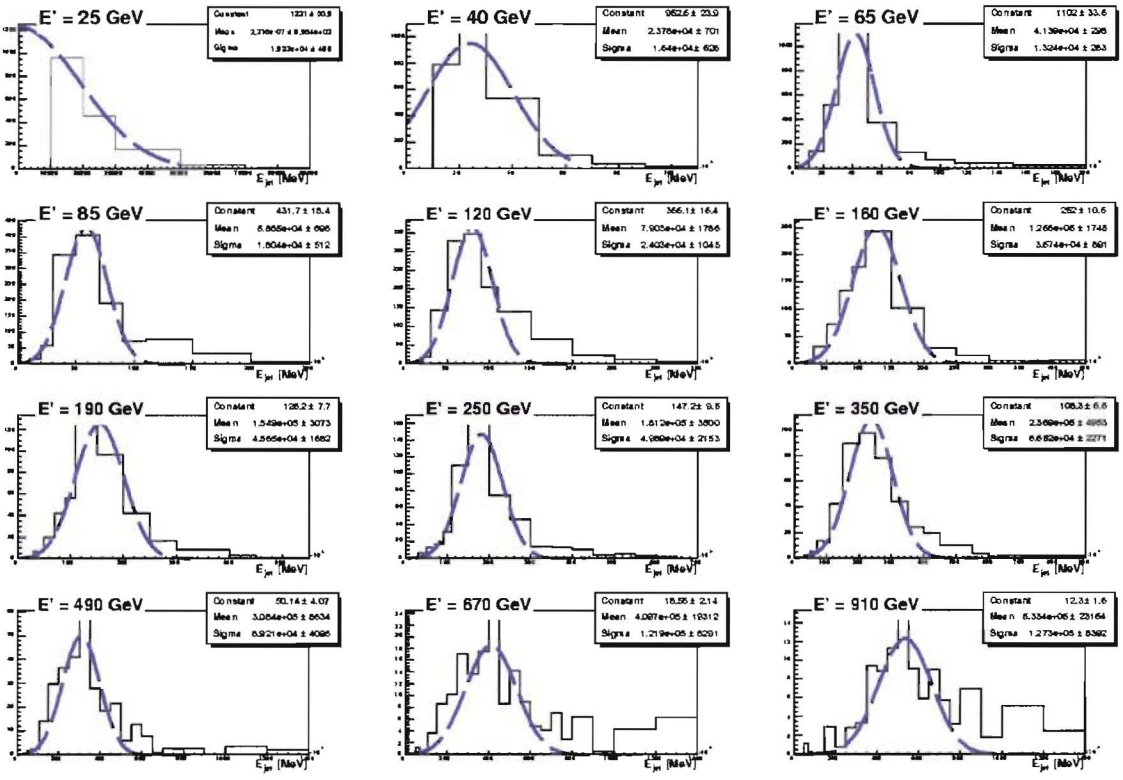

Figure B.4: Distributions of the jet energy in the eleven E' bins for `ConeTowerJets`. The fit results are shown for each E' bin for a Gaussian fit; however, only the mean of the distribution is used in plotting j versus $E^{meas,jet}$.

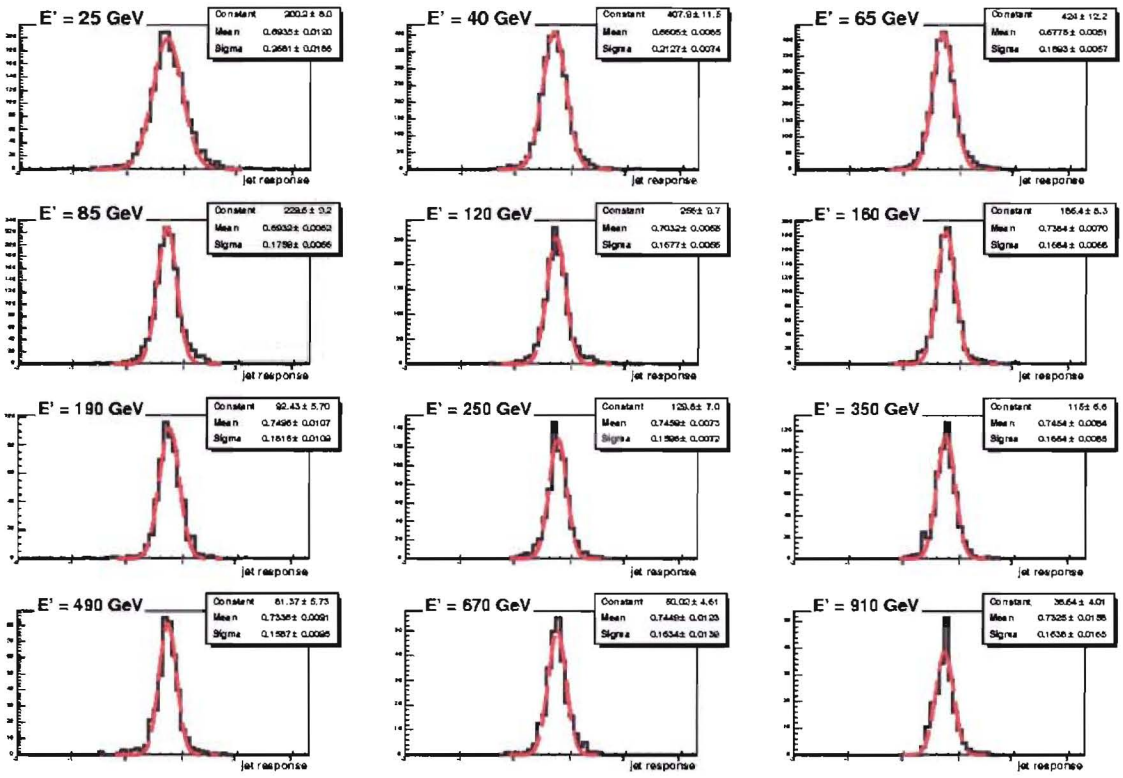

Figure B.5: Distributions of the jet response in the eleven E' bins for `ConeClusterJets`. The fit results are shown for each E' bin for a Gaussian fit.

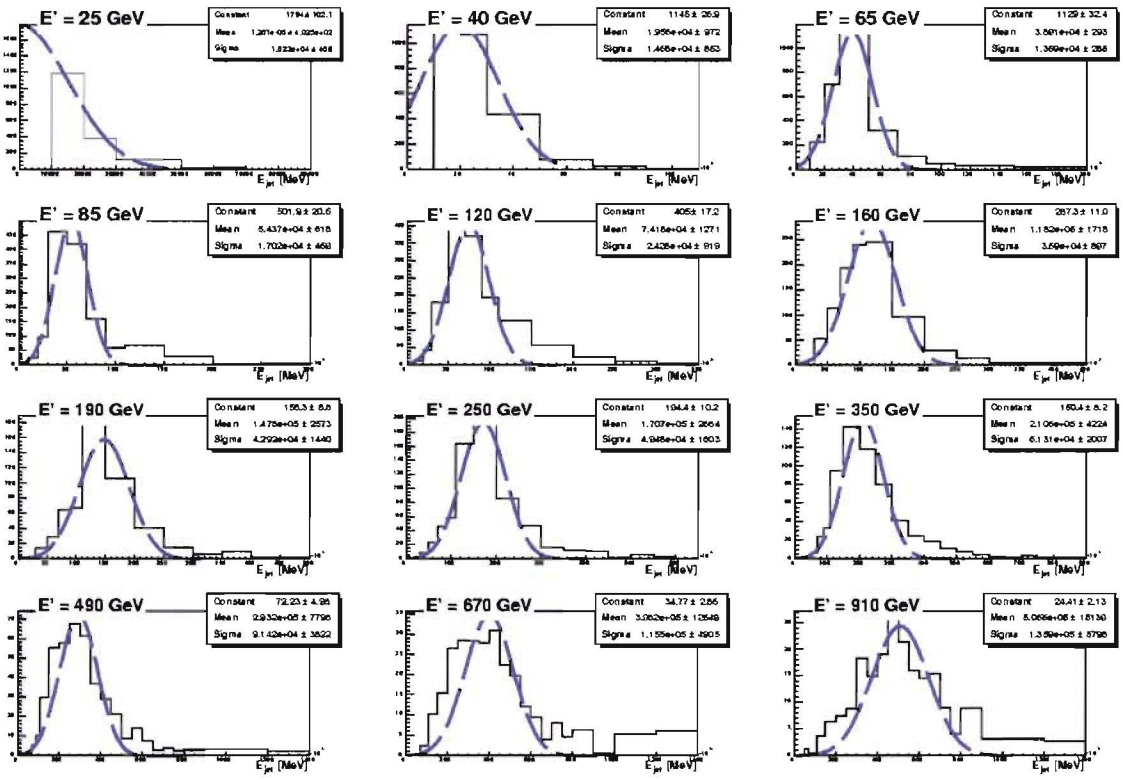

Figure B.6: Distributions of the jet energy in the eleven E' bins for `ConeClusterJets`. The fit results are shown for each E' bin for a Gaussian fit; however, only the mean of the distribution is used in plotting j versus $E^{meas,jet}$.

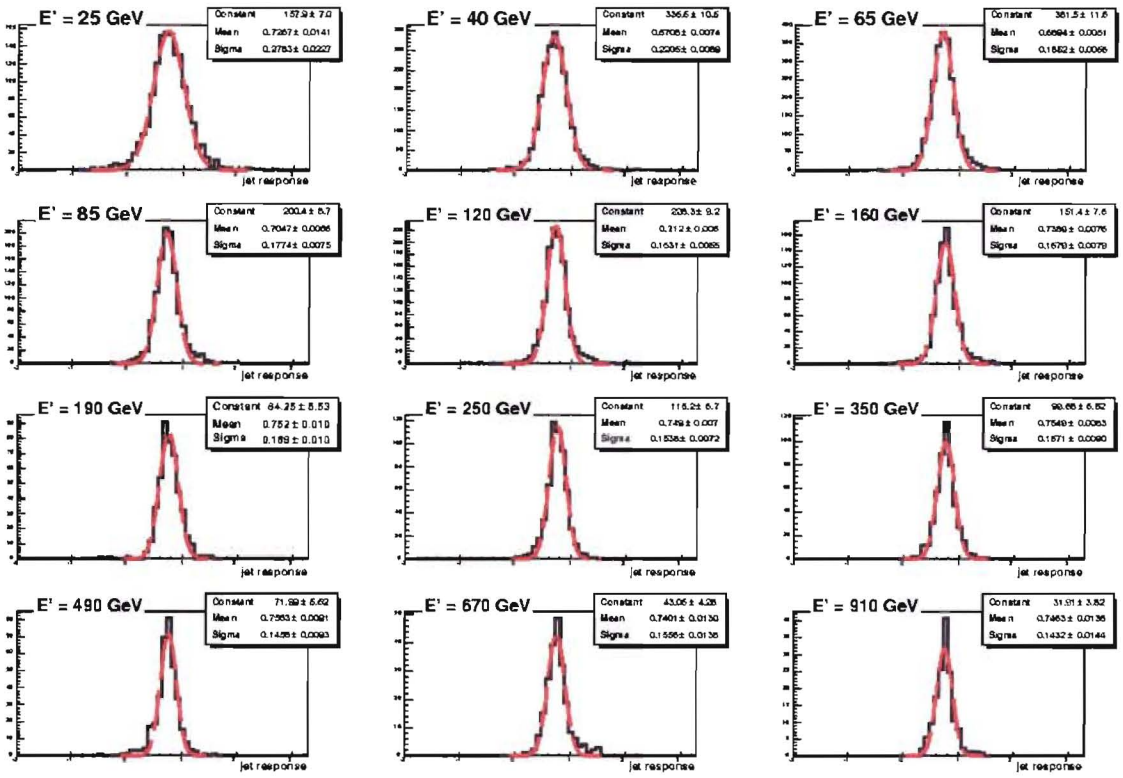

Figure B.7: Distributions of the jet response in the eleven E' bins for `Kt4TowerJets`. The fit results are shown for each E' bin for a Gaussian fit.

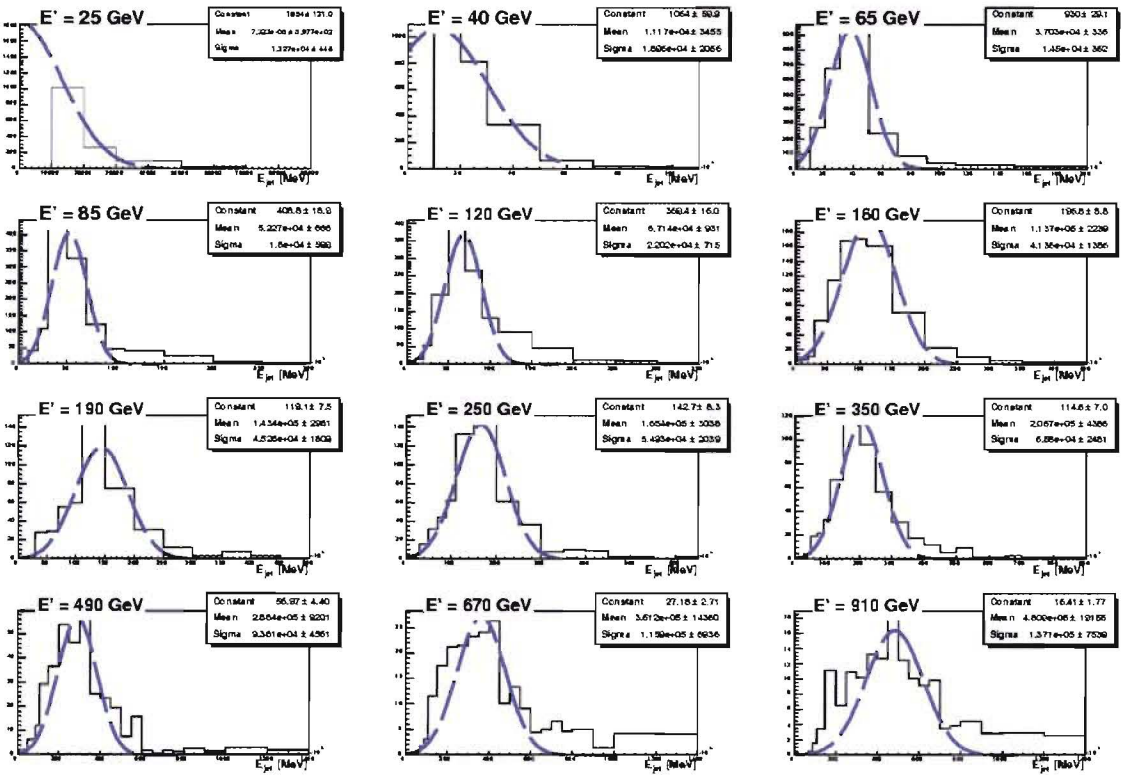

Figure B.8: Distributions of the jet energy in the eleven E' bins for `Kt4TowerJets`. The fit results are shown for each E' bin for a Gaussian fit; however, only the mean of the distribution is used in plotting j versus $E^{meas,jet}$.

Appendix C

Jet Response Distributions

This appendix contains the fit results for the jet response and jet energy in each of the eleven E' bins E' = {25.0 GeV, 40.0 GeV, 65.0 GeV, 85.0 GeV, 120.0 GeV, 160.0 GeV, 190.0 GeV, 250.0 GeV, 350.0 GeV, 490.0 GeV, 670.0 GeV, 910.0 GeV}. These measurements were performed on the Lumi02 data.

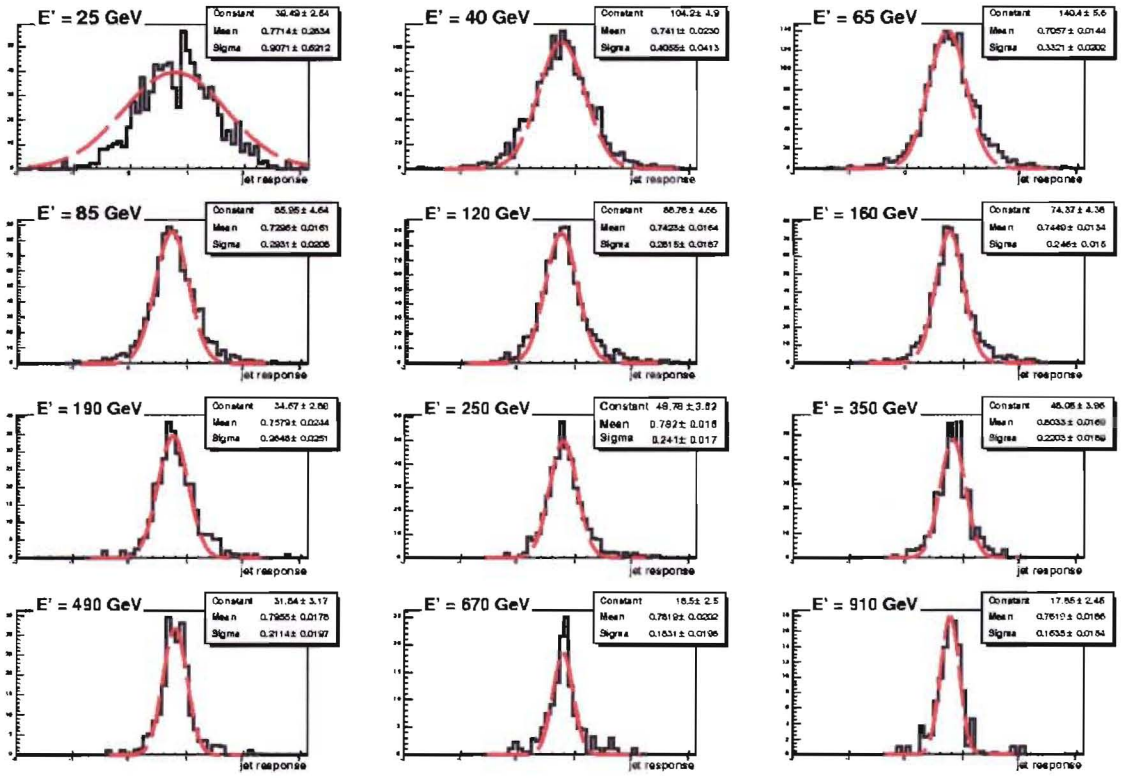

Figure C.1: Distributions of the jet response in the eleven E' bins for `Cone4TowerJets` from the `Lumi02` data. The fit results are shown for each E' bin for a Gaussian fit.

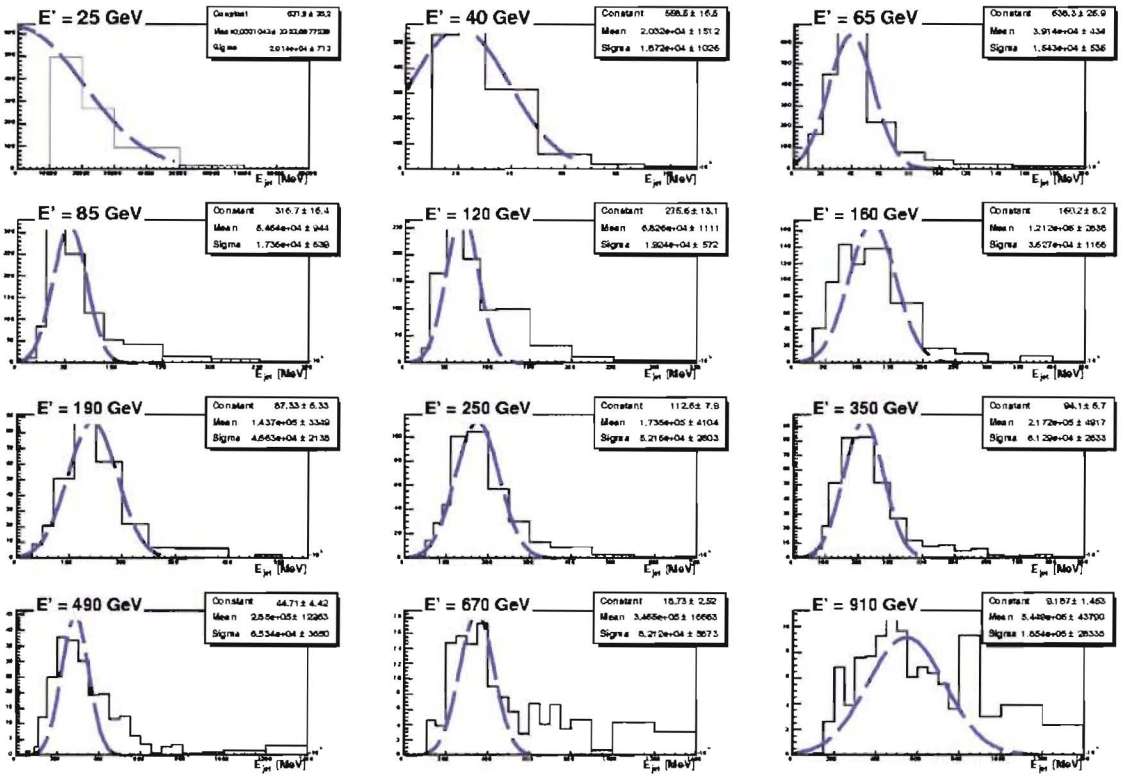

Figure C.2: Distributions of the jet energy in the eleven E' bins for `Cone4TowerJets` from the `Lumi02` data. The fit results are shown for each E' bin for a Gaussian fit; however, only the mean of the distribution is used in plotting j versus $E^{meas,jet}$.

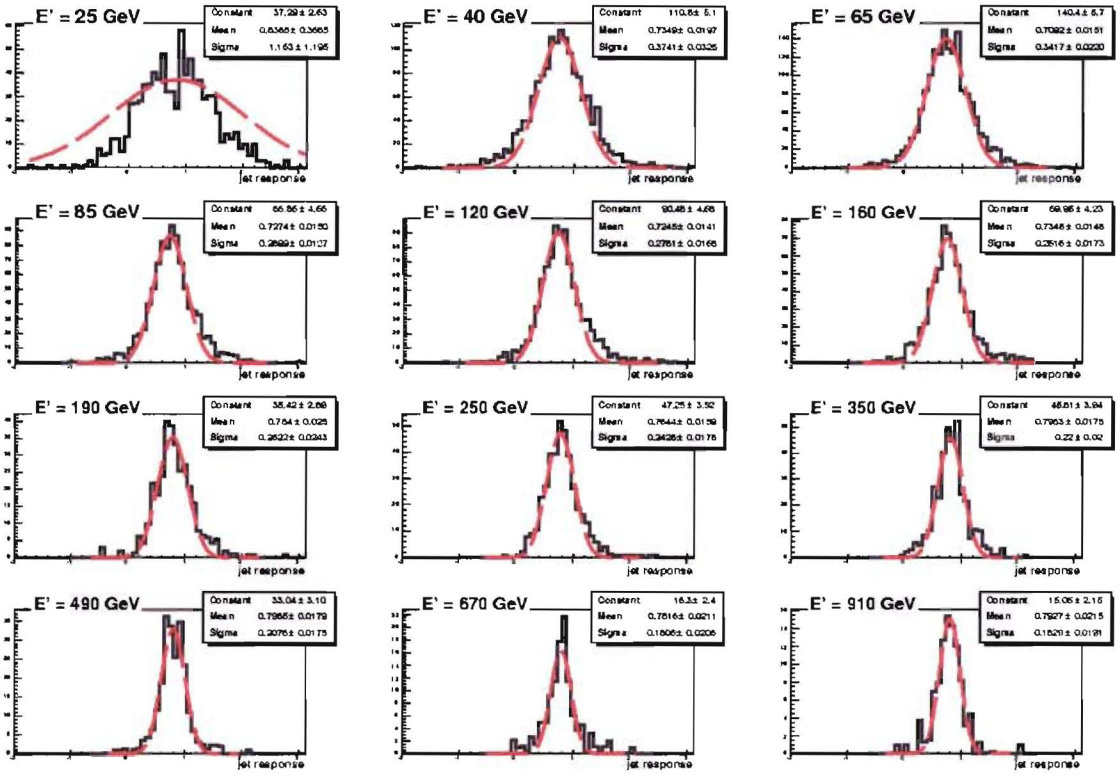

Figure C.3: Distributions of the jet response in the eleven E' bins for `ConeTowerJets` from the `Lumi02` data. The fit results are shown for each E' bin for a Gaussian fit.

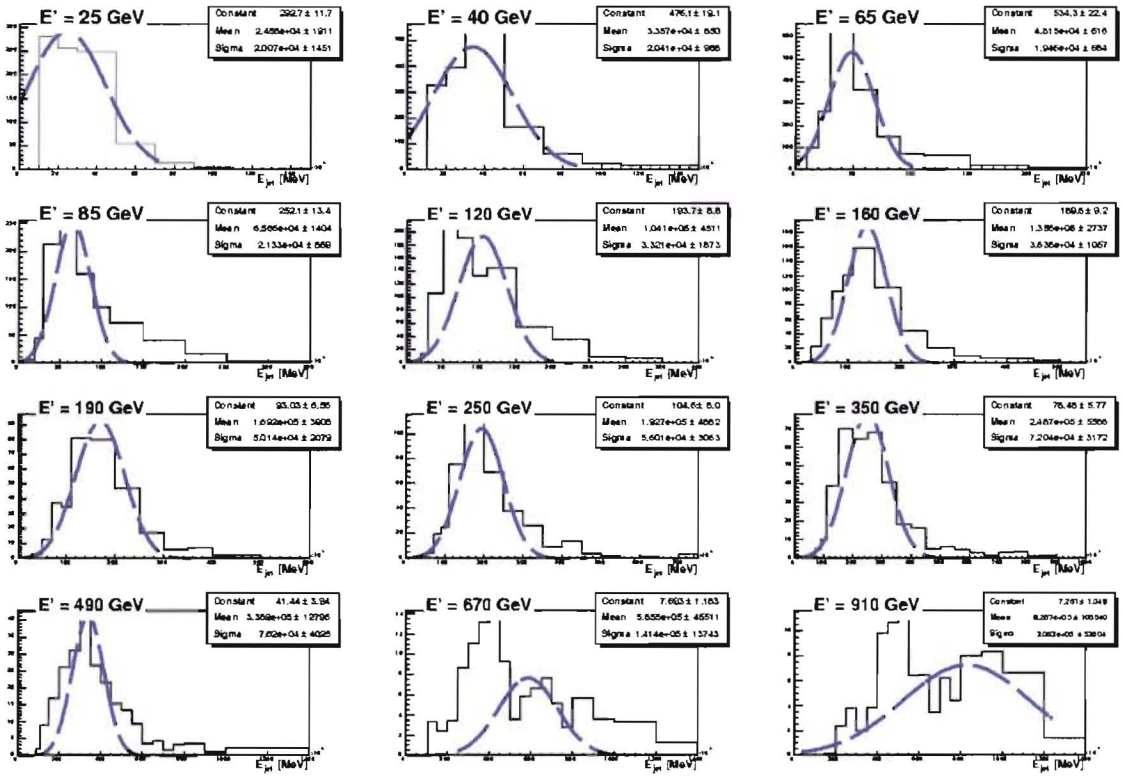

Figure C.4: Distributions of the jet energy in the eleven E' bins for `ConeTowerJets` from the `Lumi02` data. The fit results are shown for each E' bin for a Gaussian fit; however, only the mean of the distribution is used in plotting j versus $E^{meas,jet}$.

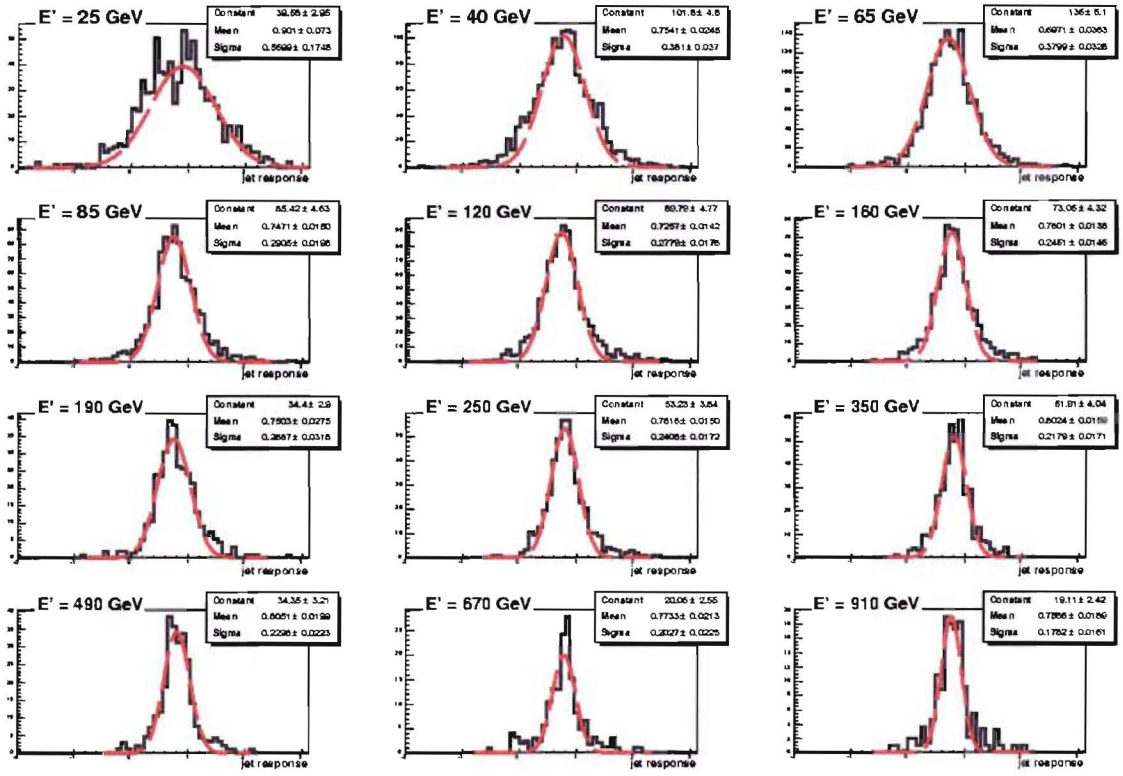

Figure C.5: Distributions of the jet response in the eleven E' bins for `Kt4TowerJets` from the `Lumi02` data. The fit results are shown for each E' bin for a Gaussian fit.

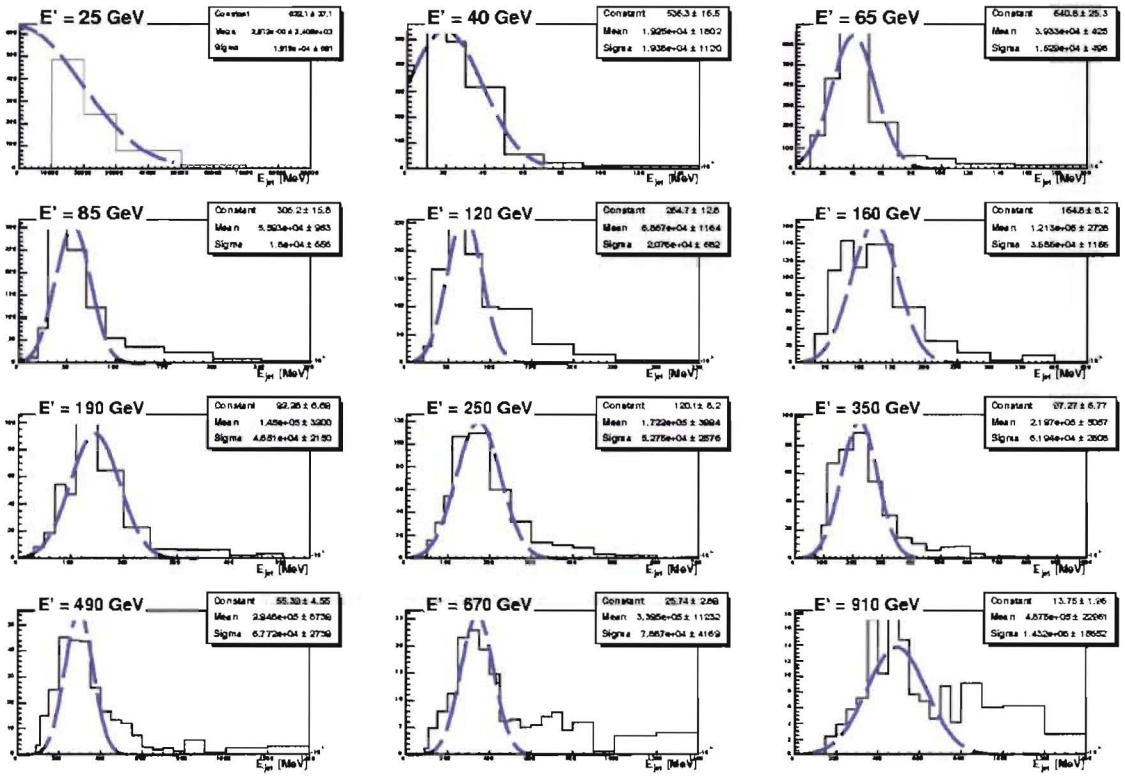

Figure C.6: Distributions of the jet energy in the eleven E' bins for `Kt4TowerJets` from the `Lumi02` data. The fit results are shown for each E' bin for a Gaussian fit; however, only the mean of the distribution is used in plotting j versus $E^{meas,jet}$.

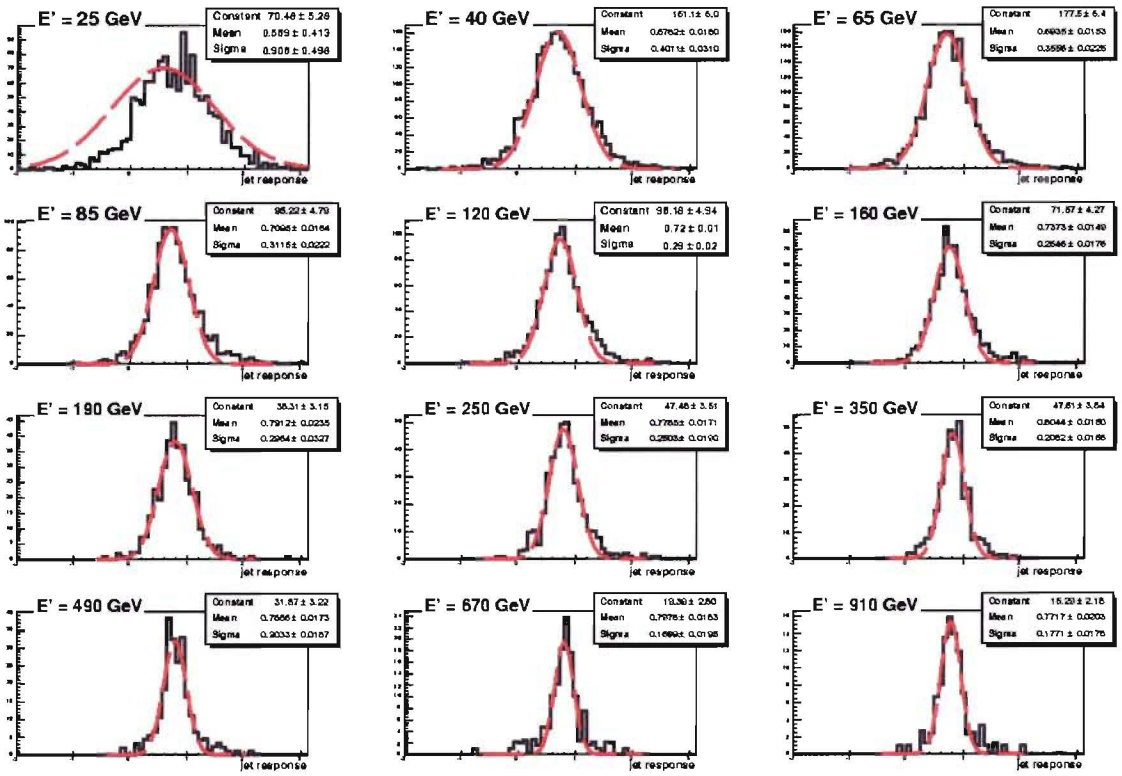

Figure C.7: Distributions of the jet response in the eleven E' bins for `ConeClusterJets` from the `Lumi02` data. The fit results are shown for each E' bin for a Gaussian fit.

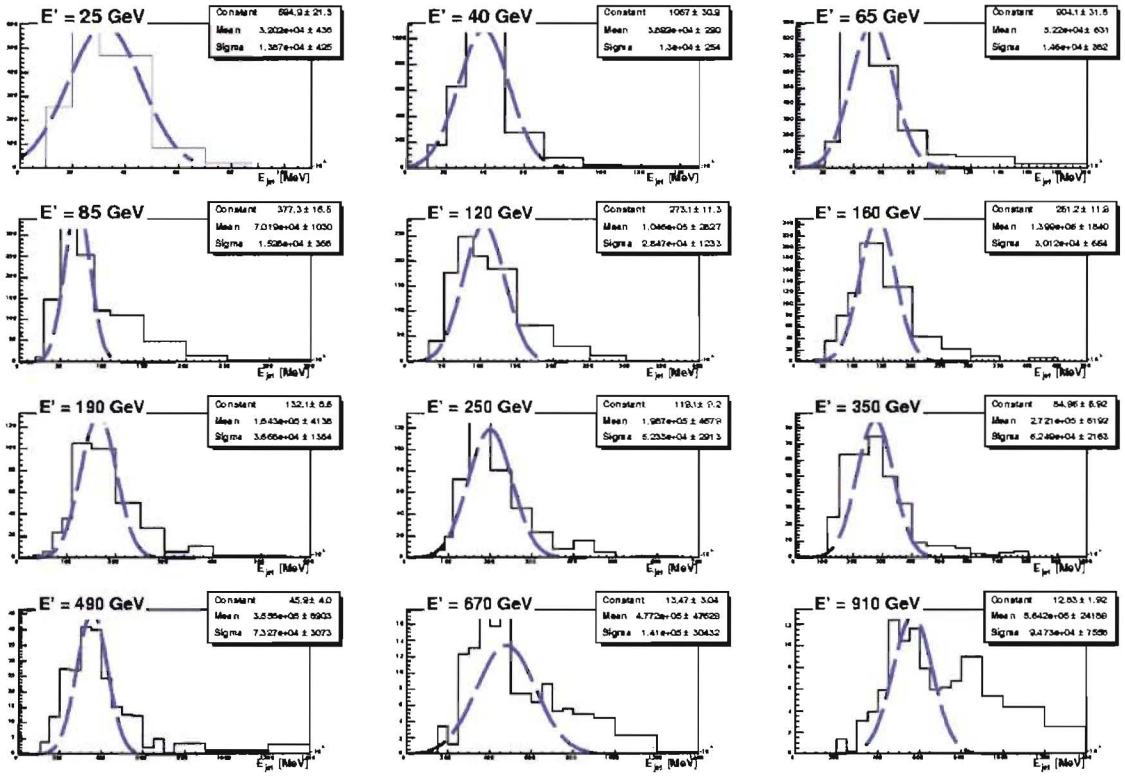

Figure C.8: Distributions of the jet energy in the eleven E' bins for `ConeClusterJets` from the `Lumi02` data. The fit results are shown for each E' bin for a Gaussian fit; however, only the mean of the distribution is used in plotting j versus $E^{meas,jet}$.

Appendix D

Jet Response Distributions

This appendix contains the fit results for the jet response and jet energy in each of the eleven E' bins `E' = {25.0 GeV, 40.0 GeV, 65.0 GeV, 85.0 GeV, 120.0 GeV, 160.0 GeV, 190.0 GeV, 250.0 GeV, 350.0 GeV, 490.0 GeV, 670.0 GeV, 910.0 GeV}`. These measurements were performed on the `Lumi05` data.

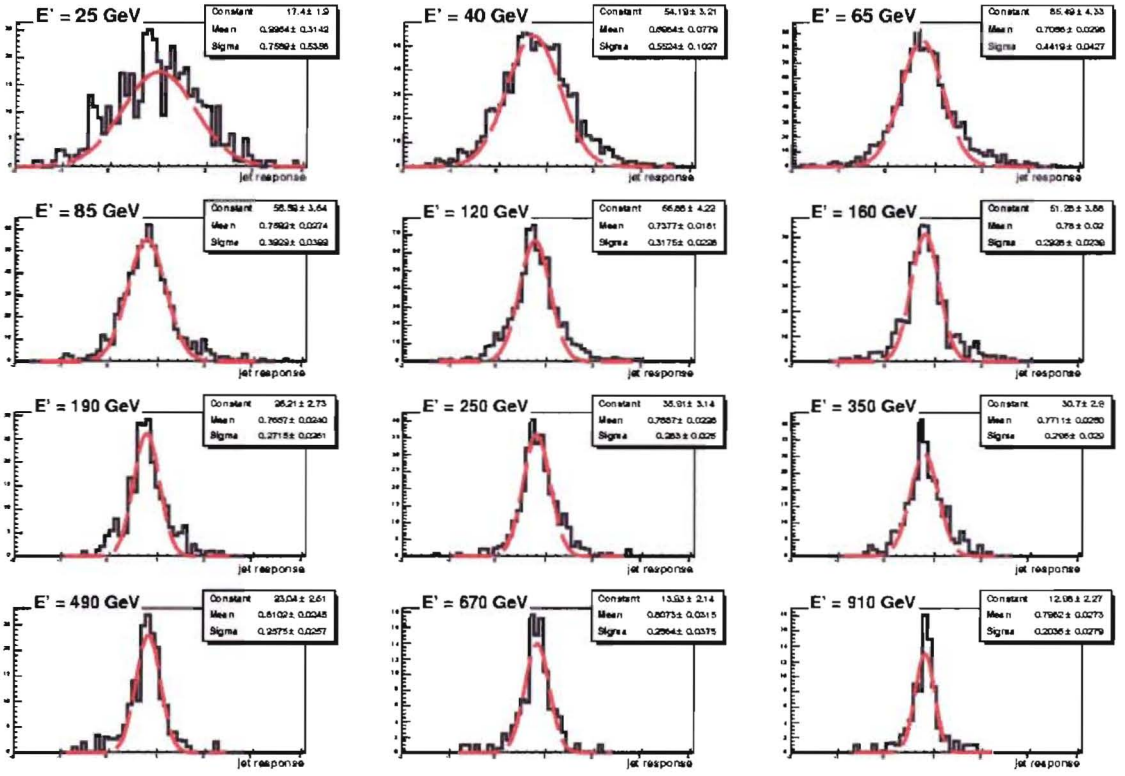

Figure D.1: Distributions of the jet response in the eleven E' bins for `Cone4TowerJets` from the `Lumi05` data. The fit results are shown for each E' bin for a Gaussian fit.

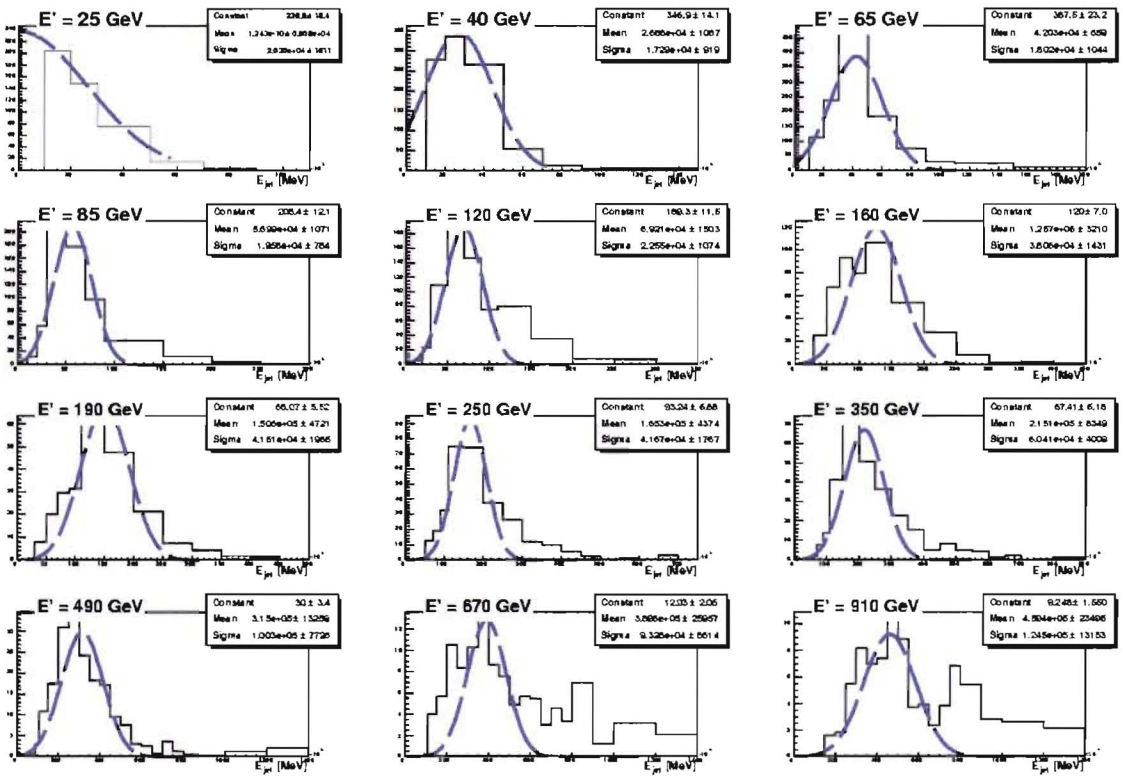

Figure D.2: Distributions of the jet energy in the eleven E' bins for `Cone4TowerJets` from the `Lumi05` data. The fit results are shown for each E' bin for a Gaussian fit; however, only the mean of the distribution is used in plotting j versus $E^{meas,jet}$.

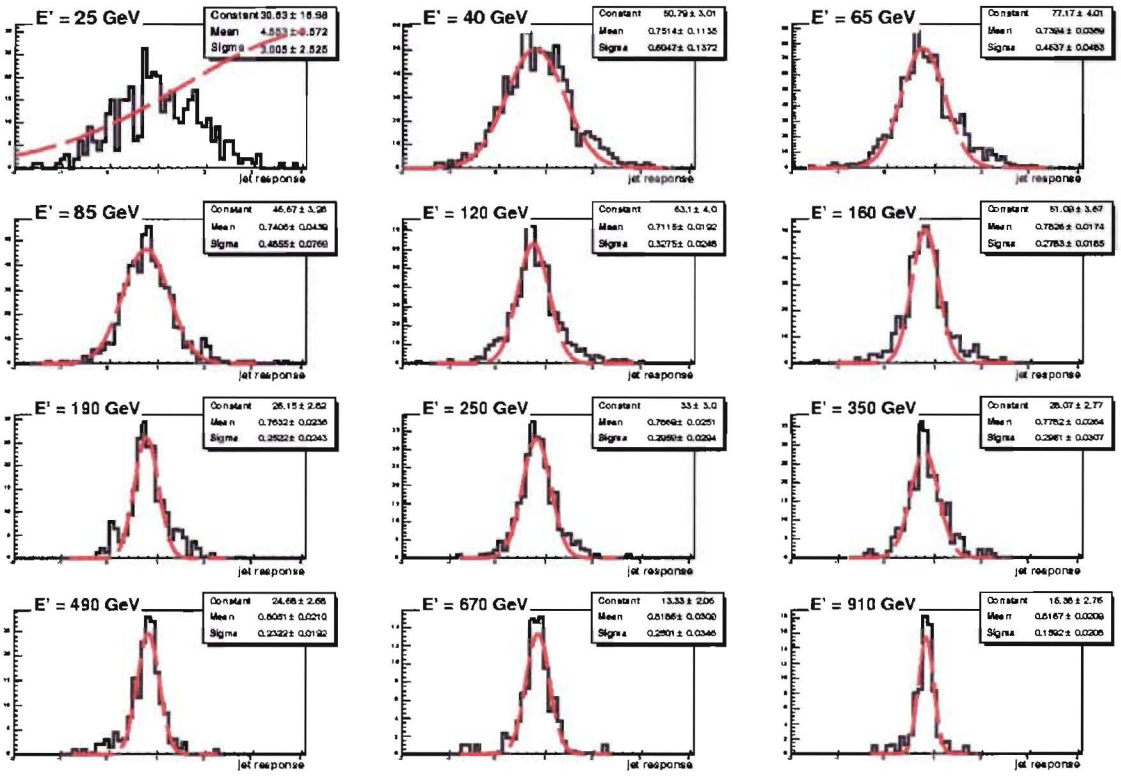

Figure D.3: Distributions of the jet response in the eleven E' bins for `ConeTowerJets` from the `Lumi05` data. The fit results are shown for each E' bin for a Gaussian fit.

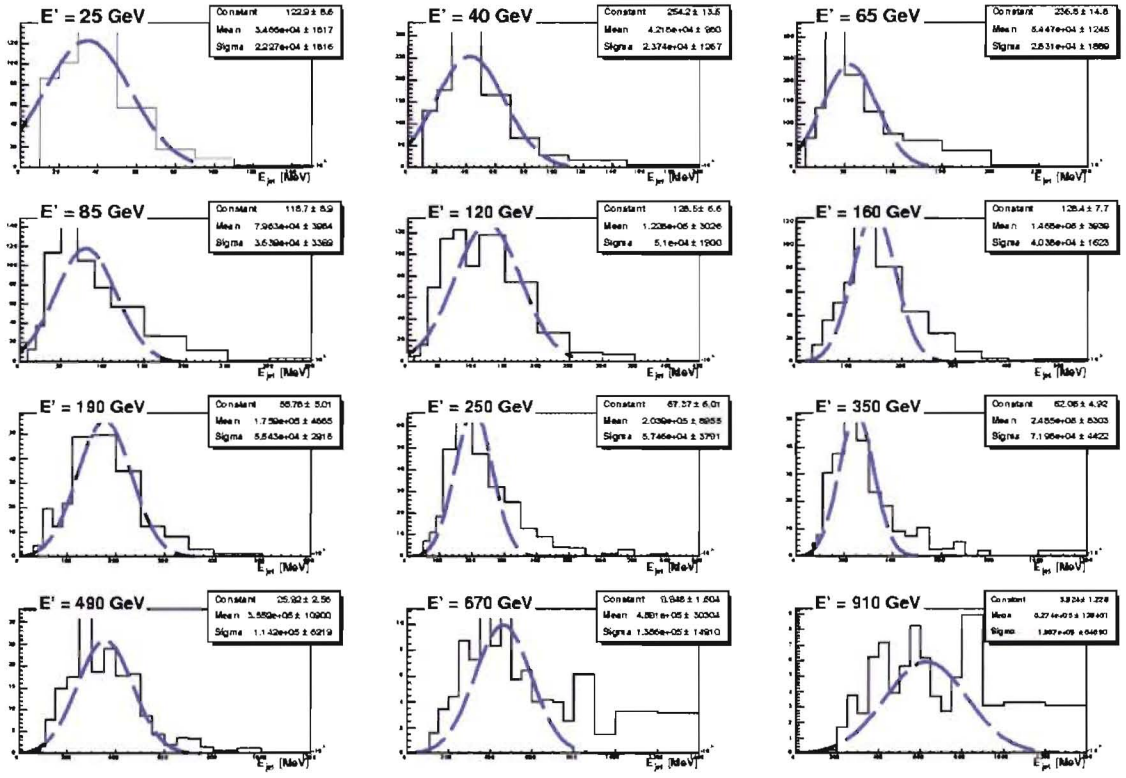

Figure D.4: Distributions of the jet energy in the eleven E' bins for `ConeTowerJets` from the `Lumi05` data. The fit results are shown for each E' bin for a Gaussian fit; however, only the mean of the distribution is used in plotting j versus $E^{meas,jet}$.

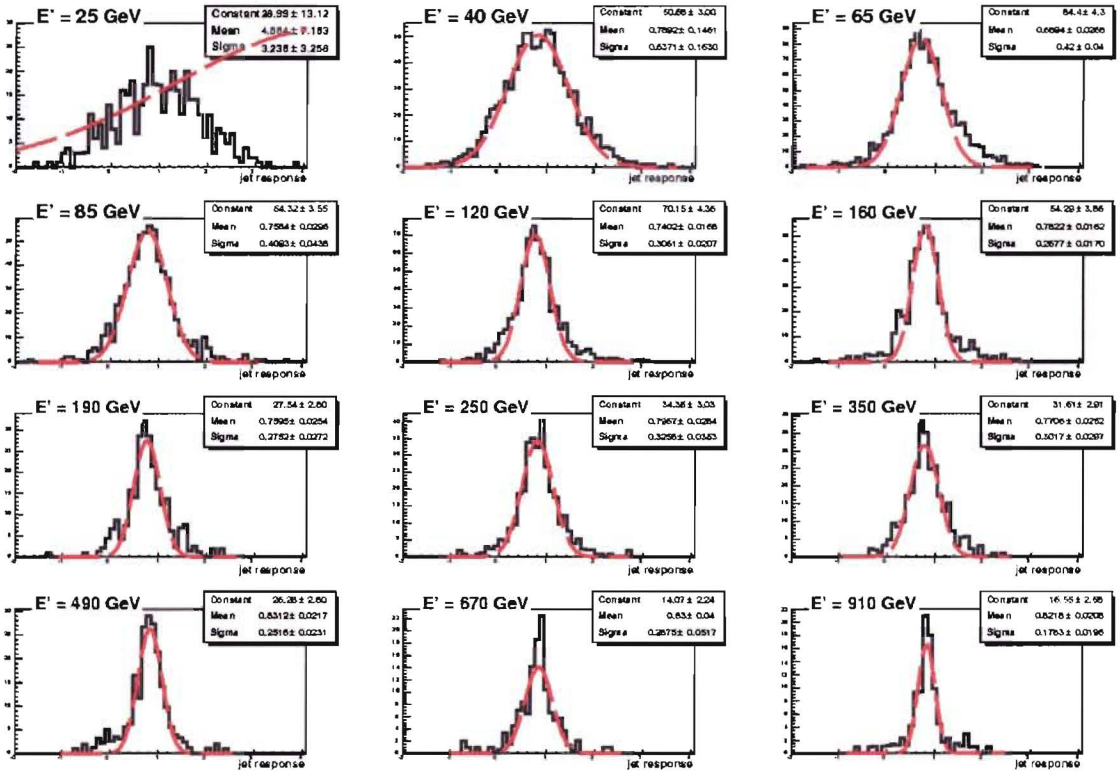

Figure D.5: Distributions of the jet response in the eleven E' bins for `Kt4TowerJets` from the `Lumi05` data. The fit results are shown for each E' bin for a Gaussian fit.

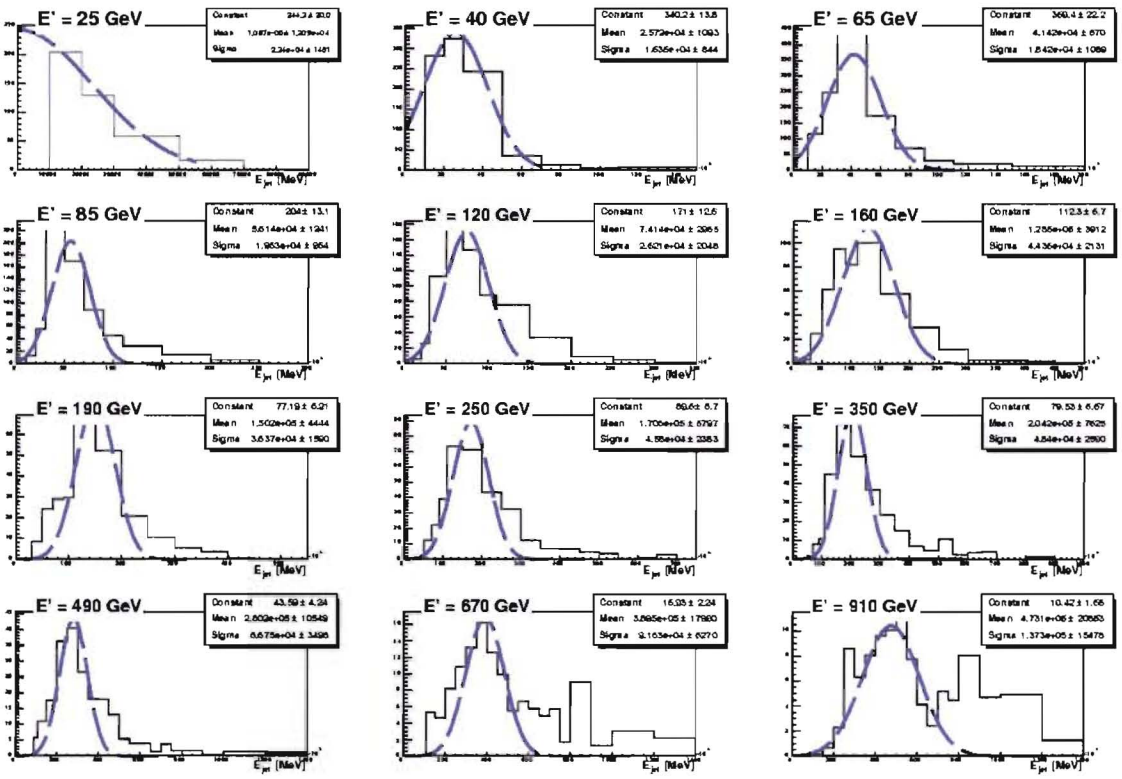

Figure D.6: Distributions of the jet energy in the eleven E' bins for `Kt4TowerJets` from the `Lumi05` data. The fit results are shown for each E' bin for a Gaussian fit; however, only the mean of the distribution is used in plotting j versus $E^{meas,jet}$.

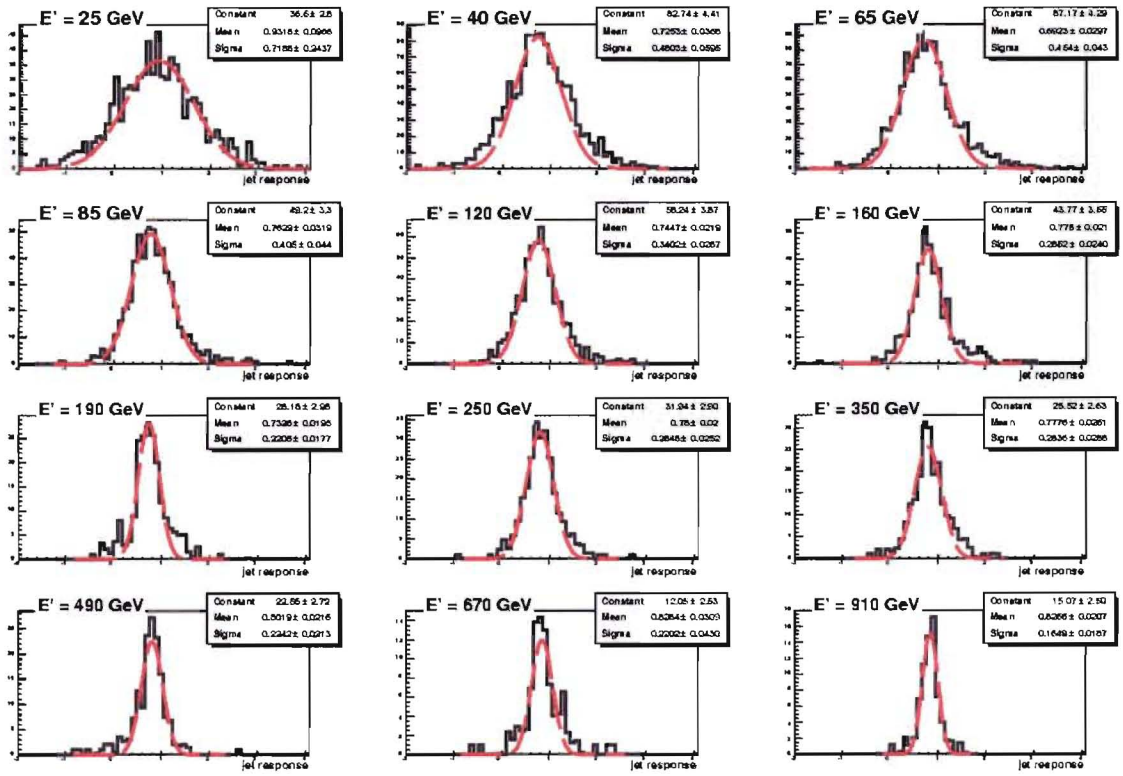

Figure D.7: Distributions of the jet response in the eleven E' bins for `ConeClusterJets` from the `Lumi05` data. The fit results are shown for each E' bin for a Gaussian fit.

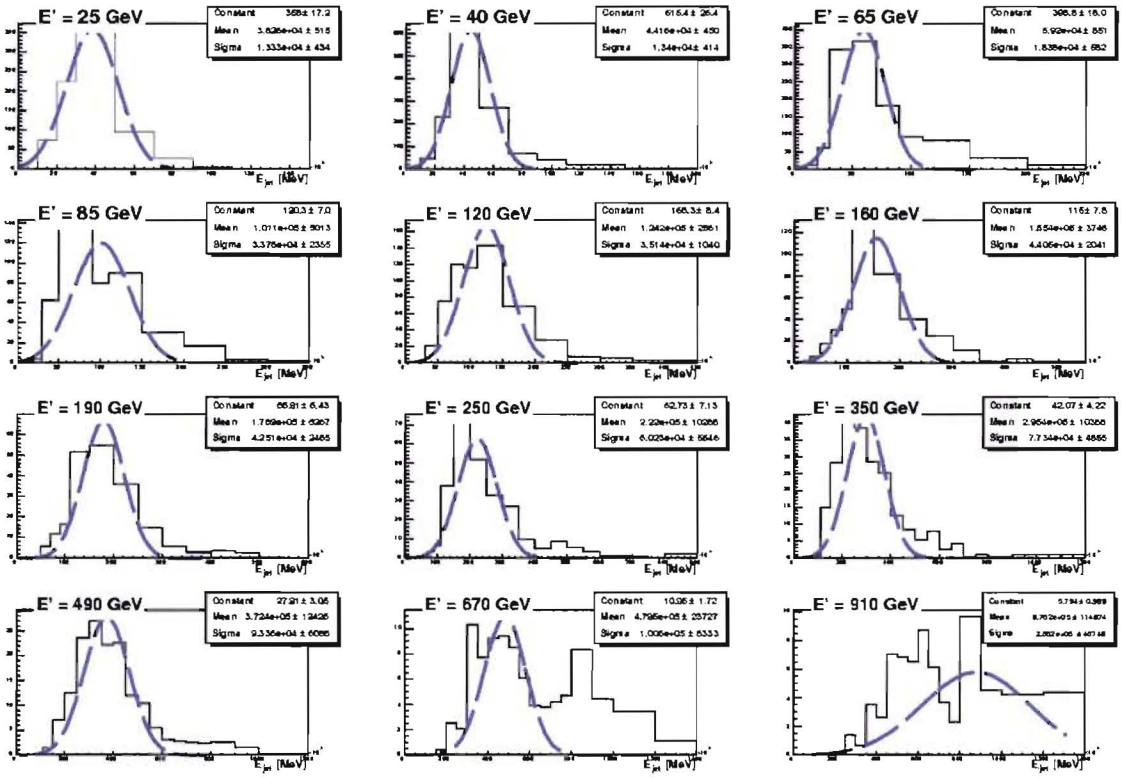

Figure D.8: Distributions of the jet energy in the eleven E' bins for `ConeClusterJets` from the `Lumi05` data. The fit results are shown for each E' bin for a Gaussian fit; however, only the mean of the distribution is used in plotting j versus $E^{meas,jet}$.

Bibliography

[1] ATLAS Detector and Physics Performance Technical Design Report Volume I & II, 1999. http://atlasinfo.cern.ch/Atlas/GROUPS/PHYSICS/TDR/access.html.

[2] ATLAS Technical Proposal for a General-Purpose pp Experiment at the Large Hadron Collider at CERN Volumes I & II, 1994. http://doc.cern.ch/archive/electronic/other/preprints//CM-P/cm-p00043027.pdf.

[3] LHC Design Report Volume I, 2006. http://ab-div.web.cern.ch/ab-div/Publications/LHC-DesignReport.html.

[4] LHC Images, 2006. http://lhc-machine-outreach.web.cern.ch/lhc-machine-outreach.

[5] Dugan Oneil. *Performance of the ATLAS Hadronic Endcap Calorimeter and The Physics of Electroweak Top Quark Production at ATLAS.* PhD thesis, ©University of Victoria, 1999.

[6] Richard Wigmans. *Calorimetery: Energy Measurement in Particle Physics.* New York: Oxford University Press, 2000.

[7] Richard Fernow. *Introduction to Experimental Particle Physics.* New York: Cambridge University Press, 1986.

[8] H. Gimm J. Hubbell and I. Overbo. *J. Phys. Chem. Ref. Data*, 9:1023, 1980.

[9] Richard Wigmans. On the energy resolution of uranium and other hadron calorimeters. *Nuclear Instruments and Methods*, A259:389–489, 1987.

[10] Dag Gillberg. A Study of Jet Response in the DØ Calorimeters. Master's thesis, ©Simon Fraser University, 2005.

[11] T.A. Gabriel, D.E. Groom, P.K. Job, N.V. Mokhov, and G.R. Stevenson. *Nuclear Instruments and Methods*, A338:336–347, 1994.

[12] Mike Vetterli. Private communications.

[13] ATLAS Liquid Argon Calorimeter Technical Design Report, 1996. http://atlasinfo.cern.ch/Atlas/GROUPS/LIQARGEXT/TDR/ps.html.

[14] ATLAS Tile Calorimeter Technical Design Report, 1996. http://atlasinfo.cern.ch/Atlas/SUB_DETECTORS/TILE/TDR/TDR.html.

[15] Chris Oram. Private communications.

[16] ATLAS Computing Technical Design Report, 2006. http://atlas-proj-computing-tdr.web.cern.ch/atlas-proj-computing-tdr/PDF/Computing-TDR-final-July04.pdf.

[17] Gerald Blazey, Jay Dittman, Stephen Ellis, et al. *Run II Jet Physics: Proceedings of the Run II QCD and Weak Boson Physics Workshop*, 2000.

[18] B. Abbott, E. Barberis, and M. Bhattacharjee *et al.* Jet energy scale at DØ. *DØ Internal Note*, 3287, 1997.

[19] Rolf Seuster. Hadronic Calibration in ATLAS. Talk presented at CALOR 2006 Conference.

[20] C. Roda and I. Vivarelli. Cell Based Jet Calibration with DC1. *Unpublished ATLAS Internal Note.*

[21] H. Wellisch, J. Kubenka, H. Oberlack, and P. Schacht. Hadronic calibration of the H1 LAr calorimeter using software weighting techniques. *H1 Notes*, 02/94-346, 1994.

[22] R. Kehoe, H. Ma, and Azzedine Kasmi. Jet response via E_T^{miss} projection. *Unpublished ATLAS Internal Note.*

[23] D.V. Bandurin and N.B. Skachkov. γ + Jet process application for setting the absolute scale of jet energy and determining gluon distribution at the Tevatron Run II. *DØ Internal Note*, 3948, hep/ex-0203003, 2002.

[24] V. Barger, T. Han, J. Ohnemus, and D. Zeppenfeld. QCD predictions for the jet activity in direct photon events at the Tevatron. *Phys. Lett.*, B232:371–376, 1989.

[25] Donatella Cavelli. Missing E_T in ATLAS. Talk presented at ATLAS Calorimeter Calibration Workshop 2006.

[26] R. A. Davis and P. Savard. Study of pileup noise in the barrel and endcap calorimetry. *Atlas Internal Notes*, CAL-NO-84, 1996.

[27] J. C. Chollet. Elementary pileup. *Atlas Internal Notes*, CAL-NO-75, 1995.

[28] L. Serin and V. Tisserand. Study of pileup in the electromagnetic calorimeter. *Atlas Internal Notes*, CAL-NO-73, 1995.

[29] W. E. Cleland and E.G. Stern. Signal processing considerations for liquid ionization calorimeters in a high rate environment. *Nuclear Instruments & Methods*, A338:467–497, 1994.